Dissertation

submitted to the

Combined Faculties of the Natural Sciences and Mathematics

of the Ruperto-Carola University of Heidelberg, Germany

for the degree of

Doctor of Natural Sciences

Put forward by

Salomé Mielke

Born in Châtel-Saint-Denis, Switzerland

Oral examination: 25.06.2019

Interfacial Viscoelasticity and Structure of Self-Assembled Semifluorinated Alkanes on Water

Referees: Prof. Dr. Motomu Tanaka
Prof. Dr. Heinz Horner

Zusammenfassung

Halbfluorinierte Alkane organisieren sich auf Wasser spontan in gleichförmige, nanometer große Domänen. Die Anordnung und Größe solcher „Oberflächenmizellen" an der Luft/Wasser Grenzschicht wird durch anziehende und abstoßende Wechselwirkungen bestimmt. In dieser Arbeit werden die viskoelastischen Eigenschaften von monomolekularen Schichten halbfluorinierter Alkane durch Grenzflächenrheologie mit oszillierendem Scheer oder Dehnung bestimmt. Die Ergebnisse zeigen, dass sich die monomolekularen Schichten vorwiegend elastisch verhalten, was durch abstoßende Kräfte zwischen den Oberflächenmizellen erklärt werden kann. Durch quantitative Röntgenkleinwinkelstreuung unter streifendem Einfall (GISAXS) konnte der Strukturfaktor und Formfaktor der Oberflächenmizellen bestimmt werden. Die systematische Veränderung der Länge und der Anzahl der Fluorkohlenstoff- und Kohlenwasserstoffketten zeigt wie eine subtile Veränderung der Molekülstruktur die Größe, Form und Korrelation der Oberflächenmizellen verändert. Eine vielversprechende Anwendung von halbfluorinierten Alkanen sind Kontrastmittel für die Ultraschalldiagnostik, die auf Mikrobläschen basieren. Diese Arbeit demonstriert, dass Perfluorhexan-Dampf, der häufig bei Mikrobläschen eingesetzt wird, um ihre Stabilität zu erhöhen, die Elastizität der monomolekularen Schichten aus halbfluorinierten Alkanen verringert, ihre Struktur aber nicht beeinflusst. Die Ergebnisse dieser Arbeit tragen zu dem fundamentalen Verständnis über die Bildung und die mechanischen Eigenschaften mesoskopischer molekularer Selbst-Organisation an Grenzflächen bei.

Abstract

Semifluorinated alkanes self-assemble spontaneously into uniform nanometer-sized domains on water. The order of such "surface micelles" at the air/water interface is achieved by the counter balance of attractive and repulsive interactions. In this thesis, the viscoelastic properties of semifluorinated alkane monolayers are investigated by using interfacial shear and dilational rheology under oscillatory strain. The obtained response function implies a predominantly elastic character of the monolayers, suggesting repulsive interactions between the surface micelles. Both the structure and the form factor of the surface micelles are determined by the quantitative analysis of grazing-incidence small-angle X-ray scattering data. A systematic variation of the length and of the number of fluorocarbon and hydrocarbon chains unravel how a subtle change in the molecular structure modulates the size, shape and correlation of the surface micelles. A promising application of semifluorinated alkanes are contrast agent microbubbles for sonographic imaging. This thesis further shows that perfluorohexane vapor - commonly used to increase the lifetime of microbubbles - reduces the elasticity of the monolayers from semifluorinated alkanes whereas their structure is not influenced. The obtained results contribute to the fundamental understanding of the formation and mechanics of mesoscopic molecular assembly at the interface.

Acknowledgments

I would like to thank everyone who helped and supported me during my doctoral studies and without whom this thesis would not exist. Special thanks go to

- Prof. Dr. Motomu Tanaka for giving me the opportunity to work in his group, his helpful ideas and his guidance,
- Prof. Dr. Heinz Horner for kindly agreeing to be my referee,
- Prof. Dr. Marie Pierre Krafft and Dr. Xianhe Liu for the great collaboration and for providing the semifluorinated alkanes,
- Prof. Dr. Kenichi Yoshikawa for the helpful discussions,
- Dr. Mariam Veschgini for guiding me through the first steps of the experiments,
- Dr. Wasim Abuillan and Dr. Aki Yamamoto for useful suggestions for the analysis,
- Dr. Oleg Konovalov for the help during the beam time at ID10 in Grenoble,
- the Landesgraduiertenförderung for financial support and the Konrad-Adenauer-Stiftung for both financial support and further education and guidance,
- my Forschi students Laura Grimm, Marisa God, Eliud Badillo, Ronja Rappolt and Martin Reinschmidt for the excellent work in the lab and useful contributions to my experiments,
- Dr. Stefan Kaufmann, Judith Thoma, Federico Amadei, Dr. Maryam Eshrati, Benjamin Fröhlich, Sven Mehlhose, Philipp Linke, Ryo Suzuki, Julian Czajor and Esther Kimmle for the help in the lab, especially during my pregnancy, the great coffee and chocolate breaks or the fun time at the beamtimes in Grenoble,
- all other colleagues of the Tanaka group for the great time in the past years.

Finally I am grateful to my parents Ulrike and Andreas for their constant interest in my work, the unwavering support and especially for looking after Johannes and thus enabling me to work in the last months of my PhD studies. Additionally, I am extremely grateful to Daniel for his great support, his kindness, his ideas and his patience. And a big thank you goes to Johannes for giving me the best distraction from work and finding always a way to make me smile.

Contents

List of Figures

List of Tables

1. Introduction

Due to their exceptional properties, perfluorocarbon materials have become indispensable in modern life. One of the most prominent examples is Teflon (polytetrafluoroethylene, PTFE) which is used among others in cookware, as lubricant and as coating and grafting material in medical applications.[56] But also simpler perfluorocarbons such as perfluorohexane (C_6F_{14}, PFH) have found applications, e.g. in medicine as breathing liquid for damaged lungs.[8,51]

In the 1980s, researchers at IBM (San José, CA) and at the Institut Charles Sadron (Strasbourg, France) designed novel hydrocarbon/fluorocarbon molecules (semifluorinated alkanes) which soon came into the focus of research in physical chemistry due to their exceptional properties. These are, among others, the strong dipole moment at the junction between the fluorocarbon segment and the hydrocarbon segment and a distinct difference in the cross-sectional areas of these chains.[1] Interestingly, long semifluorinated alkanes (> 22 carbon atoms) self-assemble spontaneously at the air/water interface into monolayers composed of highly uniform, nanometer-sized circular domains, so-called surface micelles.[2] [48] These surface micelles are very stable against coalescence and their size can be regulated by the balance between fluoro- and hydrocarbon segment lengths.[48]

Self-assembly of small molecules into regular, periodic patterns in two-dimensional (2D) films is a phenomenon found for various different systems such as ferrofluids[14], block copolymers[69,109] and fluorinated lipids.[84,96] They are also often found in lipids that show coexistence of a liquid expanded phase and a liquid condensed phase.[72] Such patterns, e.g. stripes or domains, result mostly from the interplay of attractive and repulsive intermolecular interactions.[3] In addition to the line tension minimizing the length of the border between self-assembled structures and the surrounding matrix, the repulsive interactions such like dipole repulsions cause the emergence of non-conventional patterns.[3] The ordering of molecules into domains

[1] A more detailed description about the physical and chemical properties of semifluorinated alkanes is given in Section 2.2

[2] In the following, these surface micelles are also denoted as (nano)domains. In the literature, they are also often called "hemimicelles"

is expected to strongly influence the mechanics of the film at the interface, in particular the viscous and elastic properties.[20,61] For example Li Destri et al. studied the viscoelastic properties of monolayers made of different copolymer molecules and found that the monolayers of circular micelles respond to the external strain in a predominantly elastic way whereas an entanglement into wormlike micelles exhibited a more fluid and thus viscous response of the film.[20] From a physical point of view, studying the viscoelasticity of monolayers composed of organized domains is elucidating as the viscoelastic properties result not only from intermolecular interactions between single molecules but also from macroscopic interactions between the individual domains.

In addition to the fascinating self-assembling characteristics of semifluorinated alkanes, they have other unique properties such as their biological and chemical inertness and their ability to reduce the surface tension of water. This makes them interesting for biomedical applications. For example, Perfluorohexyloctane ($C_6F_{13}C_8H_{17}$) is successfully used as a treatment of dry eyes.[102] Because of the hydrophobicity and lipophobicity of the fluorocarbon segments, these molecules are not internalized into cell membranes and thus possess no cell toxicity. Among the very promising future applications is their use as contrast agents in ultrasound diagnostics of blood vessels. This can be achieved by fabricating microbubbles coated with semifluorinated alkanes.

Due to their size ($1 - 8\,\mu m$), gas-filled microbubbles have a resonant frequency which lies in the ultrasound region ($2 - 15\,MHz$).[55,98] They act as echo-enhancers by back-scattering the ultrasound waves which allows an exact visualization of their position.[98] It was shown that their ability to scatter ultrasound is ten times higher than that of red blood cells which have a similar size.[85,98] Therefore, the injection of the bubbles into the blood makes it possible to image vessels or the blood flow within an organ.[55,98] For example this can help to distinguish tumors from healthy tissue which often differ in their blood circulation.[98] Another promising approach is the therapeutic use of microbubbles by loading them with drugs.[55,98]

Compared to other diagnostic methods like MRI, sonography is a widely available, cheap and quick technique. However, there are several obstacles that impede the fabrication of suitable microbubble contrast agents. First of all, the bubbles need to be non-cytotoxic and must be easily discarded from the human body after the imaging. Additionally, they should have a uniform size distribution and need to be small enough to pass through thin capillaries such as the lung capillaries which have a diameter of $5 - 10\,\mu m$.[98] The most crucial limitation is the stability of the

bubbles. Microbubble contrast agents based on lipid or albumin shells are already commercially available[3] but they have the major disadvantage that they are only stable in the blood for a short time and burst quickly under ultrasonic stress.[55,98] The lifetime of microbubbles needs to be long enough to allow a thorough diagnosis and additionally the microbubbles need to be able to withstand the constant deformation by ultrasonic stress and by passing through thin capillaries.[55] Since the lifetime of microbubbles is mainly limited by the fast diffusion of the core gas into the surrounding medium (blood), it can be increased in a two step procedure:[98] First, the bubbles can be stabilized by an appropriate shell. Among the material used so far are lipids, proteins and polymers.[55] A second promising step is the osmotic stabilization by filling the bubbles with a fluorocarbon gas which has an extremely low water solubility.[51,98,104] It was shown that microbubbles with a lipid shell and a core filled with perfluorohexane enriched nitrogen were stable over $\sim 90\,\mathrm{min}$ which is $4-5$ times longer than bubbles filled with air.[4][104] However the lifetime is reduced when the microbubbles are subjected to ultrasonic stress and undergo a continuous oscillation. Therefore, they need to be stabilized by providing them with an elastic shell which can withstand large deformations.

Semifluorinated alkanes were already shown to increase the stability of lipid vesicles and water-in-oil emulsions.[7,22,95] Therefore, micrometer-sized bubbles covered by semifluorinated alkanes are expected to exhibit outstanding mechanical stability. Furthermore, the self-assembly of semifluorinated alkanes into nanometer-sized surface micelles suggests a predominantly elastic behavior which is favorable for the application as microbubble contrast agents. As a straightforward approach to verify this one can study the dynamics of 2D monolayers composed of semifluorinated alkanes at the gas/water interface under constant compression and expansion. Such a flat 2D system can be understood as a very simple model system to the three-dimensional microbubbles.

This dissertation aims to shed light on the structural and viscoelastic properties of monolayers composed of two different types of semifluorinated alkanes with various lengths at the air/water interface. To this end, two methods of interfacial rheology, interfacial shear and dilational rheology[5] were used to quantify the viscoelastic properties of the semifluorinated alkane monolayers under oscillatory strains. The elastic and viscous moduli were measured with respect to strain frequency, amplitude and surface pressure. To gain further insight into the size, shape and correlation of semi-

[3] For example SonoVue®, Definity® or Sonazoid®
[4] i.e. loss of the total bubble volume $< 70\,\%$
[5] Rheology and interfacial rheology in particular are introduced in Section 2.3

fluorinated alkane surface micelles moduliating the viscoelastic properties, grazing-incidence small-angle X-ray scattering (GISAXS)[6] was employed. The quantitative GISAXS analysis enables the precise determination of both form factor and structure factor of surface micelles. The systematic change in the length and number of semifluorinated alkyl chains unraveled how a subtle change in molecular structures modulates the order and viscoelasticity of surface micelles. The interfacial shear rheology experiments on semifluorinated alkane monolayers at the air/water interface are presented in Chapter 4, Chapter 5 contains the description and analysis of the interfacial dilational rheology experiments. In Chapter 6 the size, shape and correlation of the semifluorinated surface micelles calculated from GISAXS data are presented and discussed.

Towards biomedical applications of microbubbles coated with the surface micelles of semifluorinated alkanes, the influence of perfluorocarbon vapor on the mechanics and structuring of the interfacial film composed of semifluorinated alkanes was investigated. This is in detail presented in Chapter 7. In fact, perfluorocarbons such as perfluorohexane have been found to adsorb at the air/water interface and are hence expected to alter the ordering of the surfactant molecules on the water which could have an effect on the mechanical properties of the monolayers.[15] In addition to the rheological methods which provide information about the viscoelastic properties, GISAXS was also applied to study the influence of perfluorocarbon vapor on the size, shape and correlation of surface micelles.

In a further step, mixed monolayers of semifluorinated alkanes and lipids at the air/water interface were studied (Chapter 8). In contrast to semifluorinated alkanes, lipids self-assemble into smooth monolayers at the air/water interface that sometimes show patterns when domains of lipids in the liquid expanded phase and the liquid condensed phase coexists. To elucidate the properties of the mixed monolayers compared to the pure components, two different approaches were used. First, the monolayers were investigated by fluorescence microscopy. In particular the influence of the semifluorinated alkanes on the phase transition behavior of the lipids under compression was studied. In a second approach, the viscoelastic properties of the mixed monolayers and the monolayers of the pure components were measured using interfacial dilational rheology. This allows us to get a further understanding of how the ordering of molecules into surface micelles at the interface regulates the mechanics of the monolayers. This procedure also helps to identify how the semifluorinated alkanes within the lipid monolayer are ordered.

[6] The method GISAXS is explained in detail in Section 2.4

2. Theoretical and Experimental Background

This chapter provides background information that is necessary for the different aspects of this thesis and is divided into four sections. It contains first a short introduction about the physics of interfaces and surfactants and presents the core instrument used in this thesis, the Langmuir film balance (Section 2.1). Afterwards the physical and chemical properties of the fluorocarbon/hydrocarbon materials studied are described (Section 2.2). Section 2.3 provides an introduction into the physics of viscoelasticity and the interfacial rheological methods used in this thesis (Section 2.3). The last section gives a brief description of GISAXS (Section 2.4).

2.1. Interfaces and Surfactants

Interfaces are boundaries between two immiscible phases. In nature, we are often confronted with the air/water interface. An important measure concerning interfaces is the interfacial tension γ. It corresponds to an interfacial free energy and describes the tendency of the liquid to acquire the least possible interfacial area.[91] Compared to molecules in bulk, molecules at the air/liquid interface have less neighboring molecules leading to a higher energy state. To minimize this energy, the liquid needs to minimize the number of molecules at the surface leading to a decreased surface area. The interfacial tension γ is hence given in energy per unit area, $[\gamma] = 1\,\mathrm{J\,m^{-2}} = 1\,\mathrm{N\,m^{-1}}$.[43,91] Due to the high cohesive forces of the water molecules, water exhibits a strong surface tension of $\gamma_{\mathrm{water}} \approx 73\,\mathrm{mN\,m^{-1}}$.[91]

The interfacial tension can be reduced by surface active materials (surfactants). Surfactants are amphiphilic molecules that normally compromise a polar, hydrophilic part and a hydrophobic part. A common example for surfactants in nature are lipids as they have a polar headgroup that is attached to the hydrocarbon chain(s), the hydrophobic tail.[42,91]

In water, surfactants aggregate in various shapes, e.g. micelles, depending on their molecular conformation. They also adsorb to the air/water interface where

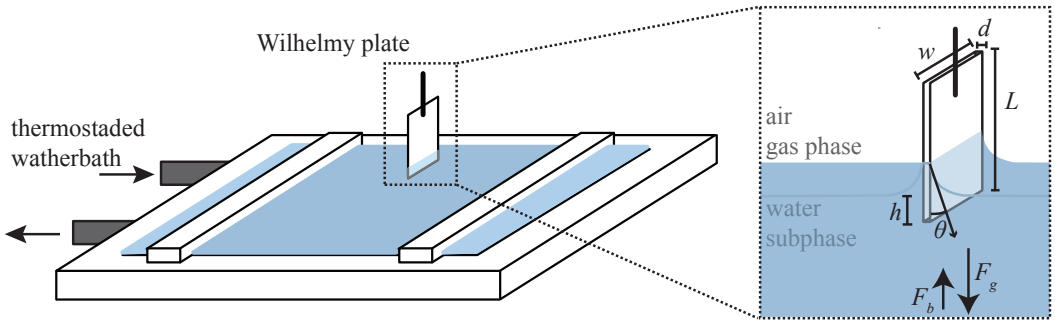

Figure 2.1.: **Schematic illustration of a Langmuir film balance.** It consists of a hydrophobic trough filled with the subphase (water). The surface area is controlled by two motor-driven, movable barriers. The temperature is controlled by a thermostated water bath which circulates through the trough. The surface pressure is controlled by a Wilhelmy plate attached to a force sensor. On the right, the Wilhelmy plate is illustrated in a larger scale indicating the dimensions of the plate and the forces acting on the plate. (inspired by [53])

the hydrophilic part is immersed into the water phase and the hydrophobic part points towards the air. At the air/water interface, surfactants hence form monolayers.[91] One distinguishes between Gibbs monolayers and Langmuir monolayers. Gibbs monolayers develop from surfactants that are in the bulk of the subphase and adsorb to the air/water interface once a critical micelle concentration is reached. Langmuir monolayers are directly spread on the air/water interface, therefore there are no surfactant molecules in the subphase. Typically, the surfactants are dissolved in an organic solvent which after spreading on the water will evaporate and leave behind the surfactant Langmuir monolayer. The decrease of the surface tension depends on the intermolecular distance, i.e. the surface density of the surfactant molecules.[42]

The most common used technique to study the behavior of surfactant monolayers is the Langmuir film balance.[42] Figure 2.1 shows the setup schematically. The film balance consists of a Langmuir trough which is usually made out of Teflon or another hydrophobic material and is filled with a subphase, typically water. It is equipped with one or two motor-driven, movable barriers that allow to vary the surface area without changing the bulk volume. A specific amount of the surfactant solved at a specific concentration in an organic solvent is spread on the water surface between the two barriers where the surfactant molecules form a Langmuir monolayer so that the number of surfactant molecules is known. The surface density and hence the

interfacial tension can be changed by compressing the film with the barriers. We can describe the surface density by the molecular area, typically given in Å^2. The reduction of the surface tension of pure water γ_0 compared to the surface tension with the surfactants present γ is given as a surface pressure[42] π,

$$\pi = \gamma - \gamma_0. \tag{2.1}$$

The surface pressure can be measured by the Wilhelmy plate method.[53] A Wilhelmy plate is a thin platinum plate or a filter paper of width w, length L and thickness d, which is attached to a force sensor (Figure 2.1). When the plate is partially immersed into a liquid with density ρ_{subphase} by the depth h, a force F is acting on the plate given by[53]

$$F = F_g + F_\gamma + F_b \tag{2.2}$$

$$= \rho_{\text{plate}} dwLg + 2(w+d)\gamma\cos\theta - \rho_{\text{subphase}} dwhg \tag{2.3}$$

where F_g is the gravitational force with the gravitational constant g and the density of the plate ρ_{plate}, F_γ is the force due to the interfacial tension with the contact angle θ between the liquid subphase and the Wilhelmy plate, and F_b is the buoyancy (see Figure 2.1). In the case of platinum or paper, one can assume a complete wetting of the plate surface which results in $\cos(\theta = 0) = 1$.[42,53]

If we assume $w \gg d$, we can measure the surface pressure of the monolayer film by the force difference $\Delta F = F_s - F_w$, where F_s is the force acting on the Wilhelmy plate which is immersed into water with surfactant molecules, and F_w is the force acting on the plate in the case of only water without surfactant molecules:[53]

$$\pi = \gamma - \gamma_0 \approx \frac{\Delta F}{2w}. \tag{2.4}$$

In order to keep the temperature constant, film balances are often equipped with a thermostaded water bath. Measuring the surface pressure π with respect to the molecular area A at a constant temperature results in so-called pressure/area (π/A-) isotherms.

The shape of the π/A-isotherms can provide information about the ordering of the surfactant molecules depending on the available area. More exactly, we can learn about the phase behavior of the surfactant molecules.[42] The amount is chosen such that the surface pressure is still $0\,\text{mN}\,\text{m}^{-1}$ when the barriers are fully open. In that case the surfactants are mostly homogeneously distributed over the available surface

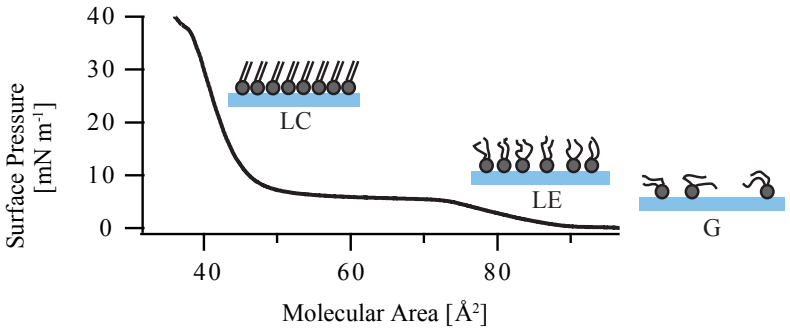

Figure 2.2.: **Isotherm of a DPPC monolayer showing schematically the different phases of the lipids upon compression.** At large molecular areas ($> 90\,\text{Å}^2$), the lipids are in the gas phase (G). The increase in surface pressure upon compression demonstrates the phase transition to the liquid expanded (LE) phase. The plateau-region indicates the begin of the transition to the liquid condensed (LC) phase where LE and LC phase coexists until a steep increase in the surface pressure marks the begin of the pure LC phase. (Inspired by[77] p.112)

which corresponds to the gas (G) phase of the film. When compressing the film, we can observe an increase of the surface pressure at a characteristic molecular area which marks the transition to the liquid expanded (LE) phase. Further compression often results into a liquid condensed (LC) or solid (S) phase, depending on the type of surfactant. Typically the transitions from an expanded to a condensed phase correspond to a loss of freedom of the surfactant molecules, a lower separation of the polar headgroups and an increased order of the hydrophobic chains.[42,77]

The π/A-isotherms allow the calculation of the isothermal compressibility[77]

$$\kappa^{-1} = -\frac{1}{A}\left(\frac{\partial A}{\partial \pi}\right)_T \tag{2.5}$$

which describes the slope of the π/A-isotherm depending on the molecular area. Being a derivative of the free energy, the compressibility contains information about phase transitions. A first order phase transition is given when $\kappa^{-1} \to \infty$ which can be detected by a horizontal slope in the π/A-isotherm. This behavior is often observed for isotherms of phospholipids at the LE/LC transition where we observe a plateau characterizing a coexistence of LE and LC phase.[42] Figure 2.2 displays a typical π/A-isotherm including the schematic illustration of the lipid phases recorded for DPPC, a phospholipid exhibiting a headgroup and two saturated hydrocarbon chains with 16 carbons (see chemical structure in Figure 3.1, Section 3.1.2, the experimental procedure is described in Section 3.2.1). At 20°C, we observe a plateau

region indicating the LE/LC phase transition where both phases coexist. In the LC phase, the hydrocarbon chains are in an all-trans conformation whereas in the LE phase, the hydrocarbon chains are disordered.[42,77] The region of coexistence of LE and LC phase depends on the temperature. With increasing temperature, the plateau region decreases until at a critical temperature T_c the monolayer does no longer undergo a phase transition.[77] Neutron scattering techniques revealed a decrease of the thickness of the monolayer during the compression which can be attributed to the phase transition.[42]

Being a first order phase transition, the change in the Gibbs free energy $\Delta G = \Delta H - T\Delta S$ should be 0, so that the change in the entropy ΔS can be described by

$$\Delta S = \frac{\Delta H}{T_m}, \tag{2.6}$$

where ΔH is the change of the enthalpy and T_m the transition temperature. In case of lipids such as DPPC, this entropy is in the order of $\sim 15 k_B$ per molecule where k_B is the Boltzmann constant.[77] Using

$$\Delta S = k_B \ln \Omega \tag{2.7}$$

we can assume that roughly $\Omega = 10^5 - 10^6$ microstates are involved in this phase transition, which can be attributed to the configurations of the hydrocarbon chains which go from an disordered state to a all-trans configuration during the LE/LC phase transition.[77]

2.2. Perfluorocarbon Materials

In the following Section, the physical and chemical properties of fluorocarbon materials will be elaborated. In Section 2.2.2, semifluorinated alkanes are introduced, which were intensively studied for this thesis.

2.2.1. Fluorine and Fluorocarbon Materials

Fluorine is the element with the highest electronegativity (4.0) which hence results in a low polarizability. Compared to hydrocarbon, fluorocarbons are very stable. Carbon has a much lower electronegativity than fluorine (2.5), therefore the C-F bond is highly polar and very strong, it is even the strongest bond found in organic chemistry.[52] Additionally, due to the electron withdrawal by the fluorine atoms, the C-C bond in fluorocarbons is strengthened.[56] These main physical properties

of fluorine itself and the C-F bond result in a broad variety of physical and chemical properties of fluorocarbon materials which make them so exceptional.

For example, the low polarizability is the reason for very low cohesive forces between fluorocarbon molecules.[56] This means that the surface energy of fluorocarbons is very low. This is the explanation for fluorocarbon being highly volatile. Besides, it is also the reason for the extremely low solubility of fluorocarbons in water.[56] Perfluorohexane (PFH) for example has a water solubility of $2.7 \times 10^{-4}\,\mathrm{mol\,m^{-3}}$ which is three orders of magnitude smaller than that of oxygen ($0.48\,\mathrm{mol\,m^{-3}}$).[35,44] This feature makes air saturated with PFH interesting for the application as microbubbles used for sonication imaging. It was shown that it increases the lifetime of lipid DMPC (1,2-dimyristoyl-sn-glycero-3-phosphocholine) microbubbles by a factor of 4-5 compared to air without PFH.[104] Furthermore, due to the weak intermolecular forces of perfluorohexane, gases such as oxygen can enter easily into the liquid which explains why perfluorohexane is used as breathing liquid for damaged lungs.[49,86,90]

Fluorocarbon chains differ strongly from hydrocarbon chains. First of all, fluorocarbon chains are bulkier. This has two reasons: first, fluorine has a higher van der Waals radius ($r_\mathrm{F} = 1.47\,\text{Å}$ compared to $r_\mathrm{H} = 1.2\,\text{Å}$ for hydrogen).[9] Second, the C-F bond length is $\sim 20\,\%$ longer than the C-H bond.[56] The mean volume of a CF_3 group was estimated to be $92\,\text{Å}^3$, which is $\sim 60\,\%$ bigger than the volume of the respective CH_3 group, $54\,\text{Å}^3$.[52] This results in a cross section area of the fluorocarbon chains of $\sim 27-30\,\text{Å}^2$, compared to $\sim 18-21\,\text{Å}^2$ for hydrocarbon chains.[52] Various studies claim that the larger surface area of fluorocarbon chains explain the extreme hydrophobicity of fluorocarbons compared to hydrocarbons.[52] The different steric requirements of the CF-groups compared to the CH-groups also lead to a helical conformation of longer fluorocarbon chains whereas hydrocarbon chains arrange in a planar conformation. Additionally, fluorocarbons display decreased cohesive forces compared to their hydrocarbon counterparts. Therefore fluorocarbon and hydrocarbon moieties will not mix, making fluorocarbons lipophobic in addition to their strong hydrophobicity.[52]

2.2.2. Semifluorinated Alkanes

In the previous paragraph, the differences between hydrocarbon and fluorocarbon chains were elaborated. Yoking hydrocarbon and fluorocarbon chains together as semifluorinated alkanes results in molecules with interesting properties on the molecular, microscopic and mesoscopic scale. First studies of the structure and properties of semifluorinated alkanes were published in the 1980s.[67,88] Since then, various types

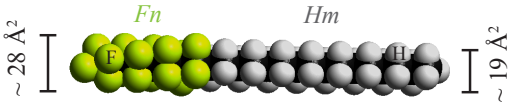

Figure 2.3.: **Chemical structure of a *F8H16* diblock molecule.** The fluorine atoms are marked in green, the hydrogen atoms in gray and the carbon atoms in black. The crosss-Sectional areas of hydrcarbon and fluorocarbon chains are given in the scheme.

of semifluorinated alkanes were synthesized.

The simplest semifluorinated alkane molecule is built of a linear combination of a fluorocarbon and a hydrocarbon chain and has hence the chemical structure $C_nF_{2n+1}C_mH_{2m+1}$ were n corresponds the number of carbons in the fluorocarbon segment and m to the number of carbons in the hydrocarbon segment. In the literature, these molecules are called $FnHm$ diblocks. The chemical structure of $FnHm$ diblocks is exemplarily shown in Figure 2.3 for $F8H16$. These diblock molecules have three interesting properties. They are:[52]

1. Amphisteric: The fluorocarbon segments are bulky and rigid whereas the hydrocarbon segments have a smaller cross section and are flexible. The cross section area of the hydrocarbon chains is $\sim 30\,\%$ smaller than that of the fluorocarbon segment.

2. Amphiphilic: The fluorocarbon segments are hydrophobic and lipophobic, the hydrocarbon segments on the other hand are hydrophobic and lipophilic.

3. Amphidynamic: The fluorocarbon segments take up a helical conformation whereas the hydrocarbon segments arrange in a planar conformation.

There are many more specific properties of the $FnHm$ diblocks which are based on these three characteristics.

Due to the different electronegativity of fluorine and hydrogen, the $FnHm$ diblock molecules exhibit a strong dipole at the junction between fluorocarbon and hydrocarbon segments. The dipoles of the CF bonds are stronger and opposite directed to the CH bond dipoles, so that the fluorocarbon segment withdraws electrons from the hydrocarbon part of the molecule. Additionally, the terminal CF_3 and also the CH_3 group contribute to the overall dipole moment of the $FnHm$ molecule which is out of the plane axis of the molecule with an estimated angle of $35°$.[52] The exact dipole moment of an $FnHm$ molecule has not yet been measured but was calculated to be in the range of $(9.7 - 11.3) \times 10^{-30}\,\mathrm{Cm}$.[52]

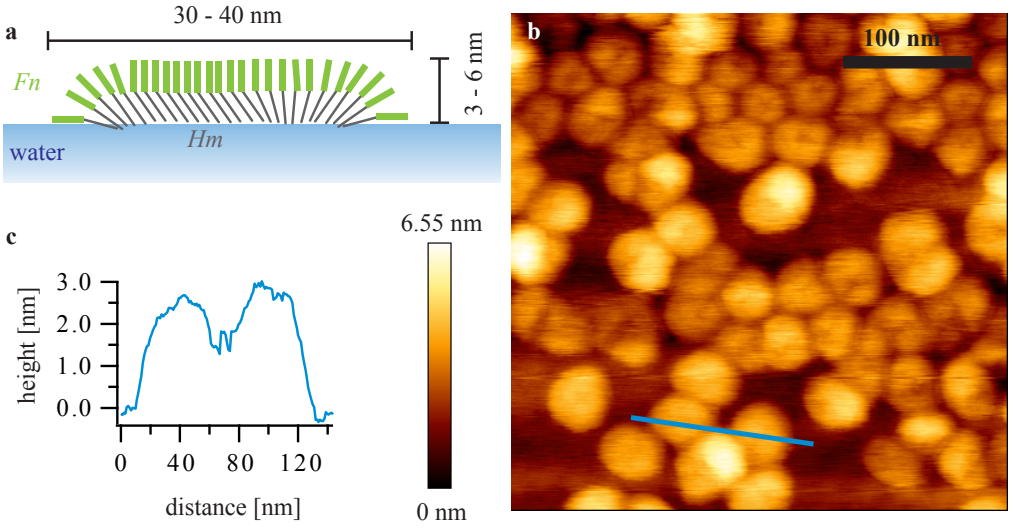

Figure 2.4.: **Formation of surface micelles by *FnHm* diblock molecules.** a) Schematic illustration of a surface micelle on water with the measured dimensions. One surface micelle contains thousands of diblock molecules, the illustration is hence not in scale. b) AFM image of a $F12H16$ monolayer transferred via Langmuir-Blodgett on a Silicon wafer at $\pi = 4\,\mathrm{mN\,m^{-1}}$ (sample preparation and imaging explained in Sections 3.2.6 and 3.2.7). c) Height profile of the blue line in the AFM image.

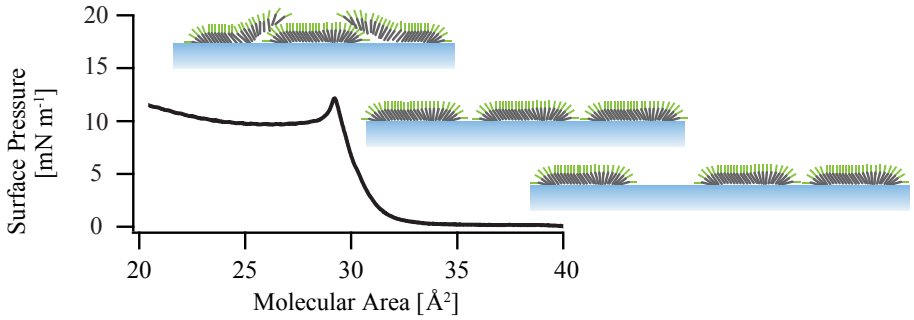

Figure 2.5.: **π/A-isotherm of a $F8H16$ monolayer at the air/water interface.** The monolayer was compressed with a speed of $3.75\,\mathrm{cm^2\,min^{-1}}$ and at 20°C. The ordering of the surface micelles on the water subphase is illustrated schematically. After the collapse of the monolayer at $\pi \approx 12\,\mathrm{mN\,m^{-1}}$, a second layer is formed above the monolayer.

The amphiphilic character of the $FnHm$ molecules makes them surface active and they form Langmuir monolayers on water.[26] One of the most interesting surfactant feature is that the longer diblocks ($n > 8$, $m > 14$) spontaneously self-assemble into nanometer-sized surface micelles at the air/water interface.[17,48,65] As schematically shown in Figure 2.4a, the diblock molecules arrange on the water surface in such a way that the hydrocarbon segments point towards the water whereas the fluorocarbon segments point in the air. Recent investigations showed that the hydrocarbon segments arrange in an all-trans conformation and are tilted by $\sim 30°$ with respect to the water surface.[99]

Figure 2.4b shows an Atomic Force Microscopy (AFM) image of a monolayer of $F12H16$ diblocks which self-assembled into circular shaped surface micelles. The monolayer was obtained by transferring it from the air/water interface to a silicon wafer by Langmuir Blodgett at a surface pressure of $\pi = 4\,\mathrm{mN\,m^{-1}}$. A detailed description of the preparation of the solid-supported monolayer is given in Section 3.2.6 and the AFM imaging is described in Section 3.2.7. Although transferring the monolayer to a solid substrate is expected to alter the arrangement of the surface micelles and their exact dimensions, AFM images prove the existence of the surface micelles visually and provide first information about their size and shape. Interestingly, the surface micelles are circular and very uniform in size. Figure 2.4c shows the height profile of the blue line in the AFM image revealing diameters of the surface micelles in the range of $\sim 40\,\mathrm{nm}$ with heights in the range of $\sim 3\,\mathrm{nm}$ which corresponds to the length of one $F12H16$ diblock molecules. Similar images were published previously.[17,48]

The surface active properties of the $FnHm$ diblocks were mostly studied by Langmuir film balances.[1] [17,26] The π/A-isotherms of $FnHm$ diblocks which are self-assembled into the surface micelles have characteristic shapes. Figure 2.5 shows an isotherm of a $F8H16$ monolayer as an example, indicating the different phases: At large surface areas, the surface pressure is $0\,\mathrm{mN\,m^{-1}}$ and the monolayer is in a gas phase as indicated by large gaps between the surface micelles. The surface pressure starts to increase at a molecular area of $\sim 30\,\mathrm{\AA}^2$ followed by a steep increase in the surface pressure which is characterized by very low compressibilities around $\kappa^{-1} = 5 - 10\,\mathrm{m\,N^{-1}}$.[17] Here, the surface domains arrange in a lattice without changing in size or coalescing.[48] At surface pressures between 10 and $18\,\mathrm{mN\,m^{-1}}$, the monolayer collapses which is demonstrated by a sudden decrease in the surface pressure which is followed by a long plateau region.[17] The collapse pressure is characteristic for each diblock molecule and increases with the length of the molecule.[48] It was shown for the $FnHm$ monolayers that this collapse is marked by a 2D/3D film transition: The lower layer of the well-ordered surface micelles stays mostly intact and a second layer above is formed in which the diblocks take a homogeneous bilayer conformation.[17,23] This was studied by AFM where on transferred, solid-supported monolayers,[17] and confirmed by GISAXS at the air/water interface.[23]

Beside the $FnHm$ diblocks, it is also possible to synthesize other forms of semifluorinated alkanes such as the so called tetrablocks di$(FnHm)$[2].[18,19] Again, n denotes the length of the fluorocarbon segment and m the length of the hydrocarbon segment. Figure 2.6 shows the chemical structure. They inherit the same basic chemical properties as the diblock molecules, e.g. they are amphisteric, amphiphilic and amphidynamic. The tetrablock molecules di$(FnHm)$ ($n = 8, 10$ and $m = 16 - 20$) were also shown to self-assemble spontaneously into well-ordered arrays of surface micelles on hydrophilic substrates with diameters of $\approx 40\,\mathrm{nm}$.[18,19] The π/A-isotherms of the di$(F10Hm)$ tetrablocks show the same characteristic shape with an onset of the increase of the surface pressure at $\sim 60\,\mathrm{\AA}^2$, a steep increase of the surface pressure with compressibilities around $\kappa^{-1} \approx 6\,\mathrm{m\,N^{-1}}$ followed by the collapse of the monolayer at $\pi_c \approx 11 - 24\,\mathrm{mN\,m^{-1}}$ where higher values correspond to higher m.[18] It was shown that the compression of the Langmuir monolayers of the di$(FnHm)$ tetrablocks beyond the collapse pressure leads to a formation of a second layer of surface micelles on top of the first layer.[19]

The interesting properties of semifluorinated alkanes open a broad field of possible

[1] So far, the self-assembly of $FnHm$ diblocks into surface micelles was reported for $F6H16$, $F8H14$, $F8H16$, $F8H18$, $F8H20$, $F10H16$, $F12H16$[48]

[2] $(\mathrm{C}_n\mathrm{F}_{2n+1}\mathrm{CH}_2)(\mathrm{C}_{m-2}\mathrm{H}_{2m-3})\mathrm{CH} - \mathrm{CH}(\mathrm{C}_n\mathrm{F}_{2n+1}\mathrm{CH}_2)(\mathrm{C}_{m-2}\mathrm{H}_{2m-3})$

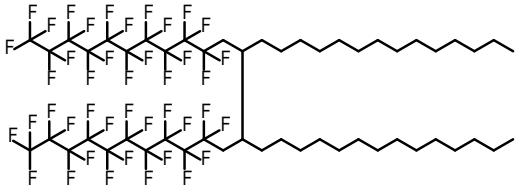

Figure 2.6.: **Chemical structure of a di($FnHm$) tetrablock molecule** for $n = 10$ and $m = 16$.

applications. $FnHm$ diblocks were found to stabilize small unilamellar vesicles made of phospholipids[22,95] and water-in-oil emulsions[7]. Therefore, it is promising to apply them as stabilizer for microbubbles used as contrast agents in sonographic imaging. The small chain diblock molecule $F6H8$ is already used in medicine as a lubricant for dry eyes.[102]

2.3. Rheology

Rheology is the science of viscoelastic materials. These are materials which have properties of both fluids and solids and hence behave both in an elastic and a viscous way.[11] In the following, the important terms of rheology will be defined and explained.

2.3.1. Viscoelastic Materials

Different viscoelastic materials show different characteristic responses to the forces acting on them. The behavior of a material is controlled by the intermolecular forces within the material. In order to physically define viscoelastic materials, we have to distinguish between stress and strain and explain what the properties of perfect elastic and perfect viscous materials are. In a next step, the time-dependent behavior of viscoelastic materials is explained including rheological models and methods to measure the rheology of 2D interfacial films are introduced.

Stress

The stress σ is given by the force F acting on the area ΔA of a deformable body, e.g.

$$\sigma = \frac{F}{\Delta A} \tag{2.8}$$

and has therefore the unit $\mathrm{N\,m^{-2}}$. It describes the internal forces in a body.

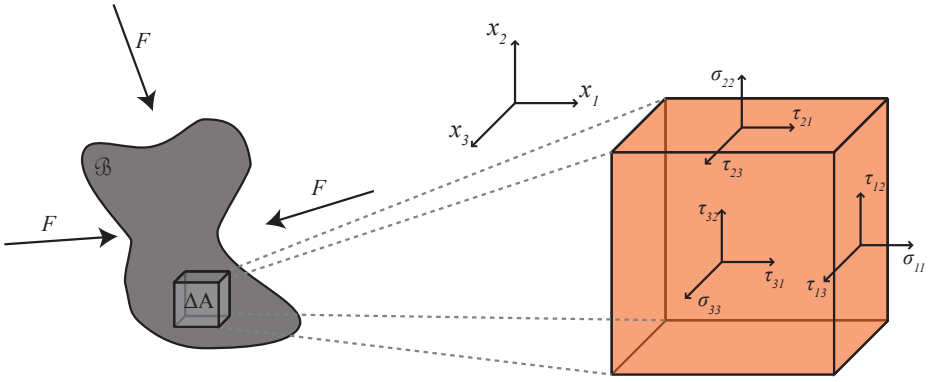

Figure 2.7.: **Schematic representation of the forces F acting on a body resulting in the demonstrated components of the stress tensor.** (Adapted from ref.[25] and[100])

In a three dimensional body $\mathcal{B}$, forces may act from different directions. When we take a closed surface ΔA inside the body $\mathcal{B}$ (see Figure 2.7), the stress describes the forces on the boundary areas. Depending on the direction of the force, we can distinguish between normal stresses σ_{ii} perpendicular to the boundary area (e.g. compression) and shear stresses $\boldsymbol{\tau} = \sigma_{ij}$, $i \neq j$ going tangential to the area. We can therefore describe the stress by the Cauchy stress tensor:

$$\boldsymbol{\sigma} = \begin{pmatrix} \sigma_{11} & \sigma_{12} & \sigma_{13} \\ \sigma_{21} & \sigma_{22} & \sigma_{23} \\ \sigma_{31} & \sigma_{32} & \sigma_{33} \end{pmatrix}. \tag{2.9}$$

The individual components of $\boldsymbol{\sigma}$ are schematically illustrated in Figure 2.7.[25,87]

Strain

When a stress $\boldsymbol{\sigma}$ is applied to a viscoelastic body, we will observe a deformation that can be described by strain $\boldsymbol{\epsilon}$. The strain gives the relative displacement of a point in body $\mathcal{B}$ with respect to its former position and is given by[87,100]

$$\boldsymbol{\epsilon} = \begin{pmatrix} \epsilon_{11} & \epsilon_{12} & \epsilon_{13} \\ \epsilon_{21} & \epsilon_{22} & \epsilon_{23} \\ \epsilon_{31} & \epsilon_{32} & \epsilon_{33} \end{pmatrix}. \tag{2.10}$$

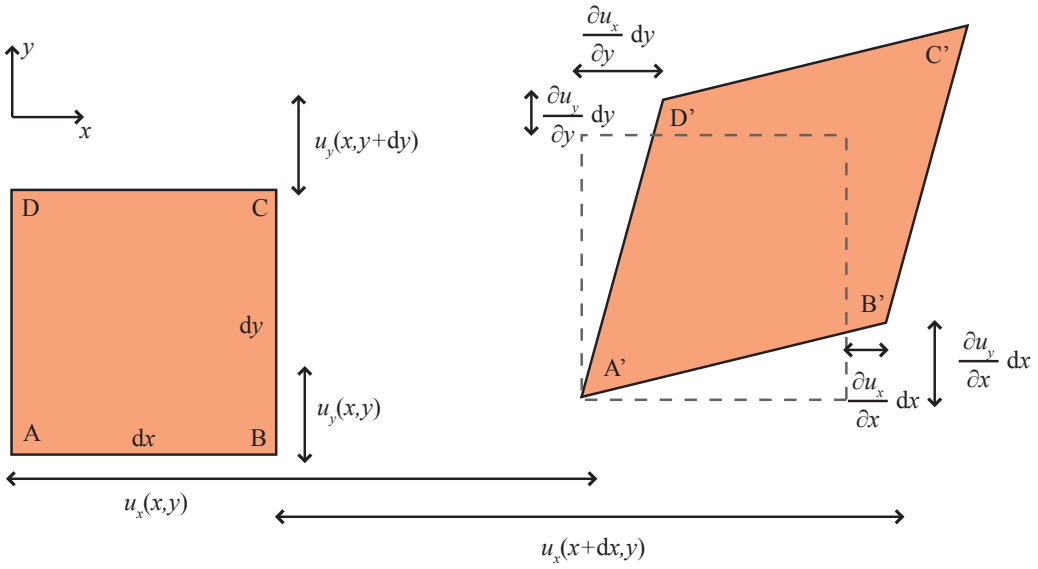

Figure 2.8.: **Schematic representation of the two-dimensional strain.** (Inspired by ref.[100])

The components ϵ_{ij} can be calculated by the derivative of the displacement u with respect to the position x.[87,100] In the one-dimensional case the strain is simply given by the change of a length L divided by the original length L_0[100]

$$\epsilon = \frac{L - L_0}{L_0}. \tag{2.11}$$

In Figure 2.8 the 2D case is schematically illustrated:[100] When a point in a planar body at (x, y) is displaced by $u_{x,y}$ to $(x + u_x, y + u_y)$, the sides of the planar body having a length of $\mathrm{d}x$ and $\mathrm{d}y$ change in length and are not longer orthogonal. The point which was originally at $(x + \mathrm{d}x, y)$ is then at the position $(x + \mathrm{d}x + u_x + \frac{\partial u_x}{\partial x}\mathrm{d}x, y + u_y + \frac{\partial u_y}{\partial x}\mathrm{d}x)$.[100] The other points are given in an analogous way (see Figure 2.8). The one-dimensional strain in x direction is then according to Equation 2.11

$$\epsilon_x = \frac{\mathrm{d}x\left(1 + \frac{\partial u_x}{\partial x}\right) - \mathrm{d}x}{\mathrm{d}x} = \frac{\partial u_x}{\partial x}. \tag{2.12}$$

In the most general form the components of the strain tensor of Equation 2.10 are hence given by[87]

$$\epsilon_{ij} = \frac{1}{2}\left(\frac{\partial u_i}{\partial x_j} + \frac{\partial u_j}{\partial x_i}\right). \tag{2.13}$$

Hookean Solid

A Hookean solid is a perfectly elastic material. It obeys Hooke's law which states that the force is linearly proportional to the deflection. The Hookean solid hence reacts on an applied stress directly without any time delay. In the stress strain notation it holds[87]

$$\boldsymbol{\sigma} = \boldsymbol{G} \cdot \boldsymbol{\epsilon} \tag{2.14}$$

where the proportionality factor $\boldsymbol{G}$ is in the most general situation a 4th order elasticity tensor which is a material constant and describes the anisotropy of a material.[87] Analogous to the orthogonal and shear stresses introduced earlier, in literature, one often distinguishes between the Young's modulus E and shear modulus G. As given by the name, the shear modulus is defined by the ratio of shear stress to shear rate. The Young's modulus describes the situation when a normal, uniaxial stress or strain is applied to an isotropic solid material.[87,100] It describes the stiffness of the material and is given by $E = \sigma/\epsilon$. For an isotropic material in a one-dimensional case, Equation 2.14 simplifies to

$$\sigma = g\epsilon \tag{2.15}$$

where g is the spring constant. This case is usually visualized by a harmonic spring.[87]

Newtonian Fluid

The counterpart to the Hookean Solid is the Newtonian fluid which describes a perfectly viscous material. Here, the shear stresses $\boldsymbol{\tau} = \sigma_{ij}$ $(i \neq j)$ are linearly proportional to the strain rates,[87]

$$\boldsymbol{\tau} = \eta \boldsymbol{D} \tag{2.16}$$

where η is the viscosity and $\boldsymbol{D}$ is the strain rate vector,[87]

$$D_{ij} = \frac{\partial \epsilon_{ij}}{\partial t} \tag{2.17}$$

$$= \frac{\partial \dot{u}_i}{\partial x_j} + \frac{\partial \dot{u}_j}{\partial x_i}. \tag{2.18}$$

A Newtonian fluid reacts on an applied stress with a time delay and the deformation of the Newtonian fluid is not reversible.

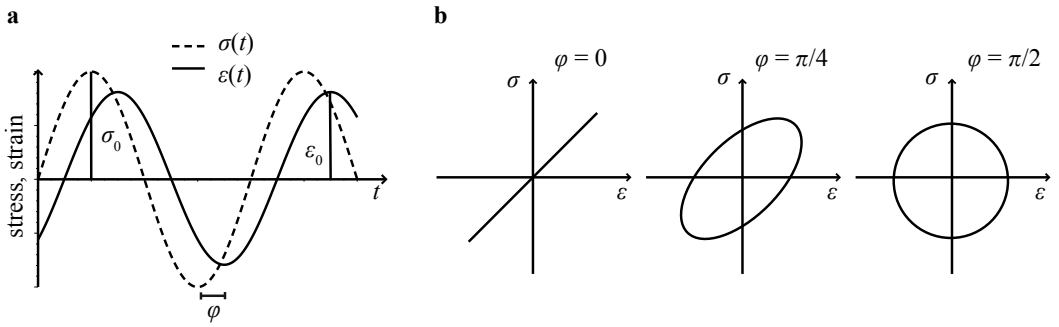

Figure 2.9.: **Harmonic stress-strain relationship.** a) Stress $\sigma(t)$ and strain $\epsilon(t)$ versus time t showing the amplitudes of the oscillations σ_0 and ϵ_0 and the phase separation φ between stress and strain. b) Lissajou curves: $\sigma(t)$ versus $\epsilon(t)$ for three different conditions. From left to right: perfect elastic material ($\varphi = 0$), viscoelastic material ($0 < \varphi < \pi/2$) and perfect viscous material ($\varphi = \pi/2$).

2.3.2. Response of a Viscoelastic Body to Harmonic Strain or Stress

In rheology, timescales are very important. A body can show different physical responses depending on the velocity of the applied stress or strain. In order to study the dynamic material response especially at shorter timescales (seconds), harmonic oscillating stress or strain can be applied. A viscoelastic material that is subjected to a sinusoidal stress with a specific frequency ω will show a harmonic strain response at the same frequency with a phase shift φ between 0 and $\pi/2$. This is also the case if a harmonic strain is applied and the stress is the measured variable.[87] This time-dependent behavior of stress and strain is depicted in Figure 2.9a.

For convenience, one can describe the dynamic functions of strain and stress in complex space,[59,76]

$$\epsilon(t) = \epsilon_0 \exp(i\omega t) \tag{2.19}$$

$$\sigma(t) = \sigma_0 \exp(i\omega t + \varphi) \tag{2.20}$$

where ϵ_0 is the amplitude of the strain and σ_0 is the amplitude of the stress.

A viscoelastic material can then be characterized by the so-called complex modulus $G^*(\omega)$ which is obtained by[59,76]

$$G^*(\omega) = \frac{\sigma(t)}{\epsilon(t)} = G' + iG''. \tag{2.21}$$

G' is the real part of G^* and describes the elastic part of the system, it is called the

elastic modulus or storage modulus as it represents the storage of elastic energy in the interface. The imaginary part of the complex modulus is the viscous modulus or loss modulus G'', which describes loss of energy due to viscous forces. Combining Equations 2.19 to 2.21 results in

$$G' = \frac{\sigma_0}{\epsilon_0}\cos(\varphi) \tag{2.22}$$

$$G'' = \frac{\sigma_0}{\epsilon_0}\sin(\varphi). \tag{2.23}$$

In a purely elastic material (such as the Hookean spring) the phase shift between stress and strain is $\varphi = 0$, resulting in $G^* = G'$. A purely viscous material however results in $G^* = G''$ and $\varphi = \pi/2$. This can be visualized by Lissajou curves that display the time-dependent stress versus the time-dependent strain (see Figure 2.9b). Viscoelastic materials possessing both viscous and elastic components, have Lissajou curves that have a shape of an ellipse.[59,76]

2.3.3. Linear Rheological Spring-Dashpot Models

Viscoelastic materials can be understood as mixtures of a perfect Hookean solid and a perfect Newtonian fluid. In order to model the dynamic behavior of such materials, several one-dimensional models were presented combining the properties of a Hookean spring, representing the elastic part, with a dashpot filled with a Newtonian fluid, representing the viscous part. This is analogous to the behavior of electric circuits over time. The simplest way would be to combine a spring and a dashpot in a linear way - the Maxwell model - or a parallel way - the Kelvin-Voigt model.[87]

Maxwell Model

The schematic idea of the Maxwell model is shown in Figure 2.10a. This mechanical model combines the spring and the dashpot in a series connection and therefore both elements experience the same imposed stress whereas the total strain is the sum of the strains in both elements. This means[58,76]

$$\sigma = \sigma_s = \sigma_d \tag{2.24}$$

$$\epsilon = \epsilon_s + \epsilon_d \tag{2.25}$$

where the subscript s corresponds to the spring element and d corresponds to the dashpot element. The complete system can hence be described by a single equation

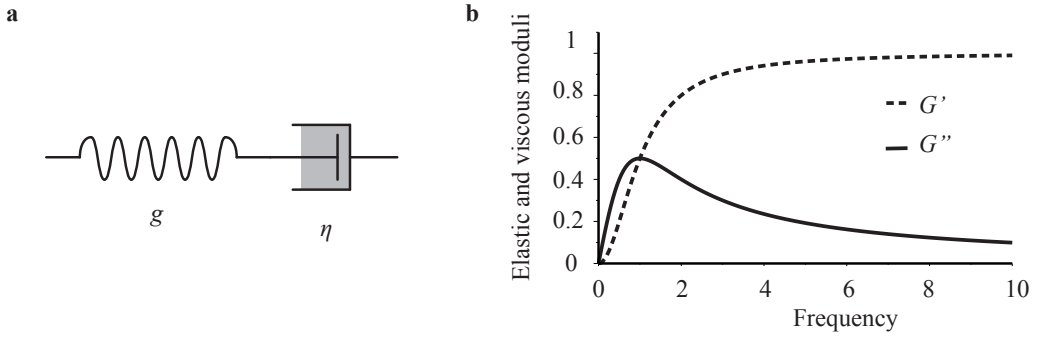

Figure 2.10.: **Maxwell model.** a) Schematic model: A serial connection of a spring with a spring constant g and a dashpot filled with a Newtonian liquid with a viscosity η. b) Elastic modulus G' and viscous modulus G'' of the Maxwell model responding to oscillatory strain/stress with respect to the frequency assuming that $g = 1$ and $\eta = 1$.

when one differentiates Equation 2.25 and includes the stress-strain Equations 2.15 and 2.16 of the spring and the dashpot[58,87]

$$\dot{\epsilon} = \frac{\dot{\sigma}}{g} + \frac{\sigma}{\eta}. \tag{2.26}$$

The Maxwell model is the simplest model describing a non-Newtonian fluid.

When confronted with an oscillatory stress or strain as introduced in Section 2.3.2, the elastic and viscous moduli can be calculated by inserting Equations 2.19 and 2.20 in the constitutive equation of the Maxwell model (Equation 2.26). This results in[58,87]

$$i\omega\epsilon(t) = \frac{1}{g} i\omega\sigma(t) + \frac{1}{\eta}\sigma(t). \tag{2.27}$$

The complex modulus is then

$$G^* = g\left(\frac{i\omega\tau}{1+i\omega\tau}\right) \tag{2.28}$$

$$= g\frac{\omega^2\tau^2}{1+\omega^2\tau^2} + ig\frac{\omega\tau}{1+\omega^2\tau^2} \tag{2.29}$$

where $\tau = \eta/g$ is the relaxation time. Figure 2.10b displays the elastic and viscous moduli G' and G'' with respect to the frequency ω in the simple case where $g = 1$ and $\eta = 1$.

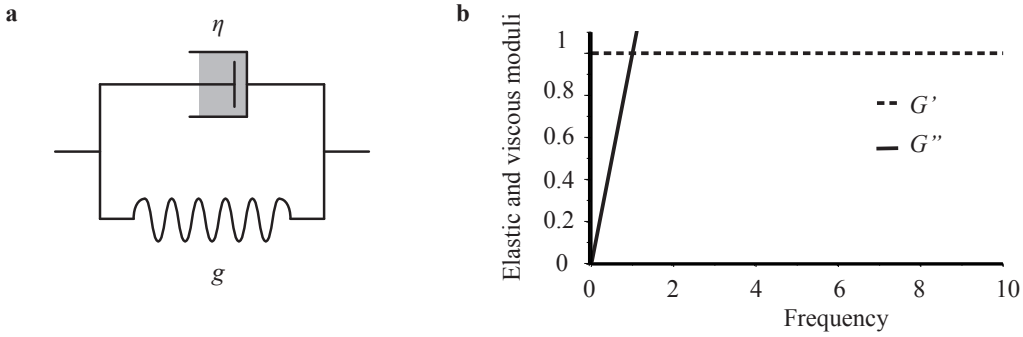

Figure 2.11.: **Kelvin-Voigt model.** a) Schematic model: A parallel connection of a spring with a spring constant g and a dashpot filled with a Newtonian liquid with a viscosity η. b) Elastic modulus G' and viscous modulus G'' of the Kelvin-Voigt model responding to oscillatory strain/stress with respect to the frequency assuming that $g = 1$ and $\eta = 1$.

Kelvin-Voigt Model

The Kelvin-Voigt model is useful for elastic materials having a weak viscous contribution. It combines a spring element and a dashpot element in a parallel way as shown schematically in Figure 2.11a. Here, the total stress is a sum of both elements[58,87]

$$\sigma = \sigma_s + \sigma_d \tag{2.30}$$

while the total strain experienced by spring and dashpot is the same

$$\epsilon = \epsilon_s = \epsilon_d. \tag{2.31}$$

The constitutive equation of the Kelvin-Voigt model can hence be obtained by simply combining the respective stress-strain Equations 2.15 and 2.16, yielding[58,87]

$$\sigma = g\epsilon + \eta\dot{\epsilon}. \tag{2.32}$$

The experimental results of the dynamic frequency-dependent harmonic stress/strain response may be modeled with the Kelvin-Voigt model. The following behavior is then expected for an oscillating stress or strain by inserting Equations 2.19 and 2.20 in the constitutive Equation of the Kelvin-Voigt model 2.32:[58,87]

$$\sigma(t) = g\epsilon(t) + i\eta\omega\epsilon(t) \tag{2.33}$$

yielding

$$G^* = \frac{\sigma(t)}{\epsilon(t)} \tag{2.34}$$

$$= g + i\omega\eta \tag{2.35}$$

where $G' = g$ is constant and $G'' = \omega\eta$ is proportional to the frequency with the viscosity being the proportionality factor.[58,87] Figure 2.11b displays the elastic and viscous moduli G' and G'' with respect to the frequency ω in the simple case of $g = 1$ and $\eta = 1$.

2.3.4. Interfacial Shear and Dilational Rheology

So far, rheology was introduced as being a bulk property. However interfaces have two dimensional viscoelastic properties as well. One has to distinguish between interfacial shear rheology and interfacial dilational rheology. Whereas in the former case, the reaction of the material to shear forces is of interest, the latter case studies the influence of changes of the available area. The principle idea behind interfacial and bulk rheology is the same, however there are also differences one has to consider. For example, in contrast to bulk, interfaces can be compressed easily. Therefore the dilational properties of interfaces are more important than in bulk, which is mostly incompressible.[93] Another difference to measurements of bulk is that mass is not always conserved.[93] Especially in adsorbed Gibbs monolayers, surfactant molecules are present in the bulk subphase and can adsorb to the interface during dilational measurements when the available surface area is increased.

In interfacial rheology, 2D surfactant films are investigated using harmonic stress-strain relationships, the theory of which was explained in Section 2.3.2. At interfaces, any deformations can be measured by the change in the surface tension. We can understand this dynamic surface tension as the two-dimensional surface stress.[93] Interfacial rheology allows the calculation of interfacial elastic and viscous moduli and interfacial viscosities. In all cases, these parameters describe only the in-plane deformations of interfaces. Out-of plane deformations such as bending are not taken into account and can mostly be neglected when we consider a flat monolayer in a Langmuir trough.

The two methods, interfacial shear and dilation rheology, provide different, complementary information about the physical properties of the film. In interfacial dilational rheology, the surface area of a film is changed periodically and the corresponding surface pressure response is recorded. The resistance of the interfacial

layer to compression and expansion is measured. In interfacial shear rheology measurements, the shape of the interface is changed and the mechanical strength of the interfacial film is measured while keeping the area and the surface tension constant.[76] In principle it is possible to perform interfacial rheology measurements on both, adsorbed Gibbs monolayers and Langmuir monolayers. Here, the focus is set on Langmuir monolayers.

There are different experimental setups which allow the execution of interfacial rheological measurements. In the following, the setups used in this study are shortly presented.

Interfacial Shear Rheology

An interfacial shear rheometer (ISR) can be used to investigate the response of the interfacial film to shear strain. The calculation of the elastic and viscous moduli are analogous to the bulk situation which was explained above with the difference that all equations have to be transferred to the 2D case: The stress is hence acting along a length not a surface.

There are different ISR setups on the market and one has to distinguish between two different types of instruments: Controlled stress rheometers regulate the forces exerted on the sample and controlled strain rheometers regulate the angular displacement. The oldest commercial setup is the CIR-100 (Camtel, Royston, UK). It is capable of both methods and is based on a du Noüy ring. The du Noüy ring is made out of thin Platinum wire ($d_{\text{wire}} \approx 1\,\text{mm}$, $d_{\text{ring}} = 1.2\,\text{cm}$) which is positioned directly at or slightly below the interface. At oscillation frequencies below the natural frequency 2 Hz, the ring oscillates at an applied torque and the ISR works in the controlled strain regime. The instrument records the phase difference and amplitude ratio between the input stress and output strain. The elastic and viscous moduli G' and G'' are directly calculated by the instrument taking the feedback signals and geometry of the experimental setup into account. The free parameters to be varied are the oscillation amplitude and frequency.[76]

Combining an ISR with a film balance allows to measure the shear elastic and viscous moduli at a certain surface pressure.

Interfacial Dilational Rheology

Dilational rheology is a method mainly used for interfaces which are often highly compressible in contrast to bulk. In interfacial dilational rheology, the surface area of the monolayer is changed periodically resulting in a dilational strain. This can be

achieved using a Langmuir film balance equipped with two movable barriers which oscillate (Figure 2.1). The Langmuir monolayer is first compressed isothermally to a distinct surface pressure π_0 and then the viscoelastic properties can be monitored by oscillating the surface area over time according to[93]

$$A(t) = A(1 + u_0 \sin(\omega t + \varphi_u)) \tag{2.36}$$

$$= A(1 + u(t)) \tag{2.37}$$

where A is the initial molecular area, u_0 is the strain amplitude, $\omega = 2\pi f$ is the oscillation frequency and φ_u the phase shift. In a linear system, the response of the surface pressure is also sinusoidal and can be measured by the Wilhelmy plate:

$$\pi(t) = \pi_0 + \pi_1 \sin(\omega t + \varphi_\pi) \tag{2.38}$$

where π_1 is the amplitude of the surface pressure response and φ_π the phase shift. The total stress-strain phase shift is given by $\varphi = \varphi_\pi - \varphi_u$. The free parameters that can be varied are the strain amplitude and the frequency.[93]

During the measurement, the area oscillation as well as the oscillation of the surface pressure are recorded. This allows the calculation of the dilational elastic and viscous moduli which are designated by E' and E'', respectively, in order to distinguish them from the elastic and viscous moduli obtained from interfacial shear rheology, G' and G''. Using the calculation from above, it holds that[58,93]

$$E' = \frac{\pi_1}{u_0} \cos\varphi \tag{2.39}$$

$$E'' = \frac{\pi_1}{u_0} \sin\varphi. \tag{2.40}$$

Another method to measure the interfacial dilational rheological properties which is not applied in this thesis is using a bubble tensiometer where the monolayer is at the air/water interface of a pending drop. The area of the interface can be periodically changed by varying the drop volume. The surface pressure can be monitored by video recording of the drop shape.

2.3.5. Nonlinear Rheology

Often, viscoelastic, complex interfaces may respond in a nonlinear way to applied single harmonic strain, especially when the strain amplitudes are high.[39,41,108] The reason for the rise of nonlinearity are diverse but most often arise from changes in

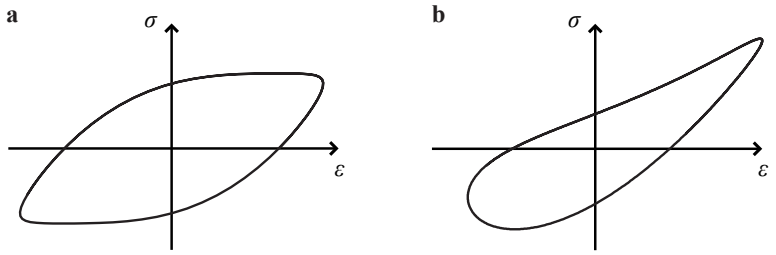

Figure 2.12.: **Lissajou curves of nonlinear stress responses.** (a) The stress response includes an additional uneven mode, (b) the stress response includes an additional even mode.

the structural order of the interface.[92] Most studies try to avoid measurements in the nonlinear regime in order to avoid difficulties in the analysis. In the last decades, several approaches were published to analyze viscoelastic responses in the nonlinear regime.[41,92,108]

A first hint of the nonlinearity of the response function is given by the shape of the Lissajou curves where the stress is displayed with respect to the strain. A perfectly linear signal would result in an elliptical shaped Lissajou curve whereas a nonlinear stress response can lead to various shapes as exemplarily shown in Figure 2.12.

The most straightforward method to quantify the nonlinear response is Fourier-Transform rheology.[108] Here, the oscillation of the stress response $\sigma(t)$ is fitted by a Fourier series expansion

$$\sigma(t) = \sum_{k=1}^{n} \sigma_k \exp(ki\omega t) \tag{2.41}$$

where σ_k are the amplitudes of the k-th modes. The further calculations are based on the situation where the input strain $\epsilon(t)$ is strictly harmonic with the frequency ω. In interfacial shear rheology measurements, only odd modes appear whereas in interfacial dilational rheology experiments, both even and odd modes can be observed.[92] The following paragraphs focus on the general case, including both, even and odd modes in the analysis. The first mode allows the calculation of the linear elastic and viscous moduli using Equation 2.22 and 2.23. The higher modes can be analyzed in terms of contribution from elastic and viscous parts.

Coming from the definition of elasticity in terms of a Hookean spring and viscosity from Newton's law, we can obtain more information about materials with a predominantly nonlinear elastic or predominantly nonlinear viscous response. A purely

elastic nonlinear stress response should be odd under reflection because of mirror symmetry, meaning that

$$\sigma_E(t) = \sum_{k,odd}^{n} g_k \epsilon^k(t) \tag{2.42}$$

$$= g_1\epsilon + g_3\epsilon^3 + g_5\epsilon^5 + \dots \tag{2.43}$$

where g_1 is the spring constant in the one-dimensional case and g_k ($k > 3$) are proportionality factors of the higher modes. Such a behavior is depicted as a Lissajou curve in Figure 2.12a for $g_3 = 0.1g_1$, including a linear viscous term.

A nonlinear viscous response on the other hand can have even and odd components and depends on the frequency

$$\sigma_V(t) = \sum_{k}^{n} \eta_k \dot{\epsilon}^k(t) \tag{2.44}$$

$$= i\omega\eta_1\epsilon - \omega^2\eta_2\epsilon^2 - i\omega^3\eta_3\epsilon^3 + \dots. \tag{2.45}$$

η_k describes the (nonlinear) interfacial viscosity. In contrast to the purely elastic response, the viscous response also contains imaginary components. This leads to an asymmetric response as visible in the Lissajou curve in Figure 2.12b which shows the stress/strain relationship of a viscoelastic body exhibiting a second Fourier mode with $\eta_2 = 0.1\eta_1$ in the viscous part whereas the elastic part is strictly linear.

This way, the thorough analysis of the Fourier modes obtained from fitting the stress response to a Fourier series expansion can provide precious information about the material. Several statements can be made:

1. The existence of mainly odd modes with infinitesimal low even modes suggest a predominantly elastic behavior.

2. The existence of mainly odd modes also indicates that the interface is isotropic, as the surface stress tensor should be symmetric ($\boldsymbol{\sigma}(-\boldsymbol{\epsilon}) = -\boldsymbol{\sigma}(\boldsymbol{\epsilon})$).[93]

3. The appearance of increased even modes may indicate an increased nonlinear viscous contribution.

4. The exact portion of the contribution of the viscosity can be obtained by analyzing the frequency dependence of the higher modes. A predominantly nonlinear viscous material shows frequency-dependent higher Fourier-modes.

The drawback of nonlinear rheology is the lack of nonlinear models that adequately describe nonlinear effects in interfacial rheology. Therefore the interpretation of nonlinear responses are limited. This is especially true as 2D films of different kinds of surfactants such as lipids[4], polymers[39] or nanoparticles[110] can form various types of phases from fluids to gels and crystalline phases, that behave completely different. It would be of great interest for the interfacial rheology community to find a way to connect the information about the nonlinearity to in-plane dynamic processes of the interfacial layers.[93]

To quantify the degree of nonlinearity, one can calculate the value of the total harmonic distortion (THD) which is the ratio of the sum of the powers of the higher mode amplitudes to the power of the first, fundamental frequency mode:

$$\mathrm{THD} = \frac{1}{\sigma_1}\sqrt{\sum_{k>1}^{n}\sigma_k^2}. \tag{2.46}$$

In literature, THD is often given in dependence of frequency, amplitude and surface concentration. Typically, the nonlinearity is independent of the frequency, whereas it often increases with amplitude and surface concentration.[106]

2.4. Grazing-Incidence Small-Angle X-Ray Spectroscopy (GISAXS)

A unique method to study nanostructured surfaces is GISAXS which combines the methods of small-angle scattering and grazing-incidence diffraction using X-rays.[79] It is especially sensitive to the structure and morphology of surfaces.[2] In the following, the basic principles will be explained in detail.

2.4.1. Principles of X-ray Scattering from Surfaces

If an X-ray beam in vacuum or air (refractive index n_0) impinges a completely smooth surface composed of a material with a refraction index n at an incidence angle α_i with the intensity I_0, we can observe refraction and reflection (Figure 2.13).[2] The angle of the reflected beam corresponds to the angle of the incident beam, $\alpha_f = \alpha_i$. The angle of the transmitted/refracted beam however depends on the refractive index of the material following Snell's law,[89]

$$n_0 \cos(\alpha_i) = n \cos(\alpha_t). \tag{2.47}$$

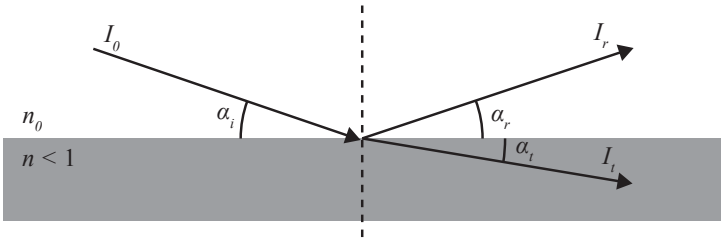

Figure 2.13.: **Refraction and reflection of an X-ray beam at an interface.** The X-ray beam with intensity I_0 impinges the interface of a material with $n < 1$ at the angle α_i. A part of the beam ($|r|^2 \cdot I_0$) is reflected at the angle α_r. Another part (with intensity $|t|^2 \cdot I_0$) is transmitted and refracted at the angle α_t.

The Fresnel's coefficients r and t allow the calculation of the intensities of the transmitted (I_t) and reflected beam (I_r) with respect to the incident beam,

$$\frac{I_r}{I_0} = |r|^2 \tag{2.48}$$

$$\frac{I_t}{I_o} = |t|^2, \tag{2.49}$$

where, in the case of X-rays,[89]

$$r = \frac{\sin(\alpha_i) - n\sin(\alpha_t)}{\sin(\alpha_i) + n\sin(\alpha_t)} \tag{2.50}$$

$$t = \frac{2\sin(\alpha_i)}{\sin(\alpha_i) - n\sin(\alpha_t)}. \tag{2.51}$$

In general, the refractive index is a complex value and depends on the wavelength λ. The real part accounts for the behavior of the transmitted beam, the imaginary part describes the extinction of the beam in the material. Whereas for visible light, the real part of the refractive index is normally $n > 1$, for X-rays, the refractive index of materials is in general $n \leq 1$ but positive.[89] It is normally denoted as[2,79,89]

$$n(\lambda) = 1 - \delta(\lambda) + i\beta(\lambda) \tag{2.52}$$

where the real component δ describes the dispersion and the imaginary component

β describes the absorption of the incident wave. They are given by[89]

$$\delta = \frac{\rho N_A r_e \lambda^2}{2\pi M} f_1 \tag{2.53}$$

$$\beta = \frac{\rho N_A r_e \lambda^2}{2\pi M} f_2. \tag{2.54}$$

ρ is the density, N_A is the Avogadro constant ($6.022 \times 10^{23}\,\mathrm{mol}^{-1}$), r_e is the classical electron radius ($2.82 \times 10^{-15}\,\mathrm{m}$) and M is the molar mass. f_1 and f_2 are the atomic scattering factors that describe how strongly the atoms in the material refract and absorb the incident X-ray beam. In general, δ is in the order of 10^{-5} and β is in the order of 10^{-6}.[89] For X-rays, any material has a refractive index that is smaller than that of air or vacuum. Therefore when X-rays impinge a material from vacuum, according to Snell's law, the angle of the transmitted beam is smaller than the angle of the incident beam $\alpha_t < \alpha_i$. At very low incident beams, the beam is totally reflected which is called total external reflection. This occurs at the critical angle[2,79,89]

$$\alpha_c \approx \sqrt{2\delta} \tag{2.55}$$

assuming $\beta \ll \delta$. α_c is usually in the order of $0.1° - 0.5°$.[89]

2.4.2. Principles of GISAXS

In GISAXS, the incident angle is chosen close to the critical angle α_c.[89] The principle setup of the scattering geometry is shown in Figure 2.14. The sample surface is in the (x, y)-plane, the z-axis is the surface normal. A beam of wavelength λ with the wavevector $\boldsymbol{k}_i$, $|\boldsymbol{k}_i| = 2\pi/\lambda$ impinges the sample surface with the incident angle α_i. It scatters with the angle α_f. In case of a perfectly flat substrate, one would only observe a specular signal at $\alpha_f = \alpha_i$. However, (nano)structures in the surface lead to off-specular signals at angles $\alpha_f \neq \alpha_i$ and out-of-plane angles θ (Figure 2.14). The scattering wave vector $\boldsymbol{q} = \boldsymbol{k}_f - \boldsymbol{k}_i$ is then given by[79,89]

$$\boldsymbol{q} = \frac{2\pi}{\lambda} \begin{pmatrix} \cos(\theta)\cos(\alpha_f) - \cos(\alpha_i) \\ \sin(\theta)\cos(\alpha_f) \\ \sin(\alpha_i) + \sin(\alpha_f) \end{pmatrix}. \tag{2.56}$$

For specular scattering, $q_x = q_y = 0$, so only information along the z-axis (height) is gathered. Off-specular scattering on the other hand provides information about the in-plane structures by $q_\parallel = (q_x, q_y)$ which allows to analyze the structure of the

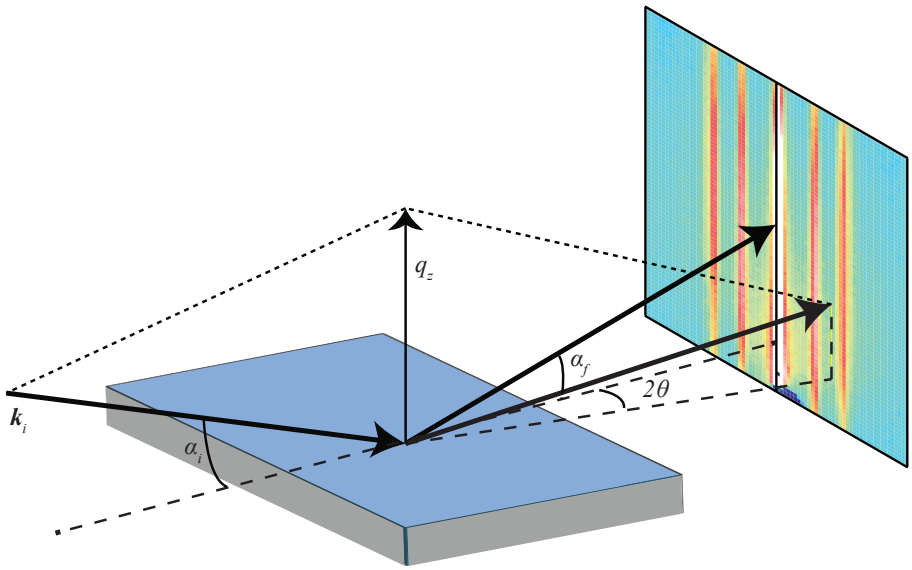

Figure 2.14.: **Schematic setup of GISAXS scattering geometry.** The monochromatic X-ray beam impinges the sample surface at the angle α_i close to the critical angle α_c. The scattered beam is recorded by a 2D detector which allows the determination of the scattering angles α_f in the plane of the incidence beam and θ out of the plane of the incidence beam. In order to detect the rather weak scattering signals, a beam stop is used to cover the signal of the direct, reflected beam.

interface. The intensity $I(q_\parallel)$ along $q_\parallel$ is given by

$$I(q_\parallel) = A|F(q_\parallel)|^2 S(q_\parallel) \tag{2.57}$$

where A is a scaling factor. $F(q_\parallel)$ is the form factor, which provides information about the shape of the scattering particles and $S(q_\parallel)$ the structure factor which describes the lateral organization of the particles. In the following, form factor and structure factor will be explained in more detail.

Form Factor

For non-interacting particles in a dilute system, the scattering intensity would only be described by the form factor which accounts for the shape and the size of the particles. In the most general form where only one particle is scattered, it is given by integrating the scattering length density $\rho(\boldsymbol{r})$ over the volume V of the particle (Born approximation)[89]

$$F(\boldsymbol{q}) = \int_V \rho(\boldsymbol{r}) \mathrm{e}^{i\boldsymbol{q}\cdot\boldsymbol{r}} \mathrm{d}V. \tag{2.58}$$

In the case of GISAXS, where small interfaces are studied, besides the normal scattering, three other scattering events can occur which are illustrated in Figure 2.15: A reflection followed by a scattering, a scattering followed by a reflection and a reflection followed by a scattering and a second reflection. These 4 scattering events have to be taken into account for the calculation of the form factor which is the case in the framework of the distorted-wave Born approximation (DWBA). Here the form factor is given by[79,89]

$$\begin{aligned} F(q_\parallel) = {} & F(q_\parallel, (\boldsymbol{k}_f - \boldsymbol{k}_i)_z) + r_i F(q_\parallel, (\boldsymbol{k}_f + \boldsymbol{k}_i)_z) \\ & + r_f F(q_\parallel, -(\boldsymbol{k}_f + \boldsymbol{k}_i)_z) + r_i r_f F(q_\parallel, -(\boldsymbol{k}_f - \boldsymbol{k}_i)_z). \end{aligned} \tag{2.59}$$

r_i and r_f are the Fresnel coefficients of the refraction as shown in Fig. 2.15 (cf. Equation 2.50).

Structure Factor

Ordered particles at the interface will show a scattering pattern that needs besides the form factor $F(q)$ a structure factor $S(q)$ to describe the intensity profile. The structure factor accounts for the organization of the particles and their interaction with each other. In the general case with a homogeneous layer of particles on a

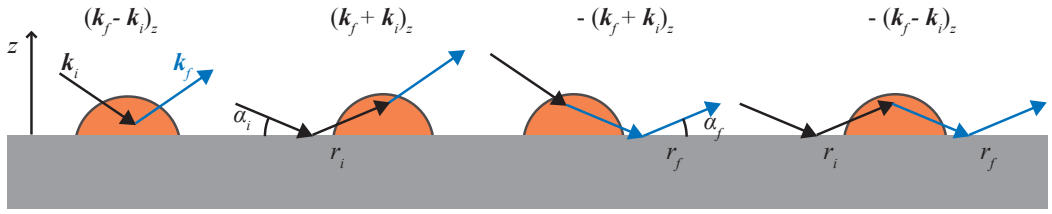

Figure 2.15.: **Scattering events on particles occurring in GISAXS experiments.** From left to right: direct reflection at the particle, reflection followed by a scattering, scattering followed by a reflection and reflection followed by a scattering and a second reflection. These four scattering events are considered in the DWBA. The black arrows indicate the incoming beams with wave vector $\boldsymbol{k}_i$, the blue arrows indicate the scattered beams with wave vectors $\boldsymbol{k}_f$. The wave vector transfer of each event is written on the top. The Fresnel coefficients r_i and r_f are marked. (inspired by ref.[89])

flat substrate forming dense domains, the reduced partial pair correlation functions $g_{\alpha\beta}(r_\parallel)$ can describe the structure factor. $g_{\alpha\beta}(r_\parallel)$ describes the relative position of particles of type α with probability density p_α to particles of type β with probability density p_β. When n_S is the number of particles in a surface unit, $n_S p_\beta g_{\alpha\beta}(r_\parallel)\mathrm{d}r_\parallel$ gives the numbers of particles of type β that are at the position $r_\parallel$ of particles of type α. The structure factor is then[89]

$$S(q_\parallel) = 1 + n_S \int_A \left(g_{\alpha\beta}(r_\parallel) - 1\right) \mathrm{e}^{iq_\parallel r_\parallel} \mathrm{d}r_\parallel. \tag{2.60}$$

A drawback in the analysis of the structure factor is the lack of knowledge of the pair-pair correlation functions. Hence, several models exist to describe the surface pattern. The two most common are:[89]

1. Decoupling approximation (DA):
   The DA neglects all kind of correlations between the particles. Here, we can replace the partial pair correlation function by its general form $g(r_\parallel)$.[89]

2. Local monodisperse approximation (LMA):
   In contrast to the DA, the LMA assumes an almost perfect correlation between monodisperse particles having a size larger than the coherence length of the X-ray wave.[89]

The precise fitting of the structure factor allows the calculation of the correlation length ξ between the particles since the structure factor is simply the Fourier trans-

formation of the pair correlation function $g(r)$ in real space. Therefore, within the framework of the short range order model, one can calculate ξ by[94]

$$\xi = \frac{\langle d \rangle^3}{2\delta r^2} \tag{2.61}$$

where $\langle d \rangle$ is the mean distance between two neighboring particles. δr is its root mean square deviation of $\langle d \rangle$ and corresponds to the width of the first correlation peak of $g(r)$. Since the width of the first peak of the structure factor is

$$\delta q_y = \frac{\delta r^2 q_y^2}{\langle d \rangle}, \tag{2.62}$$

the correlation length can be directly obtained by the width of the first peak of the structure factor in reciprocal space δq_y:

$$\xi = \frac{2\pi^2}{\delta q_y}. \tag{2.63}$$

3. Materials and Methods

3.1. Materials

3.1.1. Semifluorinated Alkanes

In this study various semifluorinated $FnHm$ diblocks were studied. n corresponds to the length of the fluorocarbon segment whereas m corresponds to the length of the hydrocarbon segment as described by the chemical structure $C_nF_{2n+1}C_mH_{2m+1}$. The semifluorinated diblocks investigated were $F8H14$, $F8H16$, $F8H18$, $F8H20$, $F10H16$ and $F12H16$. They were synthesized according to Brace et al. and purified by repeated crystallizations from methanol.[10]

Additionally, the semifluorinated tetrablock molecules di($F10H16$), di($F10H18$) and di($F10H20$) were studied which are in general denoted as di($FnHm$) with the chemical structure $(CF_{2n+1}CH_2)(C_{m-2}H_{2m-3})CH{-}CH(C_nF_{2n+1}CH_2)(C_{m-2}H_{2m-3})$. They were synthesized according to de Gracia Lux (2010)[19].

All semifluorinated alkanes were synthesized and provided by lab of Marie Pierre Krafft[1].

The chemical purity was $> 99\,\%$ which they determined by thin-layer chromatography, nuclear magnetic resonance, elemental analysis and MALDI-TOF mass spectroscopy. Throughout this study, double deionized water (MilliQ, Molsheim) with a specific resistance of $\rho > 18\,\mathrm{M\Omega}$ was used.

All semifluorinated alkanes were solved in chloroform with a concentration of 1 mM.

3.1.2. Lipids

The lipid 1,2-dipalmitoyl-sn-glycero-3-phosphocholine (DPPC) used in this study was purchased from Avanti polar lipids Inc. (USA). It consists of a zwitterionic phosphatidylcholine headgroup and two saturated hydrocarbon chains with 16 carbons. Its chemical structure is shown in Figure 3.1a. The molecule has a molecular weight of $734.04\,\mathrm{g\,mol^{-1}}$ and its transition temperature is at $T_m = 41°\mathrm{C}$.

[1] Institut Charles Sadron (CNRS), University of Strasbourg, 67034 Strasbourg, France

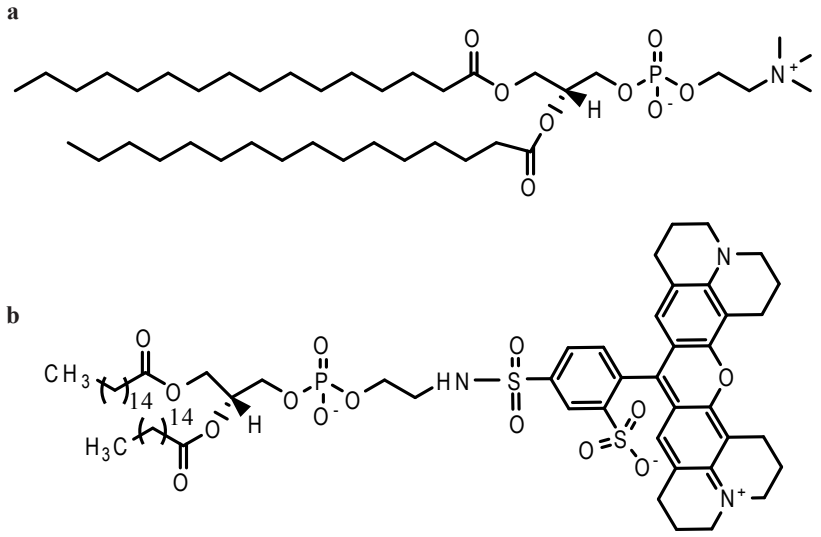

Figure 3.1.: Chemical structure of DPPC (a) and DHPE-Texas-Red (b)

1,2-Dihexadecanoyl-sn-Glycero-3-Phosphoethanolamine (DHPE) marked with Texas Red was purchased from AAT Bioquest (Sunnyvale, CA, USA). Its chemical structure is shown in Figure 3.1b. The zwitterionic headgroup is labeled with the red fluorescent die Texas Red, which has its excitation line at the wavelength $\lambda = 595\,\mathrm{nm}$ and emits light with the wavelength $\lambda = 615\,\mathrm{nm}$.

3.2. Methods

3.2.1. π/A-Isotherms

π/A-isotherms were recorded with a KSV Nima film balance with two motor-driven movable barriers (Bioloin Scientific, Stockholm, Sweden). All experiments were performed at room temperature (20°C). Before the usage, the Langmuir trough and the barriers were cleaned by wiping the surface with ethanol and rinsing it at least 10 times with deionized water.[2] The different compounds were solved in chloroform with a concentration of 1 mM. 40 µl of the solution was spread on the water surface using a Hamilton syringe. The experiments were started after $10 - 15\,\mathrm{min}$ to allow the chloroform to evaporate and the monolayer to equilibrate. The monolayer was then compressed at a constant rate of $3.75\,\mathrm{cm^2\,min^{-1}}$ until the collapse or the minimum available surface area was reached.

[2] All experiments were performed with doubled deionized water with a resistivity $\rho > 18\,\mathrm{M\Omega}$ (MilliQ, Molsheim, Germany)

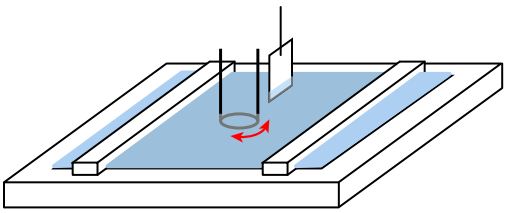

Figure 3.2.: Schematic experimental setup of the ISR combined with a film balance.

3.2.2. Interfacial Shear Rheology

To measure the interfacial shear rheology, a CIR-100 interface rheometer (Camtel Inc., UK) was used which was custom modified to accommodate a Langmuir film balance (NIMA, UK). The du Noüy ring was immersed 0.05 mm below the water surface as here, the sensitivity to the monolayer was maximal. For each measurement, reference measurements on a pure air/water interface were recorded and subtracted from the actual data. The statistical uncertainties of the elastic and viscous moduli G' and G'' were estimated from the standard deviation of 10 data points. All measurements were performed at room temperature ($T = 20°\mathrm{C}$).

The $FnHm$ molecules were solved in chloroform with a concentration of 1 mM and spread on the air/water interface of the film balance after the du Noüy ring was placed. After the evaporation of the chloroform ($\sim 15\,\mathrm{min}$), the monolayers were compressed to the desired surface pressure with a speed of $5\,\mathrm{cm^2\,min^{-1}}$. The surface pressure was then kept constant during the shear rheology measurements (which sometimes resulted in a further compression of the film). Usually, an oscillation amplitude of 1.5 mrad was applied at the frequency range $1 - 10\,\mathrm{Hz}$.

3.2.3. Interfacial Dilational Rheology

For the dilational rheology measurement, a KSV Nima film balance with two motor-driven movable barriers was used (Bioloin Scientific, Stockholm, Sweden). The monolayer was prepared as described in Section 3.2.1. Unless stated otherwise, it was compressed to a surface pressure of $5\,\mathrm{mN\,m^{-1}}$ with a speed of $3.75\,\mathrm{cm^2\,min^{-1}}$ and the monolayer was allowed to equilibrate for another 10 min. The barriers were sinusoidally oscillated at a defined frequency and amplitude while recording the area $A(t)$ and the surface pressure $\pi(t)$ according to Equation 2.36. Unless stated otherwise, the experiments were performed at the amplitude of $u_0 = 0.01$ in the frequency

regime of $1 - 150\,\mathrm{mHz}$.[3] All measurements were performed at room temperature ($T = 20°\mathrm{C}$). The elastic and viscous moduli E' and E'' could then by calculated as described in Section 2.3.4. All experiments were at least performed three times.

A part of the experiments was performed in an atmosphere enriched with perfluorohexane (C_6F_{14}, PFH) instead of air. PFH was purchased from Apollo Scientific Ltd (Bredbury, UK). A flow of N_2 gas was led through three subsequent washing bottles filled with liquid PFH into the gas-tight box of the film balance for at least 30 min. Since the saturation of PFH was accompanied by an increase in surface pressure to $2.5 - 3\,\mathrm{mN\,m^{-1}}$, the surface pressure was manually set to $0\,\mathrm{mN\,m^{-1}}$ prior to the compression.

3.2.4. GISAXS

GISAXS experiments were performed at ID10 beam line of the European Synchroton Radiation Facility (ESRF, Grenoble, France). A gas-tight film balance filled with PFH-enriched He atmosphere was used for the preparation of $FnHm$ monolayers. Therefore, a flow of He gas was led through three subsequent washing bottles filled with PFH into the gas-tight box of the film balance. The saturation of PFH in the gas phase was confirmed by an increase of the surface pressure by $2.5 - 3\,\mathrm{mN\,m^{-1}}$. All experiments were performed at room temperature ($T = 20°\mathrm{C}$). The monolayer was compressed to the surface pressure of $5\,\mathrm{mN\,m^{-1}}$, and a monochromatic X-ray beam (22 keV) impinged on the interface at an incidence angle of 0.045°, which is slightly below the critical angle of total external reflection. The intensity of the scattering signal was detected using a 2D-pixel detector. To obtain the one-dimensional scattering profile along the scattering vector parallel to the interface $q_{\parallel} \approx q_y$, the scattering intensity was averaged over $q_z = 0.9 - 1.1\,\mathrm{nm^{-1}}$. The experimental GISAXS data were analyzed using the FitGISAXS software.[5] The data were treated within the framework of the DWBA by applying the implemented functions for monodisperse oblate hemispheroids arranged in a hexagonal paracrystal or monodisperse oblate hemiellipsoids arranged in a rectangular paracrystal. The structure factors $S(q_y)$ and form factors $F(q_y)$ were obtained by optimizing the background intensity, scaling factor A, diameter D, height H and lattice constant L. Finally, the best fit was achieved by letting all parameters float.

[3] This combination of amplitude and frequency results in a oscillation velocity which is in the same order of magnitude as the oscillation applied in the interfacial shear rheology measurements ($10^{-2} - 10^{-4}\,\mathrm{cm\,s^{-1}}$).

3.2.5. Fluorescence Microscopy and Analysis with the Radial Distribution Function

The fluorescence microscopy experiments were performed using a Nikon TE2000-U microscope (Shinagawa, Japan) in combination with an EXFO X-cite 120 Metal Halide lamp (Excelitas, Waltham, United States). The Langmuir trough was equipped with a small window and mounted on the microscope allowing the observation of the film from below. The DPPC solution was mixed with 0.1 mol % of DHPE-Texas Red.

The fluorescent images were analyzed using ImageJ, Fiji. For a selection of images, the radial distribution function $g(r)$ was calculated,

$$g(r) = \frac{1}{\rho}\frac{1}{2\pi r}\frac{\mathrm{d}n(r)}{\mathrm{d}r} \tag{3.1}$$

where ρ is the density of particles and $n(r)$ is the number of particles in a infinitesimal small annulus of the area $2\pi r\mathrm{d}r$. It hence describes all pair correlations between the particles. To this end, the fluorescent images were binarized and the maximum position of each particle was detected allowing the calculation of $g(r)$.

3.2.6. Langmuir-Blodgett

With the Langmuir-Blodgett (LB) technique, molecular films can be transferred from the liquid/gas interface to a solid substrate. In this study, it was used to prepare a monolayer of $F12H16$ on a silicon wafer with native oxide (SiMat, Landsberg, Germany). The Si wafer was thoroughly cleaned by successive sonication with acetone, ethanol, methanol and water for 15 min each. In order to increase the hydrophilicity of the surface which is crucial for the deposition of the $F12H16$ surface domains, RCA cleaning was performed: The wafers were first sonicated for 3 min and then incubated for another 30 min at 60°C in a solution of H_2O_2, NH_3 and H_2O (volume ratio 1:1:5). Finally, the wafers were rinsed with deionized water at least 10 times and were put in the oven at 70°C to dry.

A Langmuir trough equipped with a deep basin that allowed Langmuir-Blodgett was used (KSV Nima, Bioloin Scientific, Stockholm, Sweden) and cleaned at least 10 times with water prior to the usage. After filling it with the water, the wafer was placed into the water, attached at a motorized clip which allowed to pull the it at a defined speed. 50 μl of a 2 mM solution of $F12H16$ solved in chloroform was spread on the water surface. After the evaporation of the solvent, the monolayer was compressed with a speed of $5\,\mathrm{cm\,min^{-1}}$ until a surface pressure of $\pi = 4\,\mathrm{mN\,m^{-1}}$ was reached. Then, the Si-wafer was extracted out of the water with a speed of

$1\,\mathrm{mm\,min^{-1}}$ allowing the formation of the monolayer on the Si-wafer. During that process, the surface pressure was kept constant at $\pi = 4\,\mathrm{mN\,m^{-1}}$ by closing the barrier further. After the deposition, the wafer was allowed to fully dry for at least 1 h at room temperature.

3.2.7. Atomic Force Microscopy

Atomic Force Microscopy was used to image $F12H16$ monolayers which were transferred on a Si-wafer. A NanoWizard 3 AFM from JPK Instruments (JPK Instruments AG, Berlin, Germany) was used. The images were recorded in tapping mode using a NCHV-A cantilever with tip radius $\approx 8\,\mathrm{nm}$, and spring constants $k \approx 20\,\mathrm{N\,m^{-1}}$ (Bruker Nano Inc., Billerica, USA).

4. Interfacial Shear Rheology of Semifluorinated Diblock Monolayers

So far, the structural ordering of semifluorinated $FnHm$ diblocks into nanodomains has been studied at the air/water interface using X-ray scattering techniques and AFM of solid-supported monolayers.[6,18] The dynamic behavior of $FnHm$ monolayers however was has not been thoroughly investigated yet. For example Klein et al. studied monolayers composed of $F12H12$, $F12H20$ and diblock copolymers in which the $F12$ and $H12$ segments are connected by a phenyl group using an ISR with a gliding magnetic needle under oscillating magnetic fields.[45] For all three molecules, they reported a predominantly elastic response. In case of $F12H12$, which self-assembles into circular domains, they observed a response typical for a 2D colloidal glass which they attributed to the interactions of the circular domains. The other two compounds behaved differently which was explained by the rather elongated and dendritic-like shaped domains.[45]

Indeed, the ordering of the $FnHm$ diblock molecules into circular surface micelles at the air/water interface is expected to determine the viscoelastic properties of the monolayers. The fluorocarbon segments of the $FnHm$ molecules point outwards, we can hence expect repulsive interactions between the surface micelles as it was shown that they do not coalesce, even at high surface pressures.[48]

The aim of this chapter is to study the interfacial shear properties of various $FnHm$ monolayers. After presenting π/A-isotherms and some preliminary experiments which are crucial for the following shear rheology measurements (Section 4.1), the frequency-dependent gelation of the monolayers is described (Section 4.2). This will be presented exemplarily for $F8H18$. Since it was reported that the semifluorinated alkane diblocks already self-assemble into the surface micelles at a surface pressure $\pi = 0\,\mathrm{mN\,m^{-1}}$,[30] it is interesting to study the mechanics of the monolayers in dependence of the surface pressure, too. In the next step, the hydrocarbon and fluorocarbon segment lengths were changed systematically in order to learn more about how the basic molecular parameters modulate the mechanics of the 2D film (Section 4.3).

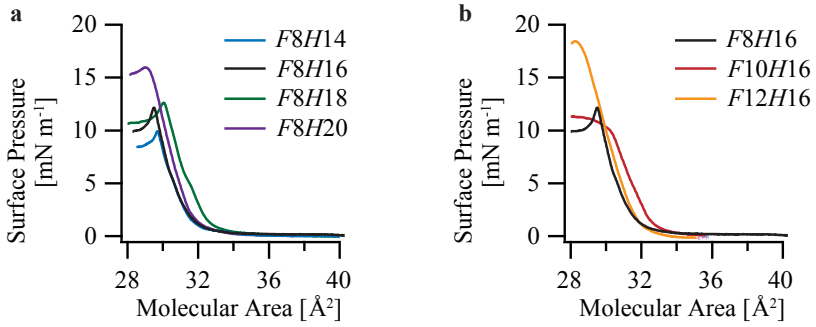

Figure 4.1.: **π/A-isotherms of $FnHm$ diblock monolayers.** a) π/A-isotherms of $F8Hm$ monolayers (m = 14, 16, 18, 20), b) π/A-isotherm of $FnH16$ monolayers ($n = 8, 10, 12$). The compression speed was $3.75\,\mathrm{cm^2\,min^{-1}}$ and the π/A-isotherms were recorded at $T = 20°\mathrm{C}$

The results presented in this chapter were published in Angewandte Chemie (2017).[1]

4.1. π/A-Isotherms and Preliminary Experiments

Figure 4.1 shows the π/A-isotherms of all $FnHm$ monolayers studied in this thesis. For clarity, they were separated into the $F8Hm$ monolayers (Figure 4.1a) and the $FnH16$ monolayers (Figure 4.1b). The π/A-isotherms were prepared as described in Section 3.2.1. They were fully reproducible and are comparable to the π/A-isotherms already published.[17,48]. All $FnHm$ monolayers exhibit the onset of the surface pressure increase at $\sim 33\,\mathrm{Å}^2$. The compressibilities do not alter much between the different diblocks and are in the range of $\kappa^{-1} = 6 - 8\,\mathrm{m\,N^{-1}}$ at $\pi = 5\,\mathrm{mN\,m^{-1}}$. The collapse pressure π_c on the other hand differs for the different $FnHm$ monolayers and increases with the molecular diblock length.

For the interfacial shear rheology measurements, it is crucial to perform the measurements in the linear response regime. Therefore, prior to studying the effect of frequency and surface pressure on the viscoelastic properties of the monolayer, test measurements at various frequencies and amplitudes were performed to find a combination which provides linear data for all $FnHm$ diblocks studied. Figure 4.2a exemplarily shows the elastic moduli G' and viscous moduli G'' recorded over time of

[1] Veschgini, M., Habe, T., *Mielke, S.*, Inoue, S., Liu, X., Krafft, M. P., & Tanaka, M. (2017). **Existence of Two-Dimensional Physical Gels even at Zero Surface Pressure at the Air/Water Interface: Rheology of Self-Assembled Domains of Small Molecules.** *Angewandte Chemie, 129*(41), 12777-12781.
I analyzed and structured the data, contributed to the interpretation of the results, wrote parts of the manuscript and performed additional, supporting experiments.

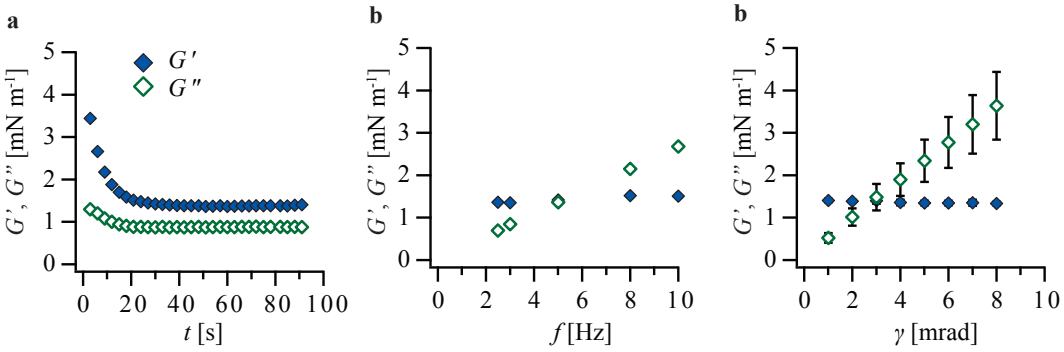

Figure 4.2.: **Elastic and viscous moduli G' and G'' of a $F8H16$ monolayer at the air/water interface.** a) For each condition of frequency, strain amplitude and surface pressure, the data were recorded over 90 s which was enough to confirm that the system reached thermodynamic equilibrium (G' and G'' const.). For the further analysis, the mean value and standard deviation of the last 10 data points was used. b) G' and G'' are displayed with respect to the frequency ($f = 2 - 10\,\mathrm{Hz}$) at a strain amplitude of $\gamma = 1.5\,\mathrm{mrad}$ and surface pressure of $7\,\mathrm{mN\,m^{-1}}$. c) G' and G'' plotted with respect to the strain amplitude ($\gamma = 1 - 8\,\mathrm{mrad}$) at the fixed frequency $f = 3\,\mathrm{Hz}$.

a $F8H16$ monolayer. For each measurement, the data were recorded over 90 s which was sufficient to reach thermodynamic equilibrium. The following data always represent the gliding mean of the last 10 data points and the respective standard deviation as error bar. In Figure 4.2b and c, frequency- and amplitude-sweep measurements at $\pi = 7\,\mathrm{mN\,m^{-1}}$ are shown confirming that the data were recorded in the linear response regime. The experimental procedure of the interfacial shear experiments is described in Section 3.2.2.

4.2. Formation of Two-Dimensional Gels

In order to study the effect of the surface pressure on the viscoelastic properties, interfacial shear rheology measurements were performed at a fixed oscillation frequency ($f = 3\,\mathrm{Hz}$) and oscillation amplitude ($\gamma = 1.5\,\mathrm{mrad}$). The results are shown in Figure 4.3 for a monolayer of $F8H18$. At this frequency and amplitude condition, the monolayer is predominantly elastic and behaves like a 2D gel ($G' > G''$) for all surface pressures measured. Both elastic and viscous moduli only slightly increased with π resulting in $G' = (1.5 \pm 0.2)\,\mathrm{mN\,m^{-1}}$ and $G'' = (1.0 \pm 0.2)\,\mathrm{mN\,m^{-1}}$ at $\pi = 10\,\mathrm{mN\,m^{-1}}$.

The formation of 2D gels has been reported for various types of monolayers at

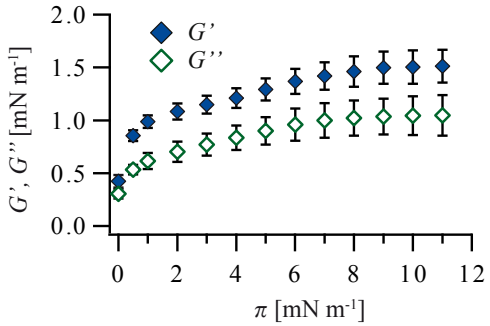

Figure 4.3.: **Elastic and viscous moduli G' and G'' of a $F8H18$ monolayer plotted with respect to the surface pressure.** The data was recorded at the frequency $f = 3\,\mathrm{Hz}$ and amplitude $\gamma = 1.5\,\mathrm{mrad}$. The value at $\pi = 0\,\mathrm{mN\,m^{-1}}$ corresponds to a surface area of $40\,\mathrm{Å}^2$.

the air/water interface. Here, we mostly have to distinguish between chemical and physical gels. Whereas chemical gels form by units that are linked by chemical bonds, physical gels are formed by units that are physically bonded and hence the gel formation is reversible.[43] Examples for 2D gels are monolayers of lipopolysaccarides (LPS) which form in the presence of Ca^{2+} [37] or monolayers of phospholipids coupled to poly(ethylene glycole) (PEG) chains.[80,81] Physical gels have so far only been reported for compressed monolayers at surface pressures $\pi > 0\,\mathrm{mN\,m^{-1}}$, e.g. for silicon and metal nanoparticles coated with surfactants.[33]

The $F8H18$ molecules at the air/water interface arrange in highly ordered, mesoscopic domains.[48] The molecular structure of the molecules excludes the possibility of the formation of chemical gels, in contrary, the strong dipole of the molecules is expected to lead to a repulsive interaction between the individual domains.[52] Indeed, the nanodomains do not coalesce even at high surface pressures.[17] The predominantly elastic response of the $F8H18$ monolayers can hence be attributed to the strong dipole repulsion between the surface micelles originating from the CF_3-termini and the $CF_2 - CH_2$ junctions. The principle viscoelastic behavior seems independent from the surface pressure which suggests that the $F8H18$ molecules already self-assemble into the stable nanodomains near $\pi \approx 0\,\mathrm{mN\,m^{-1}}$.

In order to shed light on the frequency-dependency of the gelation even at $\pi = 0\,\mathrm{mN\,m^{-1}}$, shear rheology measurements were performed at a fixed strain amplitude of $\gamma = 1.5\,\mathrm{mrad}$ in the frequency regime $2 - 10\,\mathrm{Hz}$ for various surfaces pressures from 0 to $8\,\mathrm{mN\,m^{-1}}$. Figure 4.4 shows the frequency-dependency of G' and G'' exemplarily at four different molecular areas/surface pressures. At $\pi = 0\,\mathrm{mN\,m}$, the power law

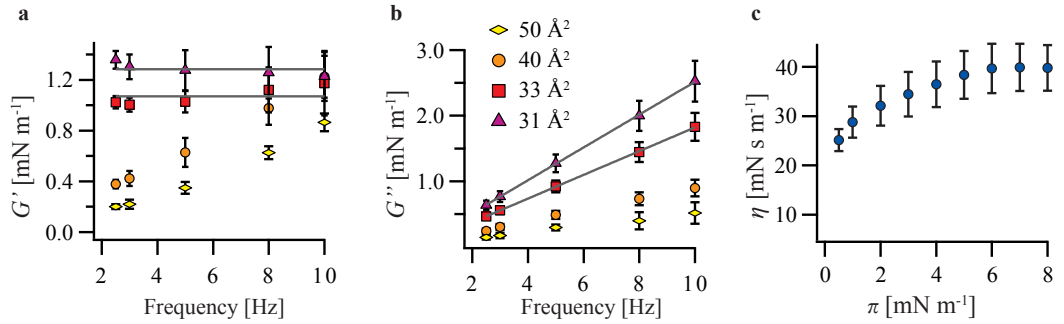

Figure 4.4.: **Kelvin-Voigt behavior of *F*8*H*18 monolayer.** a) Elastic modulus G' as a function of the frequency for four different molecular areas/surface pressures. ($50\,\text{Å}^2/0\,\text{mN}\,\text{m}^{-1}$, $40\,\text{Å}^2/0\,\text{mN}\,\text{m}^{-1}$, $33\,\text{Å}^2/1\,\text{mN}\,\text{m}^{-1}$, $31\,\text{Å}^2/8\,\text{mN}\,\text{m}^{-1}$). b) Viscous modulus G'' as a function of the frequency at the same surface pressure/molecular area conditions. The gray lines correspond to the fits of the Kelvin-Voigt model. c) Interfacial viscosity η derived from the slope of G'' vs. the frequency according to the Kelvin-Voigt model.

exponent for both G' and G'' is approximately 1 ($G' \propto f^1$, $G'' \propto f^1$). This is typical for soft glassy materials.[54,101] Interestingly, at surface pressures $\pi \geq 1\,\text{mN}\,\text{m}^{-1}$ (corresponding to molecular areas $A \geq 33\,\text{Å}^2$), G' and G'' follow a typical Kelvin-Voigt behavior which follows $G'(f) = g$ and $G''(f) = 2\pi\eta f$, with g being the spring constant and η the interfacial viscosity of the system (Section 2.3.3). The solid black lines in Figures 4.4a and b correspond to the linear fits of the Kelvin-Voigt model. The spring constant g depends on the surface pressure, at $\pi = 8\,\text{mN}\,\text{m}^{-1}$, $g = (1.28 \pm 0.02)\,\text{mN}\,\text{m}^{-1}$ was measured. The 2D viscosity η can be obtained from the slope of G'' with respect to the frequency (Figure 4.4b), the corresponding values are displayed in Figure 4.4c. Interestingly, η increases with the surface pressure until a final value of $\eta = (39.8 \pm 0.4)\,\mu\text{N}\,\text{s}\,\text{m}^{-1}$ is reached at $8\,\text{mN}\,\text{m}^{-1}$. Compared to other systems, this value of the interfacial viscoisty is very low.[39,103,106,107] These monolayers however consist of surfactants possessing large hydrophilic headgroups (e.g. lipids), which are partially immersed into the water subphase. In case of the completely hydrophobic semifluorinated alkanes, we can expect that the contact area between the *FnHm* diblock molecules and the water is minimal. The little energy loss during the rheological measurements can therefore be attributed to the low friction between the *F*8*H*18 monolayer and the water.

For $\pi > 0\,\text{mN}\,\text{m}^{-1}$ the data show a Kelvin-Voigt like behavior of the *F*8*H*18 monolayer, which is characteristic for solid-like materials with a predominantly elastic response. However, a closer look at the data shows that at higher frequencies $f >$

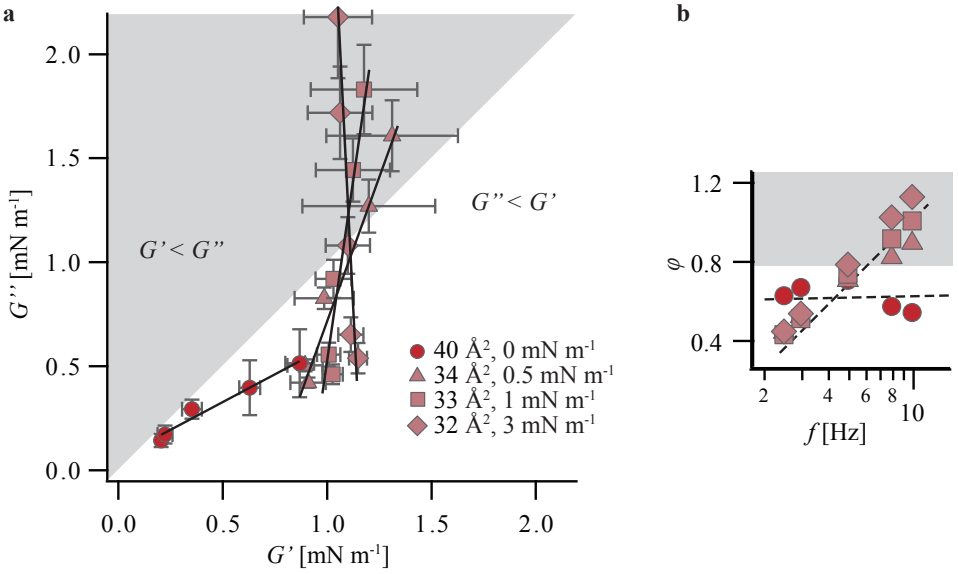

Figure 4.5.: **Frequency-dependent gelation of a *F*8*H*18 monolayer.** a) Viscous modulus G'' vs. elastic modulus G' of a $F8H18$ monolayer measured at different surface pressures in the frequency range of $2-10\,\mathrm{Hz}$ and amplitude $1.5\,\mathrm{mrad}$. b) Phase shift φ of the same data with respect to the frequency. The shaded regions display the predominantly viscous region ($G'' > G'$, $\varphi > \pi/2$).

6 Hz, the monolayer looses the gel-like behavior as $G' < G''$. Figure 4.5a shows the same data as in Figure 4.4 by displaying the relationship between G' and G''. Figure 4.4b shows the respective phase separation φ between stress and strain as a function of the frequency. The shaded regions indicate the predominantly viscous region, where $G'' > G'$ and hence $\varphi = \tan^{-1}(G''/G') > \pi/2$. At $\pi = 0\,\mathrm{mN\,m^{-1}}$, the monolayer behaves predominantly elastic in the whole frequency regime measured ($f = 2-10\,\mathrm{Hz}$) and the phase shift remains more or less constant at $\varphi \approx 0.6$. Already a slight compression of the monolayer to $\pi = 0.5\,\mathrm{mN\,m^{-1}}$ leads to a drastic change in its behavior. At low frequencies, the monolayer is still predominantly elastic. However φ increases with frequency and at the critical frequency of $f_c = 6\,\mathrm{Hz}$, φ exceeds $\pi/2$. For the higher surface pressures, the same tendency was observed.

In summary, as soon as the monolayer is compressed to $\pi > 0\,\mathrm{mN\,m^{-1}}$, it changes its behavior slightly and looses its predominantly elastic character at the critical frequency $f_c = 6\,\mathrm{Hz}$ (for $\gamma = 1.5\,\mathrm{mrad}$). The results further clearly indicate that the $F8H18$ nanodomains form a 2D physical gel already at $0\,\mathrm{mN\,m^{-1}}$. Such a behavior has not been reported for other organic compounds so far. In most cases, self-assembled organic molecules undergo gelation only at high surfaces pressures.[80,81,97]

The behavior observed for the $F8H18$ nanodomains is similar to that of hard particles.[16,21,70] These unique rheological properties can hence be attributed to the strong dipole repulsions between the domains.

4.3. Influence of Hydrocarbon and Fluorocarbon Segment Length

To elucidate the influence of the fluorocarbon and hydrocarbon segment length on the viscoelastic properties, interfacial shear rheology measurements on monolayers formed by $F8H14$, $F8H16$, $F8H20$, $F10H16$ and $F12H16$ were performed. In order to compare the systems, all measurements were performed at the frequency $f = 3\,\mathrm{Hz}$ and amplitude $\gamma = 1.5\,\mathrm{mrad}$. Figure 4.6 displays the values for G' and G'' recorded at the surface pressure of $\pi = 5\,\mathrm{mN\,m^{-1}}$ with respect to the hydrocarbon segment length m and the fluorocarbon segment length n. The whole data set is shown in Figure A.1. G'' monotonically increases with the hydrocarbon segment length of $F8Hm$ from $G''_{F8H14} = (0.4 \pm 0.1)\,\mathrm{mN\,m^{-1}}$ to $G''_{F8H20} = (2.7 \pm 1.1)\,\mathrm{mN\,m^{-1}}$. G' on the other hand remains almost constant for $m = 14$, 16 and 18 at $G' \approx 1.4\,\mathrm{mN\,m^{-1}}$ and increased significantly when further increasing m to $G'_{F8H20} = (5.1 \pm 1.9)\,\mathrm{mN\,m^{-1}}$.

Increasing the fluorocarbon segment length from $F8H16$ to $F10H16$ does not significantly change G' and G'' ($G' \approx 1.4\,\mathrm{mN\,m^{-1}}$, $G'' \approx 0.4\,\mathrm{mN\,m^{-1}}$). However increasing the fluorocarbon segment length further to $F12H16$ leads to a drastic increase of both G' and G'' by one order of magnitude ($G'_{F12H16} = (25.2 \pm 5.9)\,\mathrm{mN\,m^{-1}}$, $G''_{F12H16} = (8.3 \pm 0.4)\,\mathrm{mN\,m^{-1}}$). It also has to be noted that G' of $F12H16$ did not reach full equilibrium even after 90 s (Figure A.2a). However, the tendency was confirmed by measuring the monolayer at $f = 5\,\mathrm{Hz}$ and $\gamma = 3\,\mathrm{mrad}$ where similar high values for G' and G'' were measured and the monolayer reached thermal equilibrium (Figure A.2b).

What is the origin for this dependency of the viscoelastic properties on the length of the $FnHm$ molecules? As elaborated in the previous section, the predominantly elastic response of the $FnHm$ monolayers can be attributed to the strong repulsion between the surface micelles. The origin of this repulsion lies in the dipole moments. The dipole moment of one surface micelle is determined by two factors, first the domain size and second, the alignment of the molecular dipoles within the domain. The GISAXS data presented in Section 6.2 indeed show that increasing the hydrocarbon or fluorocarbon segment length leads to monotonic increase of the diameter of the surface micelles (Section 6.2). Due to the increased van der Waals forces, longer

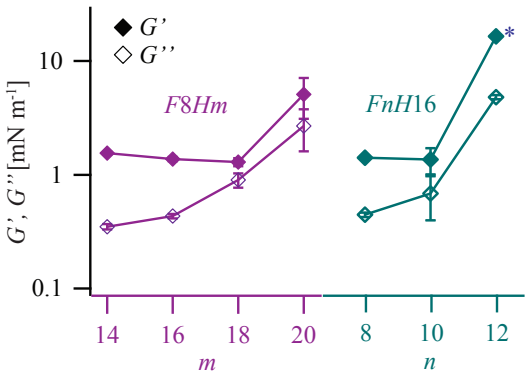

Figure 4.6.: **Elastic and viscous modulus G' and G'' of $FnHm$ monolayers plotted as a function of the hydrocarbon segment length m and the fluorocarbon segment length n.** The data were recorded at $\pi = 5\,\mathrm{mN\,m^{-1}}$, $f = 3\,\mathrm{Hz}$ and $\gamma = 1.5\,\mathrm{mrad}$. In case of the $F12H16$ monolayer, G' still exhibited a continuous increase after 90 s.

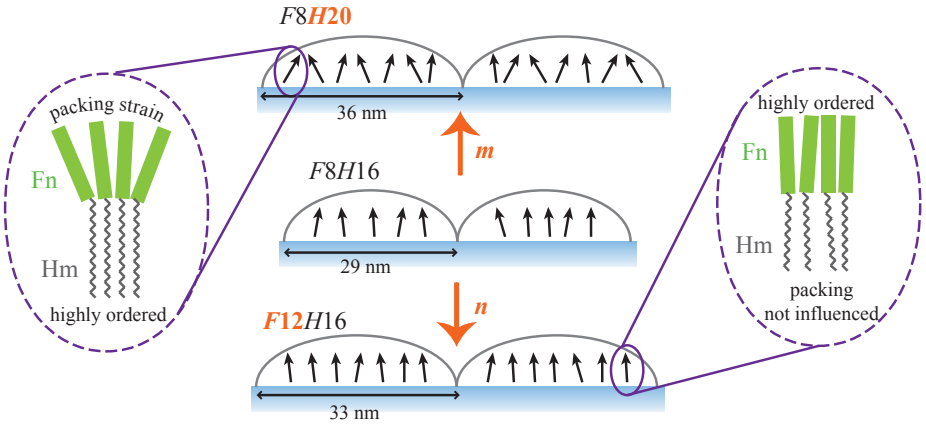

Figure 4.7.: **Schematic model describing the impact of elongating the hydrocarbon (top) and fluorocarbon (bottom) segment length on the dipole moments of $FnHm$ surface micelles.** Increasing the hydrocarbon segment length m leads to larger domain sizes and the ordering of the hydrocarbon chains is increased which results in a packing strain of the fluorocarbon chains. Therefore the molecular dipoles are poorly aligned. An increase of the fluorocarbon segment length n leads to a increased domains with well aligned dipoles.

hydrocarbon chains show a higher lateral order. This effect was reported widely for self-assembled monolayers.[13,38] Since the fluorocarbon chains have higher cross-sectional areas than the hydrocarbon chains, an increase of the lateral order of the hydrocarbon chains leads to a packing strain of the bulkier fluorocarbon chains. This is schematically illustrated in Figure 4.7. The fluorocarbon chains are hence more disordered. Therefore, the molecular dipoles are less aligned.

Elongating the fluorocarbon segments at a fixed hydrocarbon segment length however does not disturb the ordering of the hydrocarbon chains. Indeed, increased van der Waals forces between the fluorocarbon segments may even increase the ordering effect. However due to the better ordering of the fluorocarbon segments, the net dipole moment is increased which can explain the strong increase in G' by a factor of ~ 20. In contrast, the elongation of the hydrocarbon segment only slightly increases the dipole moment and hence G' is increased to a lower extend.

5. Dilational Rheology of Semifluorinated Alkane Monolayers

In rheology, one has to distinguish between shear and dilational effects. Therefore, in order to extend the study on the viscoelastic properties of monolayers composed of semifluorinated alkanes at the air/water interface, interfacial dilational rheology experiments were performed using a Langmuir film balance with two oscillating barriers that allow a sinusoidal change of the surface area. Studying both complementary methods, interfacial shear and dilational rheology, provides a broad, valuable overview about the mechanics of the monolayers under different stress/strain conditions.

So far, the dilational viscoelastic properties of Langmuir monolayers made of semifluorinated alkane have not been studied. Kovalenko et al. investigated the dilational viscoelasticity of Gibbs monolayers of $F8H2$Phos and $F10H2$Phos, short chain semifluorinated alkanes that possess a phosphate group at the hydrocarbon termini.[47] They observed exceptional high values for the elastic moduli $E' \approx 900\,\mathrm{mN\,m^{-1}}$ at surface pressures around $\sim 25\,\mathrm{mN\,m^{-1}}$ using a bubble tensiometer.[47] However, they did not study the influence of oscillation frequency and amplitude on the viscoelastic properties. From their results, Kovalenko et al. suggested the formation of the fluorinated molecules into surface domains which has not been confirmed, yet.

The previous interfacial rheology studies already suggest that the ordering of the $FnHm$ molecules into surface micelles strongly influences the viscoelastic behavior of the monolayers at the air/water interface. There are only few studies investigating the dilational viscoelasticity of monolayers that show ordered structures. For example Li Destri et al. investigated monolayers composed of various polystyrene-b-poly(methyl methacrylate) (PS-b-PMMA) copolymers.[20] They observed that the copolymers forming rather circular domains showed a predominantly elastic behavior whereas an entanglement of the copolymers into wormlike micelles lead to an increase of the viscous contribution.[20] This suggests that a circular, well ordered shape of self-assembled structures leads to a rather elastic behavior. One can therefore assume that monolayers of semifluorinated alkanes that arrange in well-ordered

circular shaped nanodomains respond in a predominantly elastic way to dilational stress.

This chapter first focuses on the dilational viscoelastic properties of semifluorinated di($FnHm$) tetrablock monolayers (Section 5.1). In fact, investigating these monolayers by interfacial shear rheology was not possible as they were too stiff, exceeding the sensitivity of the rheometer (Figure A.3). In Section 5.2 the equivalent measurements performed for $FnHm$ diblock monolayers are presented.

The results presented in Section 5.1 were published in Langmuir (2018).[1]

5.1. Dilational Viscoelasticity of Semifluorinated Tetrablocks

As a first step, π/A-isotherms were recorded for the three tetrablock molecules di($F10Hm$), $m = 16, 18, 20$ (Figure 5.1a). The experimental procedure is described in Section 3.2.1. All three monolayers showed extremely low compressibilities in the range of $\kappa^{-1} \approx 7\,\mathrm{m\,N^{-1}}$ at $\pi = 5\,\mathrm{mN\,m^{-1}}$. The onset of the increase of the surface pressure was at $A \approx 58\,\mathrm{\AA}^2$, independent from the length of the tetrablock molecule. The collapse pressure was in the range of $\pi_c = 16 - 24\,\mathrm{mN\,m^{-1}}$, increasing with hydrocarbon segment length. This confirms the results published previously by de Gracia Lux et al.[18]

The solid gray line in the isotherms in the Figure 5.1a marks $\pi_0 = 5\,\mathrm{mN\,m^{-1}}$. This is the surface pressure chosen for the dilational rheology experiments.[2] The detailed experimental procedure is described in Section 3.2.3. Figure 5.1b shows a typical stress strain signal of a di($F10H16$) monolayer recorded at $f = 100\,\mathrm{mHz}$, $u_0 = 0.01$ and $\pi = 5\,\mathrm{mN\,m^{-1}}$.[3] The applied amplitude corresponds to a change of the molecular area of $0.6 - 0.8\,\mathrm{\AA}^2$. It can therefore be assumed that the global spatial distribution of the di($FnHm$) nanodomains is not disturbed by the area oscillation as the amplitude is 4 orders of magnitude smaller than the area of one nanodomain ($D \approx 40\,\mathrm{nm}$).

[1] *Mielke, S.*, Habe, T., Veschgini, M., Liu, X., Yoshikawa, K., Krafft, M. P., & Tanaka, M. (2018). **Emergence of Strong Nonlinear Viscoelastic Response of Semifluorinated Alkane Monolayers.** Langmuir, 34(7), 2489-2496.
I performed all experiments, analyzed and interpreted the data and wrote the major part of the manuscript.

[2] $\pi_0 = 5\,\mathrm{mN\,m^{-1}}$ was chosen since it could be used for the $FnHm$ diblocks as well which have a lower collapse pressure and therefore it is not possible to measure the dilational viscoelasticity at higher π_0.

[3] The chosen frequency/amplitude regime corresponds to strain velocities which are in the same order of magnitude than that used for the ISR measurements.

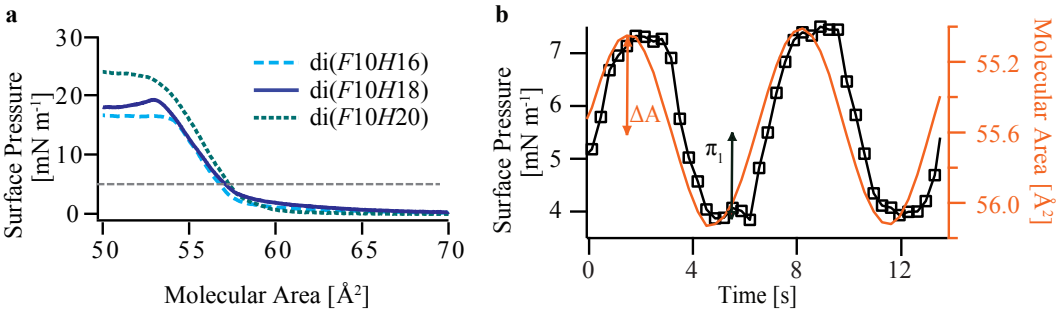

Figure 5.1.: **π/A-isotherms and stress strain signal from dilational rheology of di($F10Hm$) tetrablock monolayers.** a) π/A-isotherms recorded at a speed of 3.75 cm^2 min^{-1} and $T = 20°$C. b) Response of the surface pressure $\pi(t)$ over time at the respective applied change of the surface area (in red). The amplitude of the area change ΔA and the amplitude of the surface pressure change π_1 are marked in the figure. There is a phase separation φ between the area and the surface pressure oscillation.

The shape of the oscillation of the surface pressure already suggests that the response of the di($F10H16$) monolayer to the dilational stress is nonlinear. Therefore, as introduced in Section 2.3.5, the data were fitted to a Fourier series expansion

$$\pi(t) = \pi_0 + \sum_{k=1}^{n} \pi_k \sin(k\omega t + \varphi_{\pi_k}) \tag{5.1}$$

where $\omega = 2\pi f$ is the angular frequency , π_0 is the starting surface pressure ($\pi_0 \approx 5\,\mathrm{mN\,m^{-1}}$), π_k is the amplitude of the k-th Fourier mode and φ_{π_k} the corresponding phase shift.

In a first step, the focus is set on the contribution of the first mode to the viscoelastic properties. Then, the contributions of the higher modes (nonlinear part) are further examined and discussed.

5.1.1. First Mode Analysis

Figure 5.2a shows the phase separation $\varphi_1 = \tan^{-1}\left(\frac{E_1''}{E_1'}\right)$ between stress and strain of the first Fourier mode for all three tetrablock molecules. In the measured frequency regime, the phase shift is below $\pi/2$, which indicates a predominantly elastic response. φ_1 monotonically increases with frequency. As $E'' \propto \sin\varphi$ (Equation 2.40) and φ is small, the monolayers show an increase of the viscous contribution at the higher frequencies. This is especially prominent for di($F10H20$) which shows compared to the other two tetrablock monolayers the highest phase separation of $\varphi_1 = 0.6$ at

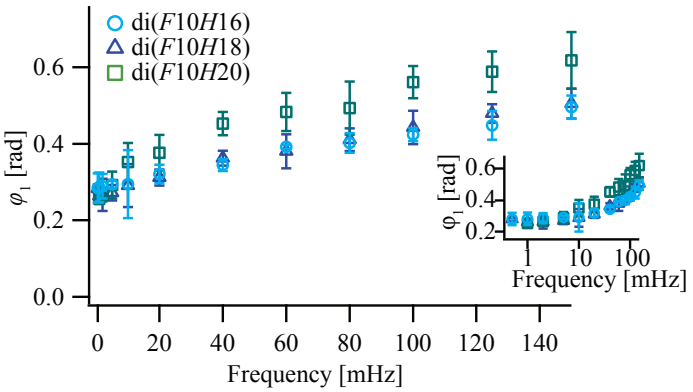

Figure 5.2.: **Phase shift φ_1 between stress and strain plotted as a function of frequency for the di($F10Hm$) monolayers.** The inset shows the data in a semilogarithmic scale. Below $f = 10\,\mathrm{mHz}$ the phase separation is constant at $\varphi_1 \approx 0.28$.

	di($F10H16$)	di($F10H18$)	di($F10H20$)
g [$\mathrm{mN\,m^{-1}}$]	164 ± 4	163 ± 1	142 ± 10
η [$\mu\mathrm{N\,s\,m^{-1}}$]	36 ± 6	54 ± 5	57 ± 17

Table 5.1.: Spring constant g and interfacial viscosity η of di($F10Hm$) monolayers. The values were obtained from fitting the Kelvin-Voigt model to the data shown in Figure 5.3.

$f = 150\,\mathrm{mHz}$. At low frequencies, φ_1 approaches $\varphi_1 \approx 0.28$, which is the intrinsic phase separation φ_{exp} resulting from the experimental setup. Indeed, here, φ_{exp} slightly depends on the amount of molecules spread on the available surface area of the Langmuir trough (Figure A.4). Therefore, the same amount of sample solution ($40\,\mu\mathrm{l}$ of $1\,\mathrm{mM}$ di($F10Hm$) solution) was used throughout the study.

Figures 5.3a-c show the elastic and viscous moduli E_1' and E_1'' for all three tetrablock molecules calculated from the first mode according to Equation 2.39 and 2.40. The elastic and viscous moduli confirm the finding of a predominantly elastic response as $E_1' > E_1''$ in the whole frequency regime. While the elastic modulus E_1' is independent of the frequency, the viscous modulus E_1'' increases linearly with the frequency. This is typical for a Kelvin-Voigt material and therefore, the Kelvin-Voigt model (Section 2.3.3) was fitted to the data and is indicated by the solid lines in Figure 5.3. This allows the calculation of the spring constant g and the interfacial viscosity η which are given in Table 5.1 for the respective tetrablocks. The determination of g and η helps comparing the three systems independent of the applied frequency. Only slight differences between the three di($F10Hm$) monolayers were

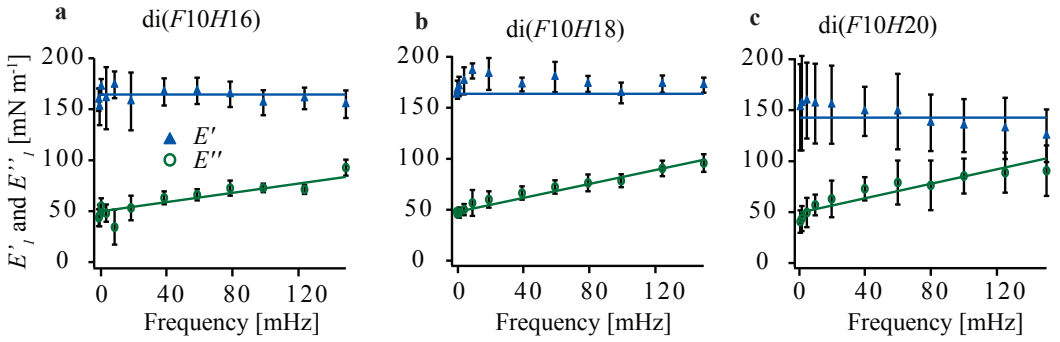

Figure 5.3.: **Interfacial Dilational Rheology of di($F10Hm$) ($m = 16, 18, 20$) monolayers, analyzed from the first Fourier mode.** Dilational elastic modulus E_1' and viscous modulus E_1'' for di($F10H16$) (a), di($F10H18$) (b) and di($F10H20$) (c) measured in the frequency range of $1 - 150\,\mathrm{mHz}$. The solid lines correspond to the fitting results of the Kelvin-Voigt model. The values of the spring constant g and the interfacial viscosity η obtained from the fits are given Table 5.1.

observed: The spring constant of the di($F10H20$) monolayers was reduced compared to the other two monolayers by $\sim 10\,\%$. The interfacial viscosity η was in the range of $\eta = 30 - 70\,\mu\mathrm{N\,s\,m^{-1}}$ for all three monolayers.

In order to investigate the influence of the surface pressure, the measurements were also performed at $\pi_0 = 10\,\mathrm{mN\,m^{-1}}$ for di($F10H16$), which is shown in Figure 5.4. We observed the same tendency of the frequency-dependency of E_1', E_1'' and φ_1 as for the measurements at $\pi_0 = 5\,\mathrm{mN\,m^{-1}}$. Fitting the data to the Kelvin-Voigt model resulted in an increased spring constant of $g = (184 \pm 1)\,\mathrm{mN\,m^{-1}}$ compared to the situation at $\pi_0 = 5\,\mathrm{mN\,m^{-1}}$ ($g_{\mathrm{di}(F10H16),5\,\mathrm{mN\,m^{-1}}} = (164 \pm 4)\,\mathrm{mN\,m^{-1}}$), whereas the interfacial viscosity was not affected by the increased surface pressure which is in line with th higher spring constant measured at $\pi_0 = 10\,\mathrm{mN\,m^{-1}}$.

The spring constants and elastic moduli $E_1' > 120\,\mathrm{mN\,m^{-1}}$ of the di($F10Hm$) monolayers are very high compared to other systems of Langmuir monolayers. Similar high values were reported by López-Montero et al. from monolayers formed by egg ceramides, however only when they were compressed to high surface pressures $\pi \geq 15\,\mathrm{mN\,m^{-1}}$.[61] Monolayers formed from DPPC lipids for example have spring constants in the region of $g_{DPPC} \approx 30\,\mathrm{mN\,m^{-1}}$, four times lower than the values measured for the semifluorinated alkanes monolayers.[106]

The high spring constants can be attributed to the low compressibility of the di($F10Hm$) monolayers. Indeed, at $\pi = 10\,\mathrm{mN\,m^{-1}}$, the monolayers showed even lower values of the compressibility compared to $\pi = 5\,\mathrm{mN\,m^{-1}}$, for di($F10H16$),

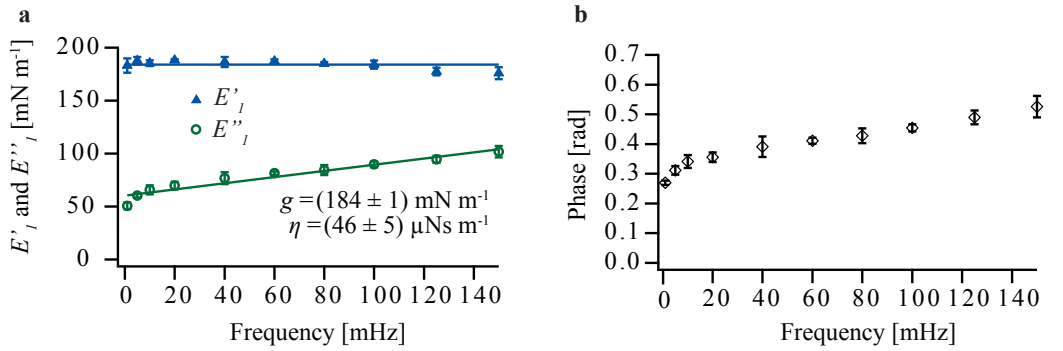

Figure 5.4.: **Dilational Rheology of di($F10H16$) at $\pi_0 = 10\,\mathrm{mN\,m^{-1}}$.** (a) Dilational elastic modulus E_1' and viscous modulus E_1'' with respect to the frequency, the lines correspond to the fit of the Kelvin-Voigt model. (b) Phase separation φ_1 between stress and strain with respect to the frequency.

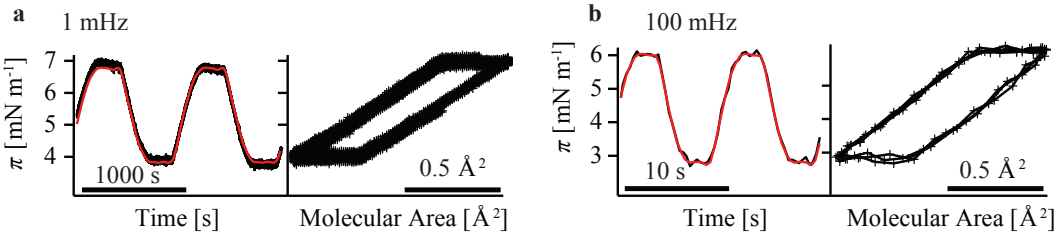

Figure 5.5.: **Response of the surface pressure of a di($F10H16$) monolayer.** π is plotted as a function of time and molecular area (Lissajou curve) for $f = 1\,\mathrm{mHz}$ (a) and $f = 100\,\mathrm{mHz}$ (b).

$\kappa^{-1}_{5\,\mathrm{mN\,m^{-1}}} \approx 6.8\,\mathrm{mN\,m^{-1}}$ and $\kappa^{-1}_{10\,\mathrm{mN\,m^{-1}}} \approx 4.3\,\mathrm{mN\,m^{-1}}$ were measured. The fact that $E_1' > E_1''$ shows that the tetrablock molecules form a 2D gel on water as already observed for the semifluorinated diblocks in shear rheology experiments (Chapter 4). As elaborated for the diblocks, this suggests that the strong elasticity results from the repulsive interactions between the surface micelles.

The high elasticity of the system goes in line with an extremely low interfacial viscosity $\eta < 0.06\,\mathrm{mN\,m^{-1}}$. This is very low compared to other Langmuir monolayer systems.[39,103,106,107] This low interfacial viscosity can be attributed to 1) the low friction between the nanodomains and the water subphase due to the strong hydrophobic nature of the di($F10Hm$) molecules and 2) the low frictional losses between the domains.

5.1.2. Nonlinear Analysis

So far, only the first mode of the Fourier series expansion was studied. However, as visible in Figure 5.5, the response of the surface pressure to oscillatory strain clearly deviates from a perfect sinusoidal shape and is nonlinear. Here, the surface pressure response is exemplarily shown for a di($F10H16$) monolayer with respect to the time and with respect to the molecular area (Lissajou curve) for $f = 1\,\mathrm{mHz}$ and $f = 100\,\mathrm{mHz}$. The principle behavior was the same for the other frequencies and the other two tetrablocks. The flat portions and kinks in the Lissajou curve clearly show the deviation from a purely linear signal which would have an elliptical shape. The red lines in the figure show the fits to a Fourier Series expansion up to the fifth mode.

In order to analyze this nonlinearity quantitatively, different approaches were used. Figure 5.6a shows the Fourier spectrum of a di($F10H16$) monolayer at $f = 100\,\mathrm{mHz}$. Clearly, only signals at odd modes were observed. Interestingly, also only the real part of the Fourier spectrum shows features, whereas in the imaginary part only the first mode is visible. The same trend was observed for the other frequencies. Figure 5.6b shows the amplitude of the higher modes normalized to the first mode with respect to the frequency. Obviously, there is no effect of the frequency on the nonlinear part. The third mode has the highest value with $\pi_3/\pi_1 \approx 0.12$ followed by the fifth mode ($\pi_5/\pi_1 \approx 0.03$), whereas the even modes and the 7th mode are close to the noise range of the experimental setup ($\sim 2\,\mathrm{mN\,m^{-1}}$) which is indicated by a gray dashed line in Figure 5.6b. The same tendency was observed for di($F10H18$) and di($F10H20$) (Figure A.5). Fitting the surface pressure data to a Fourier series expansion up to 5th mode was found to be sufficient to obtain good fitting results; including higher modes did not improve the quality of the fit. In order to exclude that the nonlinearity raises from the input signal, the oscillatory data of the change of the area $A(t)$ were studied by Fourier analysis as well, finding no nonlinear contribution.

In order to quantify the degree of nonlinearity, the THD was calculated (cf. Section 2.3.5). As the nonlinearity was found to be independent of the frequency, The THDs averaged over the measured frequency regime are given in Table 5.2 with respect to the hydrocarbon segment length m. No distinct difference of the THD between the three tetrablock monolayers was observed, $\mathrm{THD}_{\mathrm{di}(F10Hm)} \approx 12\,\%$. The data at $\pi_0 = 10\,\mathrm{mN\,m^{-1}}$ showed similar nonlinear features with $\mathrm{THD} = (13.0 \pm 0.7)\,\%$. As the nonlinearity is usually strongly affected by the strain amplitude, additional dilational rheology measurements were performed at the amplitudes $u_0 = 0.005$ and $u_0 = 0.02$ for di($F10H16$) at $f = 10\,\mathrm{mHz}$ (Figure A.6). Interestingly, the THD

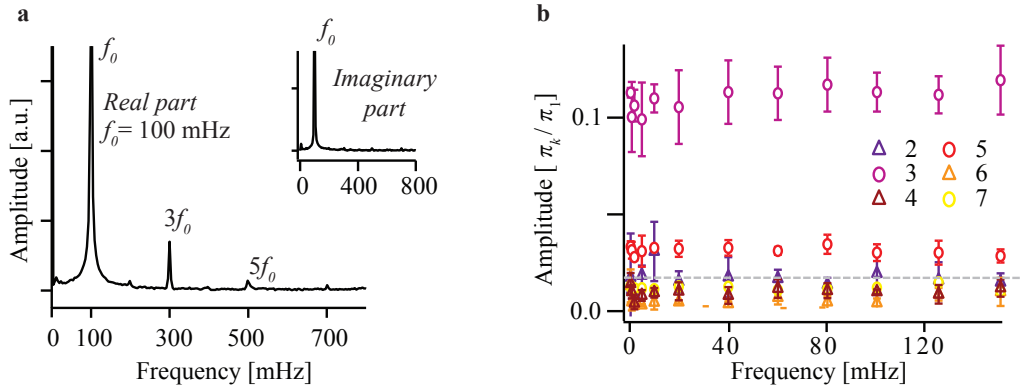

Figure 5.6.: **Analysis of the nonlinear dilational viscoelastic signal of di($F10Hm$) monolayers.** (a) Real part of the Fourier-transformed response function of a di($F10H16$) monolayer at $f = 100\,\mathrm{mHz}$. The inset shows the imaginary part of the Fourier spectrum. (b) Fractions of the higher Fourier modes (2 - 7) compared to the first mode, π_k/π_1 of a di($F10H16$) monolayer with respect to the frequency. The gray line shows the noise level of the experiments.

	di($F10H16$)	di($F10H18$)	di($F10H20$)
THD	$(12.5 \pm 0.9)\,\%$	$(11.3 \pm 0.8)\,\%$	$(11.6 \pm 0.8)\,\%$

Table 5.2.: THD averaged over the frequency for the di($F10Hm$) monolayers, $m = 16$, 18 and 20

was only barely affected by the amplitude. However, an emergence of the second mode occurred at $u_0 = 0.02$ suggesting the increased effect of friction. Due to the experimental limitations and the low compressibility of the monolayers, it was not possible to perform measurements at other strain amplitudes.

Nonlinear dilational stress responses have often been reported.[32,39,60,61,68,83,105] Mostly, they were observed in Gibbs monolayers and the rise of nonlinearity could be explained by a change in the surface concentration which can be understood by the model of van den Tempel and Lucassen.[62,83] This scenario can be excluded in this case due to the strong hydrophobicity of the semifluorinated molecules. Other possible explanations reported so far are the lateral diffusion of the surfactants[4] or changes in the microstructure.[39,64,92] Interestingly, the nonlinearity reported for other systems of Langmuir monolayers occurred mostly at higher surface pressures ($\pi \geq 15\,\mathrm{mN\,m^{-1}}$) and especially at high strain amplitudes ($u_0 \geq 5\,\%$).

Compared to other systems, the tetrablock monolayers hence exhibit two distinct features measured by interfacial dilational rheology: A strong elastic response combined with a high nonlinearity, even at low strain amplitudes. As elaborated in Section 2.3.5, the rise of mostly odd modes can be explained by a predominantly

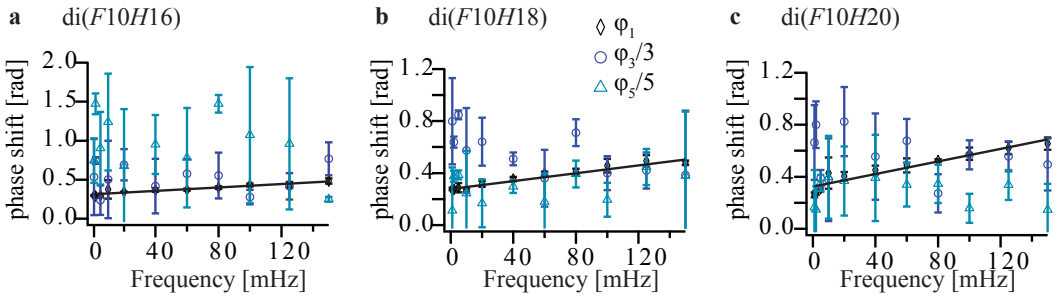

Figure 5.7.: **Phase shift between stress and strain for mode 1, 3 and 5 in dependence of the frequency for di($F10H16$) (a), di($F10H18$) (b) and di($F10H20$) (c) monolayers.** φ_1 increases linearly with the frequency, the respecting fit is included. φ_3 and φ_5 however do not show any frequency-dependency.

nonlinear elastic component as this should be odd under reflection due to mirror symmetry. As only odd modes appear in the Fourier series expansion, one can hypothesize that the nonlinearity of the tetrablock monolayers results from the elastic part of the system. The imaginary part of the Fourier spectrum does not show any features at higher modes which supports this hypothesis as the imaginary part represents the viscosity of the system.

To further analyze this hypothesis, the phase separations of the higher Fourier modes φ_3 and φ_5 were studied. Figure 5.7 shows the phase shifts with respect to the frequency for all three tetrablock molecules. As already shown before in Figure 5.2, φ_1 increases linearly with the frequency. Since $E_1'' \propto \sin\varphi_1$ and $E'' = \eta 2\pi f$ in the framework of the Kelvin-Voigt model, for small phase shifts, it holds

$$\varphi_1 \propto \eta 2\pi f. \tag{5.2}$$

Hence, the slope of the phase shift represents the interfacial viscosity η. As shown in Figure 5.7, the higher mode phase shifts φ_3 and φ_5 do not show any frequency dependency. It can therefore be concluded, that the viscosity of the system is mostly represented by the first mode phase shift φ_1. This is another hint that the nonlinearity lies in the elastic part of the system and not the viscous part.

This information can be used to extend the linear Kelvin-Voigt model by and additional, nonlinear elastic term,

$$\pi(t) \propto g + g'\epsilon^3 + \eta\frac{\partial\epsilon}{\partial t}. \tag{5.3}$$

This extended Kelvin-Voigt model describes the data well, the higher mode spring constant is $g' \approx 0.12g$.

A possible explanation of the rise of nonlinearity may be the occurrence of a first order phase transition. The Lissajou curves (Figure 5.5) show flat panels ($\kappa^{-1} \rightarrow \infty$) which are commonly seen in isothermal compressions of lipid monolayers that undergo a first order phase transition (see Section 2.1). In the framework of Landau theory, we can describe phase transitions of a system having the order parameter q close to the transition point by the free energy[34,57]

$$F(q,t) = \frac{\alpha}{2}q^2 + \frac{\beta}{4}q^4 \tag{5.4}$$

with α and β being proportionality factors. If a time-dependent, external force $h(t)$ is acting on the system, the free energy needs to be extended to[34,57]

$$F(q,t) = \frac{\alpha}{2}q^2 + \frac{\beta}{4}q^4 + h(t)q. \tag{5.5}$$

This only holds for a time-independent order parameter. In the framework of Landau theory, if the order parameter q is time-dependent and we observe relaxation processes, one can then assume that it behaves as[34,57]

$$\frac{\partial q(t)}{\partial t} \propto -\frac{\partial F(q,t)}{\partial q}. \tag{5.6}$$

Using the free energy in Equation 5.5, one obtains an equation for the relaxation of q,

$$\frac{\partial q(t)}{\partial t} \propto \alpha q + \beta q^3 + h(t). \tag{5.7}$$

This behavior can be transferred to the monolayer of semifluorinated alkanes where we can think of the time-dependent area change (density) $u(t)$ to be equivalent to the order parameter $q(t)$, and the external force $h(t)$ to be equivalent to the surface pressure change (stress) $\pi(t)$. It then holds

$$\pi(t) \propto \alpha' u(t) + \beta' u(t)^3 + \eta' \frac{\partial u(t)}{\partial t} \tag{5.8}$$

which represents directly the extended nonlinear Kelvin-Voigt model presented above (Equation 5.3) with α' and β' corresponding to the spring constants. Therefore, one can claim that the nonlinearity as observed for the rheology of semifluorinated alkane monolayers with an increased third mode in the elastic term can be explained by a first order phase transition. This phase transition is obviously only visible for very

small compression speeds such as they were applied with the small strain amplitudes during the dilational oscillations.

5.2. Dilational Linear and Nonlinear Viscoelasticity of Semifluorinated Diblocks

Interfacial dilational rheology measurements were performed on monolayers composed of semifluorinated $FnHm$ diblock monolayers as well. The molecules studied are: $F8H16$, $F8H18$, $F8H20$, $F10H16$, $F12H16$. In a first step, the dilational viscoelasticity of $F10H16$ monolayers is presented in detail in order to compare it to the tetrablock counterpart di($F10H16$) (Section 5.1). In the next step, the influence of hydrocarbon and fluorocarbon segment length on the dilational viscoelastic properties is studied (Section 5.2.1).

5.2.1. Dilational Viscoelasticity of *F10H16*

Figure 5.8 shows the surface pressure response $\pi(t)$ of a $F10H16$ monolayer measured under oscillatory change of the surface area with respect to the the time (a) and the area (b) at a strain frequency of $f = 100\,\mathrm{mHz}$ and a strain amplitude of $u_0 = 0.01$. The global shape of the response function is similar to that measured for the tetrablock molecules (Figure 5.1) and also shows nonlinear features which are indicated by the flat portions in Figure 5.8a and the deviation from the elliptical shape of the Lissajou curve in Figure 5.8b. Analogous to the previous procedure, the surface pressure response was fitted to a Fourier series expansion up to the 5th mode. In a first step, the first mode is analyzed in the framework of linear dilational rheology. The nonlinear contribution is analyzed in a next step.

Figure 5.9a shows the phase separation φ_1 between stress and strain of the first Fourier mode as function of the frequency for both, $F10H16$ diblock and di($F10H16$) tetrablock monolayers. φ_1 is slightly smaller for the diblock system compared to the tetrablock system. However, in both cases $\varphi_1 < \pi/2$ indicating that the monolayers behave predominantly elastic in the measured frequency regime. In Figure 5.9b the measured elastic and viscous moduli E_1' and E_1'' are displayed with respect to the frequency, confirming the gel-like behavior of the monolayer as $E_1' > E_1''$. The frequency dependency of the $F10H16$ monolayer follows the same trend as of the tetrablock monolayers displaying a typical Kelvin-Voigt behavior. The lines in the plot correspond to fitting the model. Compared to di($F10H16$), the spring constant of the $F10H16$ monolayers is $\sim 18\,\%$ smaller ($g_{F10H16} = (134 \pm 1)\,\mathrm{mN\,m^{-1}}$,

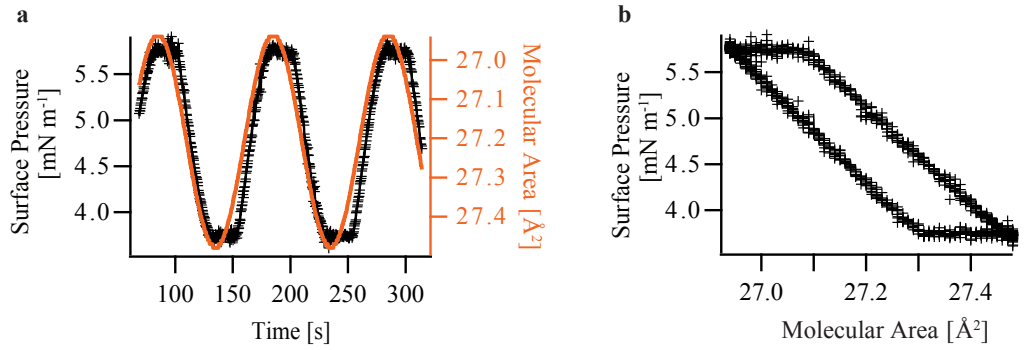

Figure 5.8.: **Dilational rheology of a *F*10*H*16 monolayer.** a) Response of the surface pressure π to oscillatory strain, the oscillation of the area is marked in red. b) Surface pressure response versus the oscillatory change of the area (Lissajou curve).

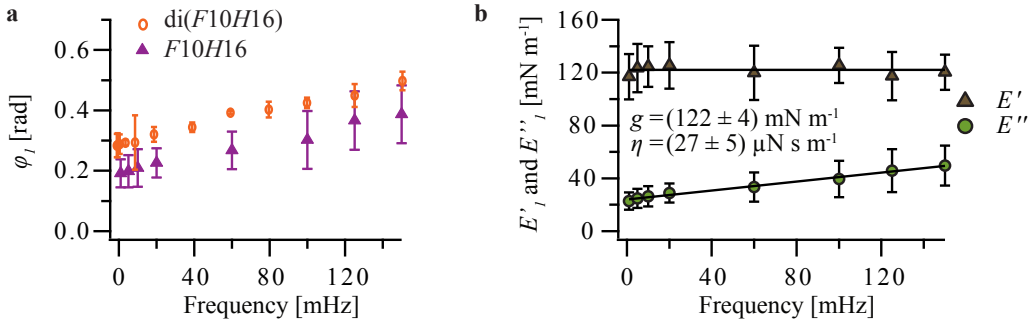

Figure 5.9.: **Dilational rheology of a *F*10*H*16 diblock monolayer compared to a di(*F*10*H*16) tetrablock monolayer.** a) Phase shift between stress and strain as a function of the frequency. b) Elastic and viscous modulus E_1' and E_1'' as a function of the frequency for a $F10H16$ monolayer. The solid lines correspond to the fits of the Kelvin-Voigt model.

$g_{\mathrm{di}(F10H16)} = (164 \pm 4)\,\mathrm{mN\,m^{-1}}$). The 2D viscosity on the other hand is similar for both monolayers, $\eta_{F10H16} \approx \eta_{\mathrm{di}(F10H16)} \approx 30\,\mu\mathrm{N\,s\,m^{-1}}$.

It is not surprising that the viscoelastic response of the $F10H16$ monolayers is predominantly elastic as the $F10H16$ molecules arrange in well defined circular surface micelles at the air/water interface, too, with the fluorocarbon segments pointing towards the air. The previous investigations already showed that the existence of the repulsive nanodomains is the reason for a strong elastic response to oscillatory shear and compression. Compared to the $F10H16$ monolayer, the tetrablock monolayers are obviously stiffer showing a higher spring constant. Actually, the same trend was observed in the interfacial shear measurements. Here, the tetrablock monolayers exceeded the sensitivity of the instrument exhibiting very high shear elastic moduli

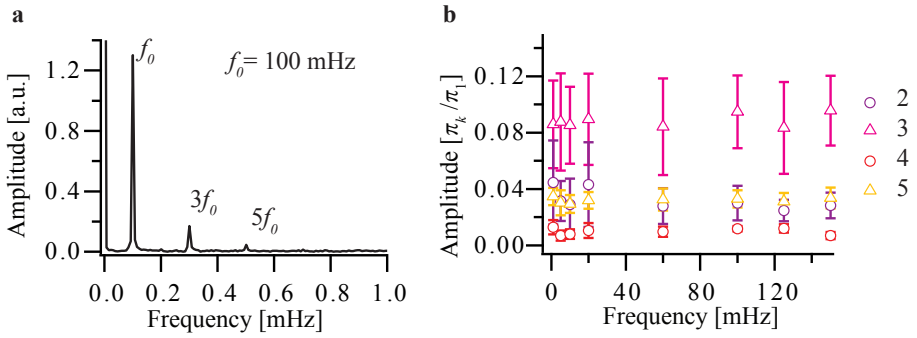

Figure 5.10.: **Nonlinear analysis of the dilational viscoelasticity of a $F10H16$ monolayer.** a) Fourier spectrum at $f = 100\,\text{mHz}$. b) Fractions of the higher mode Fourier amplitude with respect to the first mode π_k/π_1 as a function of the frequency.

at the same frequency and amplitude conditions where the $F10H16$ monolayer still showed a linear response. As elaborated in the discussion about the shear viscoelastic behavior (Section 4.3), the strong elastic response can mainly be attributed to the strong repulsive interaction between the nanodomains which is a result of the opposite dipole moments of the nanodomains. We could hence suggest that the $F10H16$ domains have a lower dipole moment compared to the di($F10H16$) domains. The net dipole moment of one domain depends on the size of the domain and the dipole moment of one molecule. The size of the two domains was determined using GISAXS. The results of the scattering data are in detail presented in Chapter 6. Indeed, they show that the sizes of the $F10H16$ and di($F10H16$) surface micelles are very similar (see Section 6.2.1). Therefore, the reduced spring constant can most probably be explained by a lower dipole moment of the $F10H16$ molecules compared to the di($F10H16$) molecules.

The interfacial viscosity η is the same for $F10H16$ and di($F10H16$) monolayers. As discussed above (Section 5.1.1), η is composed of the frictional forces between the surface micelles and the water subphase and the frictional forces between them. It is reasonable that both interactions are similar for the diblocks and tetrablocks systems.

The next step involves the analysis of the nonlinear contribution which was already clearly visible from the shape of the time-dependent surface pressure response $\pi(t)$ and the corresponding Lissajou curve (Figure 5.8). Indeed, just comparing the raw data between $F10H16$ and di($F10H16$) qualitatively does not show any major difference between the two systems. Therefore, one can expect that the nonlinear response

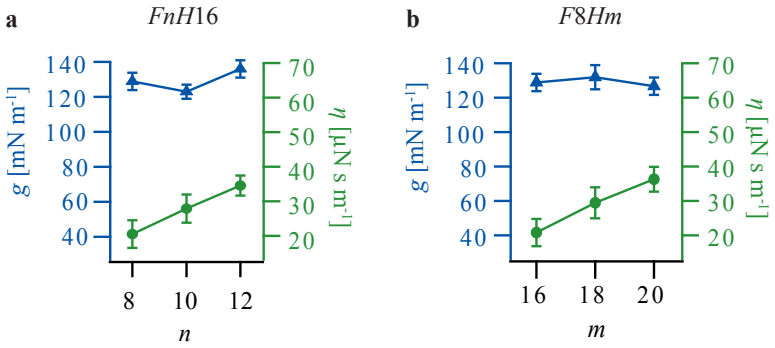

Figure 5.11.: **Spring constant g and interfacial viscosity η for various $FnHm$ monolayers.** g and η were obtained from fitting the Kelvin-Voigt model to the dilational elastic and viscous modulus E_1' and E_1''. g and η are given as a function of the hydrocarbon segment length for $F8Hm$ monolayers (a) and of the fluorocarbon segment length for $FnH16$ monolayers (b).

acts in a similar way. This can be confirmed by the shape of the Fourier transformation which is displayed in Figure 5.10a. As observed for the tetrablock monolayers, the $F10H16$ monolayer exhibits an increased 1st, 3rd and 5th Fourier mode whereas the even and higher modes are in the noise regime of the measurement. To further analyze this behavior, the fractions of the higher Fourier modes with respect to the first Fourier modes are plotted versus the frequency in Figure 5.10b, showing that the 3rd mode has the highest contribution with $\pi_3/\pi_1 \approx 0.08$ which is lower than for the di($F10H16$) monolayers ($\pi_3/\pi_1 \approx 0.12$). The degree of nonlinearity was determined by calculating the THD. As it is independent of the frequency, the value was averaged over the frequency regime obtaining $THD_{F10H16} = (10.3 \pm 0.5)\,\%$, which is slightly lower than the corresponding value for the di($F10H16$) monolayer ($THD_{\mathrm{di}(F10H16)} = (12.5 \pm 0.9)\,\%$).

As discussed before, the emergence of the nonlinearity was attributed mainly to the strong elastic response. Indeed, the tetrablock monolayer which show a stronger elastic response compared to the diblock monolayer also has a slightly higher nonlinear fraction. This effect is most prominent in the 3rd mode which has the highest contribution in the nonlinear elastic part. To conclude, the $F10H16$ diblock and the di($F10H16$) tetrablock monolayers show a very similar dilational viscoelastic response. The spring constant of the diblock monolayer is reduced compared to the tetrablock monolayer which goes in line with a slightly lower degree of nonlinearity.

5.2.2. Influence of Hydrocarbon and Fluorocarbon Segment Length

In order to assess the influence of the hydrocarbon and fluorocarbon segment length, dilational rheology measurements were performed on $F8H16$, $F12H16$, $F8H18$ and $F8H20$ diblock monolayers under the same conditions. The other $FnHm$ monolayers behave similar to the $F10H16$ monolayer, following a Kelvin-Voigt behavior which provides the spring constant g and interfacial viscosity η. Figure 5.11 shows g and η with respect to the hydrocarbon segment length m and the fluorocarbon segment length n. An overview of the frequency dependent E_1' and E_1'' values is given in Figure A.7.

Interestingly, irrespective of n and m, all $FnHm$ diblocks have similar spring constants, $g_{FnHm} \approx 130\,\mathrm{mN\,m^{-1}}$. The interfacial viscosity on the other hand depends on the length of the $FnHm$ molecule, increasing monotonically both with n and m. Elongating either the fluorocarbon or the hydrocarbon part by a length of 2 carbons leads to an increase of the 2D viscosity by $\sim 7\,\mu\mathrm{N\,s\,m^{-1}}$. In fact the same tendency was observed for the di($F10Hm$) monolayers. The interfacial viscosity results from two effects: 1) the loss of energy due to the friction between the domains and the water subphase, 2) the frictional coupling between the domains. An increase of the molecular length can influence both effects. On one hand, longer hydrocarbon chains may have a larger contact area with the water increasing the frictional forces, on the other hand, longer fluorocarbon chains may lead to increased frictional forces due to an increased contact area between the individual domains.

In the interfacial shear rheology experiments presented in Chapter 4, an increase of the interfacial viscosity with hydrocarbon and fluorocarbon segment length was observed as well. Contrary to the elastic modulus, the viscous response of the $FnHm$ systems should rather be independent of the type of strain (shear or compression/expansion) applied to the system. In both cases, it mainly results from the friction between the domains and the water and between the domains themselves. Therefore, although interfacial shear rheology and interfacial dilational rheology are two complementary methods, in case of the viscous response one can expect similar values in the same order of magnitude. The viscous moduli itself can not be compared since they depend on the applied oscillation frequency and amplitude. However, the interfacial viscosity η obtained from fitting the Kelvin-Voigt model is independent of the frequency and can be used to compare the two methods. In case of the $F8H18$ monolayers at $5\,\mathrm{mN\,m^{-1}}$, the interfacial viscosity measured with both methods is $\eta_{\mathrm{shear}} = (38 \pm 1)\,\mu\mathrm{N\,s\,m^{-1}}$ and $\eta_{\mathrm{dilational}} = (23 \pm 6)\,\mu\mathrm{N\,s\,m^{-1}}$. Indeed, the two values are of the same order of magnitude although they are not equal within the error tol-

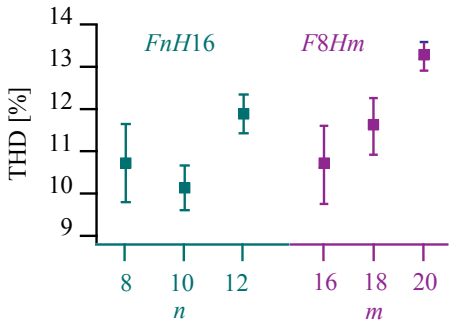

Figure 5.12.: **THD of *FnHm* monolayers** as a function of the hydrocarbon segment length m and the fluorocarbon segment length n

erance. An applied shear indeed may lead to increased frictional coupling between the domains compared to an compression and expansion of the films: When shear is applied, the contact area between the circular shaped domains is larger compared to a dilational movement where only small parts of the domains move against each other.

Finally, the influence of the hydrocarbon and fluorocarbon segment length m and n on the nonlinear viscoelastic response of the $FnHm$ monolayers was studied. Figure 5.12a displays the THD values averaged over the whole frequency regime for all $FnHm$ monolayers with respect to n and m. The THD of $F8H16$ and $F10H16$ were similar, THD $\approx 10\,\%$, whereas increasing n further to $F12H16$ yields in $\mathrm{THD}_{F12H16} = (11.8 \pm 0.5)\,\%$. On the other hand, an increase of the hydrocarbon segment length leads to a stronger nonlinear response of the film, $\mathrm{THD}_{F8H20} = (13.2 \pm 0.3)\,\%$. Interestingly, comparing the diameter of the $FnHm$ surface micelles with the THD reveals that the $FnHm$ monolayers with the larger surface micelles show a stronger nonlinear response (see Section 6.2). In the previous section the rise of a nonlinear signal could be explained phenomenologically by a first order phase transition. A possible explanation of the dependency of the THD with m could hence be a different ordering of the larger surface micelles compared to the smaller surface micelles.

6. GISAXS of Semifluorinated Alkane Monolayers

Although Gaines et al. found that semifluorinated alkanes form stable Langmuir monolayers on water already in 1991[26], it took 10 more years to find out in what way the molecules are ordered at the interface.[65] Transferring the monolayers from water to solid substrates via Langmuir-Blodgett and imaging them with AFM revealed the self-assembly of semifluorinated alkanes diblocks into well-ordered nantometer-sized surface micelles.[24,65,78] This approach is extremely helpful in order to obtain a first picture about the structure of the monolayers, however one cannot exclude that the transfer of the monolayer from the air/water interface to a solid substrate alters the order, the size and especially the shape of the surface micelles.

Another 10 years later, the presence of the surface micelles composed of $F8Hm$ diblocks directly on water was further confirmed using GISAXS.[6] This allowed to determine the size of the surface micelles by the the lattice parameter which can be obtained by the peak positions of the scattering signal.[6] However, such procedures often over-estimate the size of the domains when they are closely packed as it is the case for the semifluorinated alkanes.

In this chapter, the scattering data obtained from GISAXS on monolayers of semifluorinated $FnHm$ diblocks and di($F10Hm$) tetrablocks at the air/water interface was fitted by taking both the structure factor and the form factor into account. This allows a precise determination of the sizes and the shapes of the surface micelles. The GISAXS data of the three tetrablock systems di($F10Hm$), $m = 16, 18, 20$ are presented in Section 6.1. In particular it contains the calculation of the exact dimensions of the surface micelles and their change in shape and size upon compression of the monolayer. Additionally, the correlation length was determined. Section 6.2 contains a short presentation of the GISAXS results obtained for the $F8Hm$ ($m = 14, 16, 18, 20$) and $FnH16$ ($n = 8, 10, 12$) diblocks. The results demonstrate how a subtle change of the molecular structure influences the size and correlation of the surface micelles.

The results presented in this Chapter were recently published in ChemPhysChem

in two publications addressing the di($F10Hm$) tetrablocks (2019) and the $FnHm$ diblocks (2017) separately.[1]

6.1. GISAXS of Semifluorinated Tetrablocks

This section shows the GISAXS data and analysis for di($F10H16$), di($F10H18$) and di($F10H20$) tetrablock monolayers at the air/water interface. So far, there are no X-ray studied of the tetrablock systems. The shape and size of the surface micelles was only determined by imaging transferred monolayers with AFM.[19]

6.1.1. Dependence of the Size and Correlation of the Surface Micelles on the Molecular Length

Figure 6.1a shows the GISAXS signal of a di($F10H20$) monolayer in a 2D reciprocal coordinate system using Equation 2.56 at a surface pressure of $\pi = 5\,\mathrm{mN\,m^{-1}}$. A detailed description about how the data were recorded is given in Section 3.2.4. Rod-like scattering features were observed which demonstrate that the di($F10H20$) molecules form domains that arrange in a 2D lattice. The intensity, integrated along $q_y = 0.9$ and $1.1\,\mathrm{nm^{-1}}$ is displayed in Figure 6.1b. It was fitted using the structure factor $S(q_y)$ and the form factor $F(q_y)$ according to Equation 2.57. In a first step, the best combination of models for form factors and structure factors need to be chosen. For the tetrablock monolayers, a form factor was found to be provide the best fitting results which models the surface micelles as oblate hemiellipsoids in the framework of DWBA. This takes the multiple scattering by the self-assembled surface micelles into consideration (see Section 2.4.2). The dimensions are schematically shown in Figure 6.2. The hemiellipsoids have the in-plane axes D_x and D_y and the height H. The form factor is given by

$$F(q_y) = 2\pi \int_0^H r_{x,z} r_{y,z} \frac{J_1(r_z)}{r_z} \mathrm{e}^{iq_z z}\,\mathrm{d}z \tag{6.1}$$

[1] Abuillan, W., Veschgini, M., *Mielke, S.*, Yamamoto, A., Liu, X., Konovalov, O., Krafft, M. P., & Tanaka, M. (2019). **LongRange Lateral Correlation between Self-Assembled Domains of Fluorocarbon-Hydrocarbon Tetrablock by Quantitative GISAXS.** *ChemPhysChem. 20*(6), 898-904.
Veschgini, M., Abuillan, W., Inoue, S., Yamamoto, A., *Mielke, S.*, Liu, X., Konovalov, O., Krafft, M. P., & Tanaka, M. (2017). **Size, Shape, and Lateral Correlation of Highly Uniform, Mesoscopic, Self-Assembled Domains of Fluorocarbon-Hydrocarbon Diblocks at the Air/Water Interface: A GISAXS Study.** *ChemPhysChem, 18*(19), 2791-2798.
I performed parts of the analysis and contributed in the structuring and interpretation of the data.

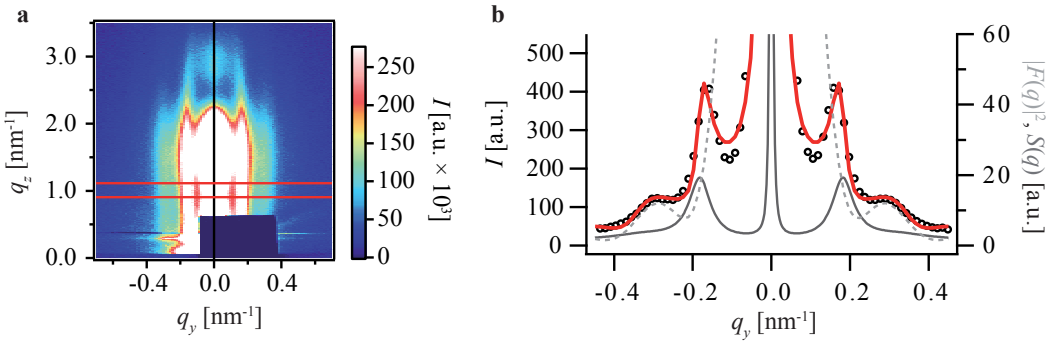

Figure 6.1.: **GISAXS signal intensity of a di($F10H20$) monolayer plotted in a 2D reciprocal coordinate system.** The monolayer was compressed to $\pi = 5\,\mathrm{mN\,m^{-1}}$. a) Readout of the 2D detector. The dark spot at $q_z \approx 0$ is the beam stop which conceals the strong intensity of the direct beam. b) Intensity profile along q_y, integrated between $q_z = 0.9$ and $1.1\,\mathrm{nm^{-1}}$, indicated by the two dashed lines in panel a) (open circles). The red line represents the fitted intensity, including the structure factor (solid gray line) and the form factor (dashed gray line).

where

$$r_{x,z} = \frac{D_x}{2}\sqrt{1-\left(\frac{z}{H}\right)^2} \tag{6.2}$$

$$r_{y,z} = \frac{D_y}{2}\sqrt{1-\left(\frac{z}{H}\right)^2} \tag{6.3}$$

$$r_z = \sqrt{(q_x r_{x,z})^2 + (q_y r_{y,z})^2} \tag{6.4}$$

and $J_1(r_z)$ represents the Bessel function of the first kind.

The structure factor $S(q_y)$ on the other hand was calculated within the framework of the paracrystal theory. The best fit could be obtained by using a structure factor representing an rectangluar paracrystal lattice with the mean lattice parameters L_x and L_y with the standard deviations σ_x and σ_y. It is given by

$$S(q_\parallel) = \prod_{k=x,y} \frac{1-\exp\left(-q_\parallel^2\sigma_k^2\right)\exp\left(-\frac{2L_k}{\xi}\right)}{1-2\exp\left(\frac{q_\parallel^2\sigma_k^2}{2}\right)\exp\left(-\frac{L_k}{\xi}\right)\cos(q_k L_k)+\exp\left(-q_\parallel^2\sigma_k^2\right)\exp\left(-\frac{2L_k}{\xi}\right)} \tag{6.5}$$

where ξ is the correlation length and $q_\parallel$ is given by

$$q_\parallel = \sqrt{q_y^2 + q_x^2} \approx q_y. \tag{6.6}$$

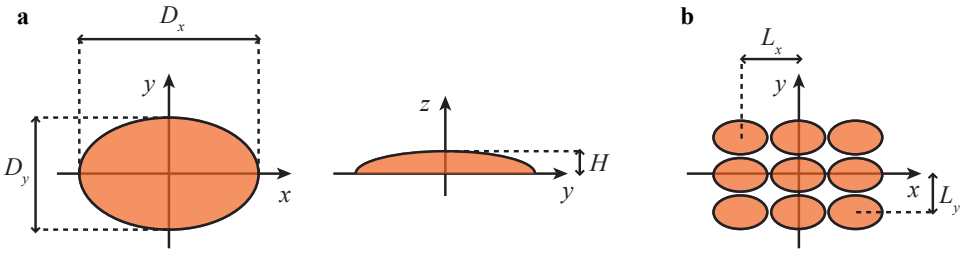

Figure 6.2.: **Model of form factor and structure factor used to fit the di($FnHm$) tetrablock GISAXS data.** a) The shape of the surface micelles could be best fitted using form factor was which represents a hemiellipsoid with the major axis D_x, the minor axis D_y and the height H. b) The ordering of the surface micelles could be best described by a structure factor $S(q_y)$ which represents a rectangular lattice with the two lattice constants L_x and L_y.

To obtain a good fitting result, both the structure factor and the form factor are necessary. In Figure 6.1 the fits of the structure factor and form factor are indicated. They show that the di($F10H20$) molecules arrange in hemiellipsoids with the major and minor axis being $D_x = (42 \pm 2)\,\mathrm{nm}$ and $D_y = (37 \pm 2)\,\mathrm{nm}$ respectively. The height was measured to be $H = (4.7 \pm 0.5)\,\mathrm{nm}$ which corresponds approximately to the molecular length of one di($F10H20$) molecule. Since the lattice parameters L_x and L_y are comparable to the major and minor axes ($D_x/L_x \approx D_y/L_y \approx 1$) one can assume that the domains are tightly packed into an orthorhombic lattice.

The integrated intensities of GISAXS data obtained from the monolayers composed of di($F10H16$) and di($F10H18$) surface micelles are shown in Figure 6.3. The same model hemiellipsoids arranged in a orthorhombic lattice was used for the fitting and yielded excellent agreement with the raw data. This further confirms that the model describes the shape and order of the tetrablock surface micelles well.

The sizes of the surface micelles for the three different di($F10Hm$) tetrablock molecules were measured at a surface pressure of $5\,\mathrm{mN\,m^{-1}}$. Interestingly, both axes of the hemiellipsoid increase with the hydrocarbon segment length as shown in Figure 6.4a. The total area of the ellipsoid surface micelles is $A_{\mathrm{di}(F10H16)} = 676\,\mathrm{nm}^2$, $A_{\mathrm{di}(F10H18)} = 803\,\mathrm{nm}^2$ and $A_{\mathrm{di}(F10H20)} = 1220\,\mathrm{nm}^2$.

What is the origin of the increase of the size of the surface micelles with the increase of the molecular length of the tetrablock molecules? In the case of 2D lipid domains, the size of the domains was predicted to be mainly governed by two aspects: The line tension λ which minimizes the boundary length of the domains and the repulsive dipole interactions between the molecules within the surface micelles.[73]

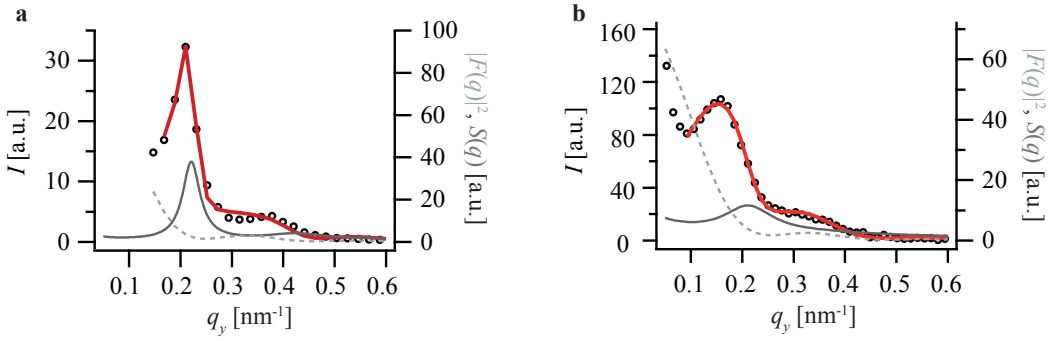

Figure 6.3.: **Integrated GISAXS signals of a di($F10H16$) monolayer (a) and a di($F10H18$) monolayer (b).** The red line represents the fitted intensity, including the structure factor (solid gray line) and the form factor (dashed gray line).

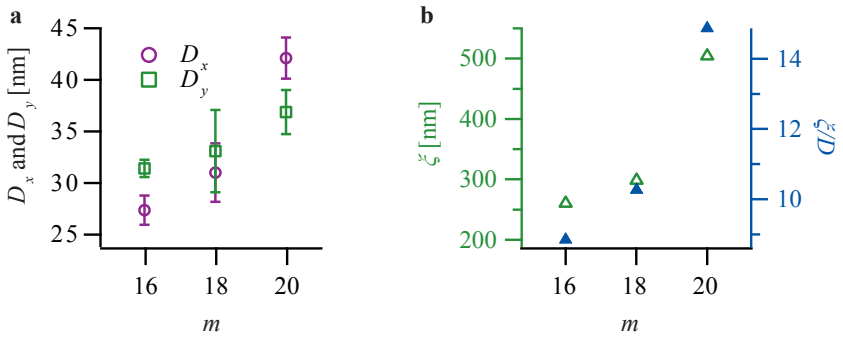

Figure 6.4.: **Diameters and correlation lengths obtained from GISAXS data of di($F10Hm$) monolayers ($m = 16, 18, 20$) with respect to the hydrocarbon segment length m.** a) In-plane axes D_x and D_y of the hemiellipsoid shaped surface micelles. b) Correlation length ξ and normalized correlation length ξ/D.

The equilibrium radius of one domain was suggested to be

$$R_{eq} \propto \exp\left(\frac{\lambda}{\mu^2}\right) \tag{6.7}$$

where μ corresponds to the difference in the dipole density between the domain and the surrounding phase. In case of the semifluorinated alkanes, the molecular dipole moment is mainly determined by the CF_3 groups and the $CF_2 - CH_2$ junction and is predicted to be independent from the length of the molecule.[12] Therefore, the increase in size can be attributed to an increase of the line tension.

The precise fitting of the integrated intensity allows the calculation of the correlation length by the width of the first peak of the structure factor as described in Section 2.4.2. The calculated correlation lengths for the three different di($F10Hm$) tetrablock monolayers are represented in Figure 6.4b with respect to the hydrocarbon segment length m. ξ increases monotonically with the hydrocarbon segment length which may result from larger sizes of the surface micelles for the longer tetrablock molecules. The correlation length is much larger than the size of the surface micelles. In order to quantify this further, it was normalized by the average diameter of the surface micelles $D = (D_x + D_y)/2$ which shows that the correlation reaches distances $8 - 14$ times higher than the size of one surface micelle. This is depicted in Figure 6.4b. These normalized correlation lengths are very high and distinctly larger compared to those of perfluorinated surfactants which are incorporated into phospholipid matrices where $\xi/D_{\text{lipid}} = 3 - 4$.[84] Interestingly, the normalized correlation length ξ/D also increases with the hydrocarbon segment length. This means that the monotonic increase of ξ with m can not only be explained by an increase of the size of the surface micelles but most probably results from increased interactions between the larger surface micelles.

6.1.2. Deformability of the Surface Micelles

So far, all measurements were performed at the constant surface pressure of $\pi = 5\,\text{mN}\,\text{m}^{-1}$. In order to assess how the surface micelles react upon compression, GISAXS data at $\pi = 0.5\,\text{mN}\,\text{m}^{-1}$ and $\pi \approx 10\,\text{mN}\,\text{m}^{-1}$, close to the collapse of the monolayer, were recorded. The respective integrated intensity signals are shown in Figure 6.5. In all three cases, the positions of the characteristic features are shifted to higher q_y values when the monolayers are compressed. This represents a decrease of the lengths of the domains in y-direction which is the direction of the compression of the monolayer. Therefore, compressing the monolayer in y-direction leads to an

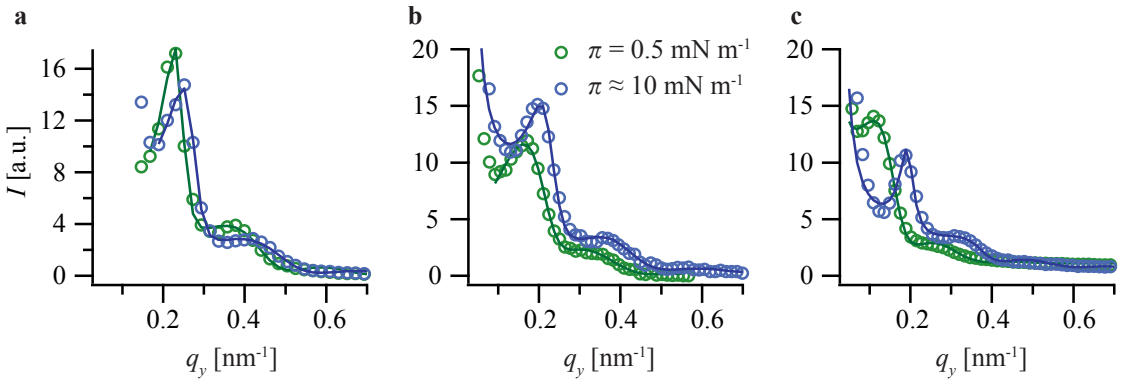

Figure 6.5.: **Influence of the surface pressure on the GISAXS signal of di($F10Hm$) monolayers.** The GISAXS data at $\pi = 0.5\,\mathrm{mN\,m^{-1}}$ and $\pi \approx 10\,\mathrm{mN\,m^{-1}}$ of di($F10H6$) (a), di($F10H18$) (b) and di($F10H20$) (c) monolayers. The lines corresponds to the best fit using the structure factor and form factor.

decrease of D_y. In the same time, the in-plane axis D_x increases, whereas the area of surface micelles stays constant. In the case of di($F10H16$) for example an increase of the surface pressure from $\pi = 0.5\,\mathrm{mN\,m^{-1}}$ to $\pi = 9.5\,\mathrm{mN\,m^{-1}}$ leads to a decrease of D_y from $(29 \pm 1)\,\mathrm{nm}$ to $(26 \pm 1)\,\mathrm{nm}$ whereas D_x increases from $(30 \pm 1)\,\mathrm{nm}$ to $(34 \pm 1)\,\mathrm{nm}$ with the area of the surface micelle remaining $A \approx 690\,\mathrm{nm^2}$. The same trend was observed for the di($F10H18$) and di($F10H20$). The results hence demonstrate that the surface micelles composed of di($F10Hm$) tetrablock molecules undergo an elliptic deformation in the direction of the compression from an almost circular shape at $\pi \approx 0\,\mathrm{mN\,m^{-1}}$ to an elliptical shape just before the collapse of the monolayer whereas the integrity of the individual surface micelles stays intact.

6.2. GISAXS of Semifluorinated Diblocks

GISAXS data were recorded monolayers of $FnHm$ diblocks at the air/water interface, as well. In a first step, the data of $F10H16$ are presented. In a next step, the molecules $F8H16$, $F8H18$, $F8H20$, $F10H16$, $F12H16$ were investigated which allows to study the influence of both, the hydrocarbon and the fluorocarbon segment length on the size and shape of the surface micelles.

6.2.1. Size, Shape and Correlation of *F10H16* Surface Micelles

Figure 6.6a displays the integrated scattering intensity of a monolayer composed of $F10H16$ surface micelles at the surface pressure of $\pi = 5\,\mathrm{mN\,m^{-1}}$. The intensity profile was obtained as explained in the previous section and in Section 3.2.4. In

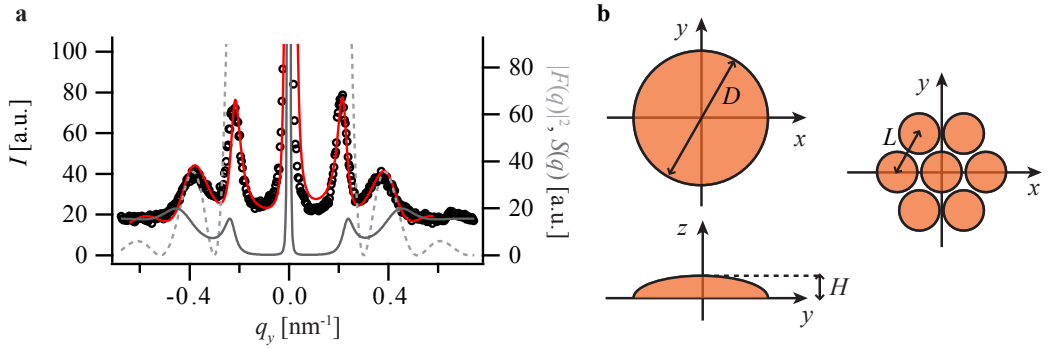

Figure 6.6.: **Integrated GISAXS signal intensity of a $F10H16$ monolayer plotted in a 2D reciprocal coordinate system.** a) Intensity profile along q_y, integrated between $q_z = 1.0$ and $1.2\,\mathrm{nm}^{-1}$. The monolayer was compressed to $\pi = 5\,\mathrm{mN\,m}^{-1}$. The red line represents the fitted intensity, including the structure factor (solid gray line) and the form factor (dashed gray line). b) The shape of the surface micelles could be best fitted using form factor was which represents a hemispheroid with the diameter D and the height H. The ordering of the surface micelles could be best described by a structure factor $S(q_y)$ which represents a hexagonal lattice with the lattice constant L.

order to fit it using Equation 2.57, a suitable form factor and structure factor needed to be found. The fit shown in Figure 6.6a was obtained by applying the form factor

$$F(q) = 2\pi \int_0^H \frac{D^2}{4}\left(1-\left(\frac{z}{H}\right)^2\right) J_1\left(\frac{D}{2}\sqrt{(q_x^2+q_y^2)\left(1-\left(\frac{z}{H}\right)^2\right)}\right)\exp(-iq_z z)\,\mathrm{d}z \tag{6.8}$$

which describes oblate hemispheroids with a diameter D and a height H. J_1 represents the first order Bessel function of the first kind.

The structure factor representing the data best was that of a 2D hexagonal lattice,

$$S(q) = \frac{(1-\phi^2)^2}{(1+\phi^2-2\phi\cos(q_y L))\left(1+\phi^2-2\phi\cos\left(\frac{q_y L}{2}+\frac{\sqrt{3}q_x L}{2}\right)\right)} \tag{6.9}$$

with L being the lattice constant and

$$\phi = \exp\left(\frac{-(q_x^2+q_y^2)\sigma^2}{2}\right)\exp\left(-\frac{L}{\xi}\right). \tag{6.10}$$

σ is the standard deviation of L and ξ the correlation length. The dimensions are illustrated schematically in Figure 6.6b. According to this fit, the $F10H16$

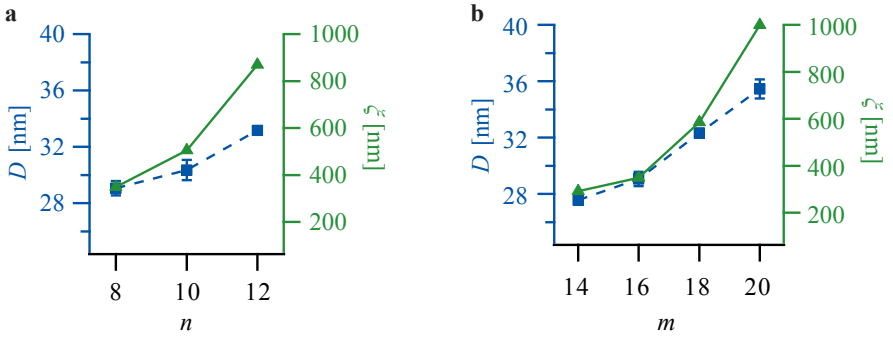

Figure 6.7.: **Diameter D and correlation length ξ of $FnHm$ surface micelles obtained from GISAXS.** a) D and ξ for $FnH16$ ($n = 8, 10, 12$) monolayers. b) D and ξ for $F8Hm$ ($m = 14, 16, 18, 20$) monolayers.

self-assemble into circular shaped surface micelles which have a diameter of $D = (30 \pm 1)\,\mathrm{nm}$ and a height of $H = (4.9 \pm 0.9)\,\mathrm{nm}$. The lattice parameter is comparable to the diameter of one surface micelle which means that they are tightly packed into the hexagonal lattice. The correlation length ξ was calculated using the same approach as in Section 2.4.2 taking into account the width of the first peak of the structure factor, yielding $\xi = 505\,\mathrm{nm}$ which is 17 times larger than the size of one surface micelle.

These results demonstrate that there are several differences between the surface micelles of the $F10H16$ diblock molecules and the di($F10H16$) tetrablock molecules that exhibit the same molecular length: First, the $F10H16$ molecules self-assemble in completely circular shaped surface micelles whereas the tetrablock molecules could be better fitted using a form factor which represents hemiellipsoid shapes. The size of the $F10H16$ surface micelles however is slightly larger than the size of the di($F10H16$) surface micelles ($A_{F10H16} = 724\,\mathrm{nm}^2$, $A_{\mathrm{di}(F10H16)} = 676\,\mathrm{nm}^2$). This can be explained by the stronger packing strain of the di($F10H16$) molecules. It further suggests that the diblock surface micelles are composed of a higher number of molecules than the tetrablock surface micelles since the tetrablock molecules have larger steric requirements. The correlation between the $F10H16$ surface micelles is distinctly higher than the correlation between the tetrablock surface micelles. This can be attributed to a more regular shape and hence higher order of the diblock surface micelles.

6.2.2. Influence of the Block Length

In a next step, the influence of the hydrocarbon and fluorocarbon segment length m and n on the size and correlation of the surface micelles was investigated. The results are summarized in Figure 6.7 and Table A.1. For all other $FnHm$ diblocks, the intensity profile could be well fitted using a form factor which describes circular domains and a structure factor which accounts for a 2D hexagonal lattice.

Both the elongation of m or n leads to an increase of the diameter. Equivalently to the approach described for the tetrablock system, this increase in the size of the surface micelles can be attributed to an increase in the line tension due to increased van der Waals interactions. The fact that the increase of the diameter seems less pronounced in case of the increasing fluorocarbon segment length compared to the hydrocarbon segment length might be attributed to the lower polarizability of the fluorocarbon chains. The values obtained for the diameters of the $FnHm$ surface micelles are comparable or lower than that measured by Bardin et al who performed similar experiments.[6] However, they only used the peak position of the scattering signal to derive the diameter. This obviously leads to an overestimation of the size of the densily packed surface micelles.

The correlation length ξ which was calculated from the width of the structure factor shows an increase with the fluorocarbon and hydrocarbon segment length as well. Also, calculating the normalized correlation length ξ/D demonstrates that the lateral correlation between the surface micelles reaches distances over $10-26$ longer than the diameter of the single domain. Additionally, ξ/D monotonically increases with the increase of the molecular length of the diblocks. This indicates that the increase of ξ with the molecular length can not only be explained by increasing sizes of the surface micelles but might be understood by stronger inter-domain repulsions for larger surface micelles.

7. Influence of Perfluorohexane Vapor on the Structural and Viscoelastic Properties of Semifluorinated Alkanes at the Air/Water Interface

One of the most promising applications of semifluorinated alkane monolayers is their use as microbubble contrast agents for sonographic imaging. Due to their hydrophobic nature and the strong elastic response they are expected to increase the stability of microbubbles in the blood. Indeed it was shown that they stabilize lipid vesicles.[22,95] In the recent scientific progress of microbubble research, PFH is playing an important role as it was shown that the lifetime of lipid microbubbles filled with PFH vapor is $4-5$ times larger than that of microbubbles filled with air.[104] This is important as so far the microbubbles available on the market lack in stability. The stabilizing effect of PFH originates from the extremely low water solubility of PFH ($2.7 \times 10^{-4}\,\mathrm{mol\,m^{-3}}$ compared to $0.48\,\mathrm{mol\,m^{-3}}$ for oxygen).[35,44] Combining microbubbles of PFH vapor with a shell composed of semifluorinated alkanes would hence be a promising candidate for very long-living microbubbles. Therefore it is crucial to understand the effect of PFH-enriched gas on the mechanics of semifluorinated alkane monolayers on water which is the principle aim of this chapter.

Previous studies showed that fluorocarbons present in the gas phase have an effect on the physical properties of 2D surfactant films at the air/water interface.[27,28,82] PFH itself is adsorbed at the air/water interface and reduces the surface tension of water by $2-5\,\mathrm{mN\,m^{-1}}$.[15] It was demonstrated that fluorocarbon gases lead to a fluidization of DPPC Langmuir monolayers by inhibiting the LE/LC phase transition during compression.[28] Recent studies even showed that an atmosphere saturated with PFH helps the adsorption of albumin on the air/water interface. In particular, such an atmosphere increases the protein adsorption when both albumin and lipids are present.[27,82] This makes fluorocarbon gas a promising candidate for the therapeutic treatment of patients with acute respiratory distress syndrome.

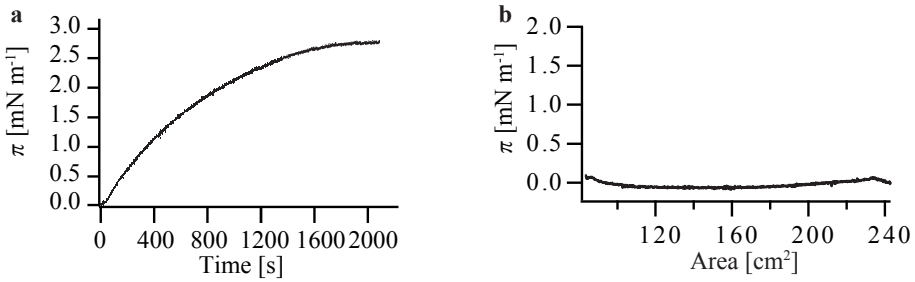

Figure 7.1.: **Adsorption/desorption of PFH on water.** a) Saturation of PFH over time. b) π/A-isotherm of pure PFH adsorped at the air/water interface. The surface pressure was set to $0\,\mathrm{mN\,m^{-1}}$ prior to the compression and the surface area was compressed with the speed $3.75\,\mathrm{cm^2\,min^{-1}}$.

The effect of PFH on $FnHm$ monolayers at the air/water interface has not been studied yet. Mourran et al. observed that perfluorocarbon vapors can change the macroscopic structure of self-assembled 2D films of semifluorinated alkanes on solid substrates such as mica and glass.[78] More explicitly, they saw a transition of the monolayer structure from straight to bent ribbons when treating a supported monolayer of $F14H20$ with hexafluoroxylene. It can hence be suspected that besides adsorbing to the water surface, PFH molecules may interact with the $FnHm$ molecules, maybe even altering their self-assembly into the nanodomains. The impact of PFH present in the gas phase on monolayers of $FnHm$ molecules on water was studied using different approaches: In a first step, π/A-isotherms were recorded allowing the calculation of the compressibility (Section 7.1). In a next step, analogous to the measurements in air, interfacial dilational rheology experiments were performed and the elastic and viscous moduli were calculated (Section 7.2). The nonlinearity of the response function was assessed as well. Additionally, in order to study the effect of PFH on the structure of the nanodomains, GISAXS measurements were performed which provide information about the shape, size and correlation of the domains (Section 7.3). This chapter focuses on the molecules $F8H16$, $F10H16$ and $F12H16$ to study the effect of the fluorocarbon segment length. The results of $F8H18$ and $F8H20$ are very similar and are therefore presented in the Appendix (Figure A.9).

The results of this chapter have been submitted to ChemPhysChem.[1]

[1] *Mielke, S.*, Abuillan, W., Veschgini, M., Liu, X., Konovalov, O., Krafft, M. P., & Tanaka, M. (2019). **Influence of a Perfluorohexane-enriched Atmosphere on the Viscoelasticity and Structural Order of Self-assembled Nanodomains of Semifluorinated Alkanes at the Air/Water Interface.** submitted to ChemPhysChem
I performed all experiments, analyzed and interpreted the data and wrote the major part of the manuscript.

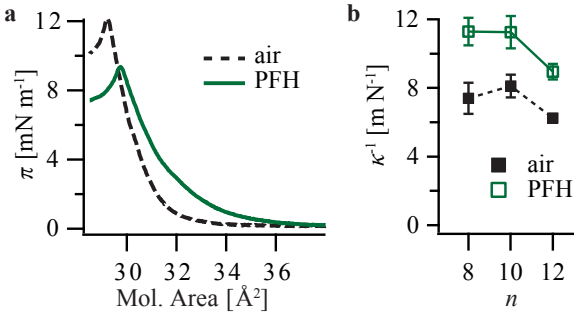

Figure 7.2.: **Influence of PFH on π/A-isotherms of $FnHm$ monolayers.** a) π/A-isotherms of $F8H16$ monolayers in air and in a PFH-enriched atmosphere. The data were recorded with a compression speed 3.75 cm^2 min^{-1} at 20°C. b) Compressibility κ^{-1} of $FnH16$ isotherms in air and in a PFH-enriched atmosphere obtained from the π/A-isotherms at $\pi = 5\,\mathrm{mN\,m^{-1}}$.

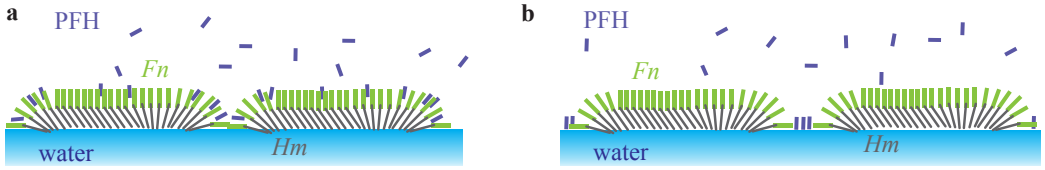

Figure 7.3.: **Scenarios of PFH molecules interacting with the $FnHm$ nanodomains.** a) Intercalation of the PFH molecules into the nanodomains. b) Adsorption of the PFH molecules to free spaces between the nanodomains on the air/water interface.

7.1. π/A-Isotherms

PFH in the atmosphere was shown to lead to an increase of the surface pressure.[15] In our experiments, the surface pressure increased to a maximum value of $\pi = 2.5 - 3\,\mathrm{mN\,m^{-1}}$ which was reached after ~ 30 min (Figure 7.1). In Section 3.2.3 the procedure to obtain an atmosphere enriched with PFH is described. The increase of the surface pressure can be attributed to the adsorption of the PFH from the gas phase to the air/water interface. Compressing the surface of the film balance without any surfactants present besides PFH adsorbed from the gas phase did not show any features. Instead the surface pressure stayed constant during the compression (Figure 7.1). It can therefore be concluded that the adsorption of PFH from the gas phase to the water surface is weak and the molecules desorb during compression.

At high surface areas, one can assume that both the $FnHm$ molecules and the PFH molecules are present at the air/water interface. π/A-isotherms of a $F8H16$ monolayer in air and in an PFH-enriched atmosphere are exemplarily shown in Figure

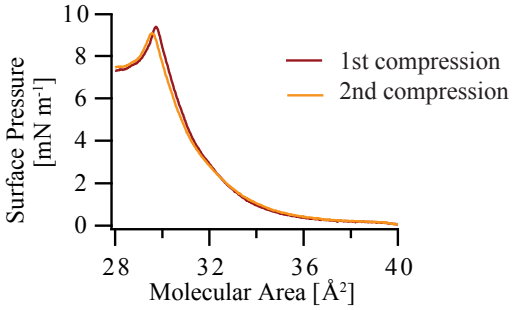

Figure 7.4.: **Reversibility of π/A-isotherms of a $F8H16$ monolayer.** After compressing the monolayer with speed of $3.75\,\mathrm{mN\,m^{-1}}$, the barriers were fully opened and the monolayer was allowed to equilibrate for 5 min before starting a second compression.

7.2a. In the presence of PFH, the onset of the increase in the surface pressure appeared at a larger area per molecule ($A \approx 36\,\mathrm{Å}^2$), while the surface pressure increase in air was observed at $A \approx 33\,\mathrm{Å}^2$. The shape of the isotherms which is typical for the incompressible nanodomains stays intact. Besides the different onset of the surface pressure increase, the collapse pressure of the $F8H16$ monolayer in PFH-enriched atmosphere was lower than that in air ($\pi_{c,\mathrm{PFH}} \approx 9\,\mathrm{mN\,m^{-1}}$, $\pi_{c,\mathrm{air}} \approx 11\,\mathrm{mN\,m^{-1}}$). The lateral compressibility κ^{-1} was calculated from the isotherms at the surface pressure of $\pi = 5\,\mathrm{mN\,m^{-1}}$. As may be suggested from the shape of the π/A-isotherms, the compressibility in the PFH-enriched atmosphere $\kappa^{-1}_{F8H16,\mathrm{PFH}} = 11.3\,\mathrm{m\,N^{-1}}$, is distinctly higher compared to the value in air $\kappa^{-1}_{F8H16,\mathrm{air}} = 7.4\,\mathrm{m\,N^{-1}}$. The same tendency was also observed for all the other $FnHm$ molecules as depicted in Figure 7.2b. Since the $FnHm$ domains expose the fluorocarbon segments to the atmosphere, PFH molecules are either intercalated into the fluorocarbon segments of the nanodomains or adsorbed on the free water surface between the domains. These two scenarios are illustrated schematically in Figure 7.3.

To further investigate the behavior of PFH, two isothermal π/A compressions were recorded in a row. In Figure 7.4, two π/A-isotherms of $F8H16$ in the PFH-enriched atmosphere are shown. After compressing for the first time, the barriers were fully opened and compressed again after waiting for 5 min. Clearly, the isothermal compression is completely reversible which suggest that the PFH molecules either do not desorp from the air/water interface or if they desorp they get readsorped quickly.

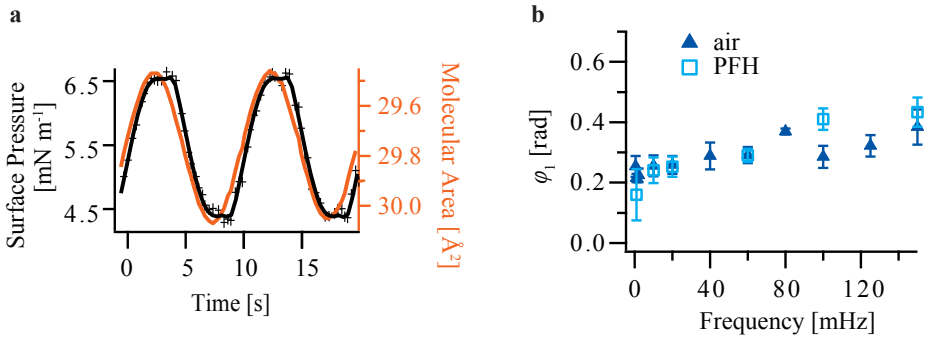

Figure 7.5.: **Dilational rheology of a $F8H16$ monolayer in air and in PFH-enriched atmosphere.** a) The applied strain $A(t)$ (red) and the recorded stress response $\pi(t)$ (black symbols) of a $F8H16$ monolayer in a PFH-enriched atmosphere. The experiment was performed at a strain amplitude of $u_0 = 0.01$ and frequency of $f = 100\,\text{mHz}$. The black line is the fit with a Fourier series expansion up to the 5th mode. b) Phase shift between stress and strain for a $F8H16$ monolayer in air and in PFH-enriched atmosphere in dependence of the frequency.

7.2. Dilational Viscoelasticity

In a next step, the influence of PFH on the dilational viscoelastic behavior of $FnHm$ monolayers was studied. In Figure 7.5a, the change of the surface pressure of a $F8H16$ monolayer measured under oscillatory change in the area per molecule $A(t)$ in a PFH-enriched atmosphere at a strain frequency of $f = 100\,\text{mHz}$ and strain amplitude of $u_0 = 0.01$ is displayed. Equivalently to the situation in air (Section 5.2), the global shape of the response function $\pi(t)$ shows a distinct deviation from an ideal sinusoidal function, indicating that the viscoelastic response of the $F8H16$ monolayer is nonlinear. Thus, the response function was fitted by a Fourier series expansion up to the 5th mode. In the following, the linear contribution will be investigated first by analyzing only the first mode of the Fourier series expansion, the contribution of the higher modes are discussed afterwards.

As presented in Fig. 7.5b, the phase separation between stress and strain exhibits a minor increase from $\varphi \approx 0.2 - 0.6$ following the increase in the frequency from $f = 1 - 150\,\text{mHz}$. The results in air are presented with solid symbols, while the data points from the experiments in the PFH-enriched atmosphere are shown with open symbols.[2] The fact that the phase shift is below $\pi/2$, indicates that the $F8H16$ monolayer in the PFH-enriched atmosphere is predominantly elastic. In fact, the raw data as well as the behavior of the phase versus frequency are very similar to

[2] This representation was used throught this chapter: air data are shown with solid, dark symbols and the data of the PFH-enriched atmosphere in open symbols with brighter colors.

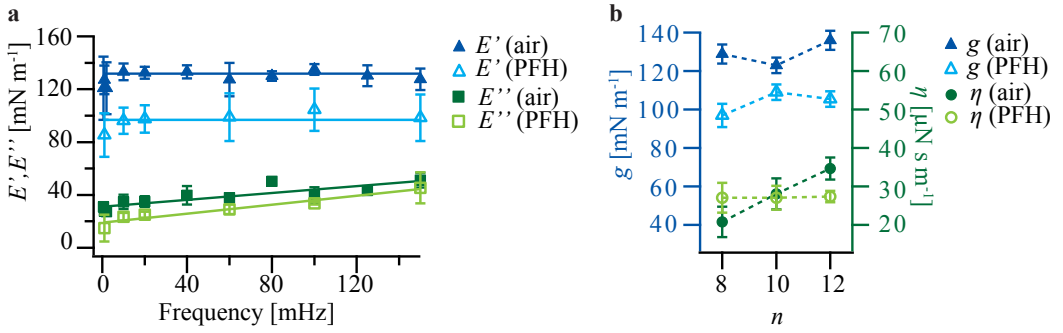

Figure 7.6.: **Dilational rheology of *FnH*16 monolayers in the PFH-enriched atmosphere.** a) Elastic modulus E_1' and viscous modulus E_1'' with respect to the frequency in air and in PFH-enriched atmosphere for a $F8H16$ monolayer. The lines correspond to the fits to the Kelvin-Voigt model. b) Spring constant g and interfacial viscosity η for the $FnH16$ molecules with respect to the fluorocarbon segment length in air and in PFH-enriched atmosphere. The lines are a guide to the eye.

what we measured in air.

Figure 7.5a shows the elastic and viscous modulus E_1' and E_1'' obtained from the first Fourier mode of $F8H16$ monolayers as a function of the strain frequency. Both E_1' and E_1'' exhibit the same tendency in the PFH-enriched atmosphere compared to air and were fitted with the Kelvin-Voigt model. The elastic modulus E_1' is almost independent from the frequency, yielding a spring constant that is about 25 % less compared to the corresponding value in air, ($g_{F8H16,\mathrm{PFH}} = (96.8 \pm 2.6)\,\mathrm{mN\,m^{-1}}$, $g_{F8H16,\mathrm{air}} = (128.8 \pm 1.4)\,\mathrm{mN\,m^{-1}}$). The viscous modulus E_1'' however increases linearly with the frequency in both situations and the 2D viscosity is slightly higher in the PFH-enriched atmosphere compared to air ($\eta_{F8H16,\mathrm{PFH}} = (27.1 \pm 3.8)\,\mathrm{\mu N\,s\,m^{-1}}$, $\eta_{F8H16,\mathrm{air}} = (20.8 \pm 3.9)\,\mathrm{\mu N\,s\,m^{-1}}$).

This principle Kelvin-Voigt-like behavior was observed for all the other $FnHm$ diblocks, too (Figure A.8). Therefore, the spring constant g and the interfacial viscosity η obtained from fitting to the Kelvin-Voigt model are used to study the influence of the fluorocarbon segment length n (Figure 7.5c). The spring constant in the PFH-enriched atmosphere is $\approx 25\,\%$ lower than in air and is in both situations independent from the fluorocarbon segment length. Whereas in air the elongation of the fluorocarbon segments from $n = 8$ to 10 leads to an increase in the interfacial viscosity, η is independent from the fluorocarbon segment length in the PFH-enriched atmosphere ($\eta_{FnH16,\mathrm{PFH}} \approx 27\,\mu\mathrm{N\,s\,m^{-1}}$), which suggests that the cohesion between the fluorocarbon segments is screened by the PFH molecules.

Since the π/A-isotherms measured in the PFH-enriched atmosphere showed higher

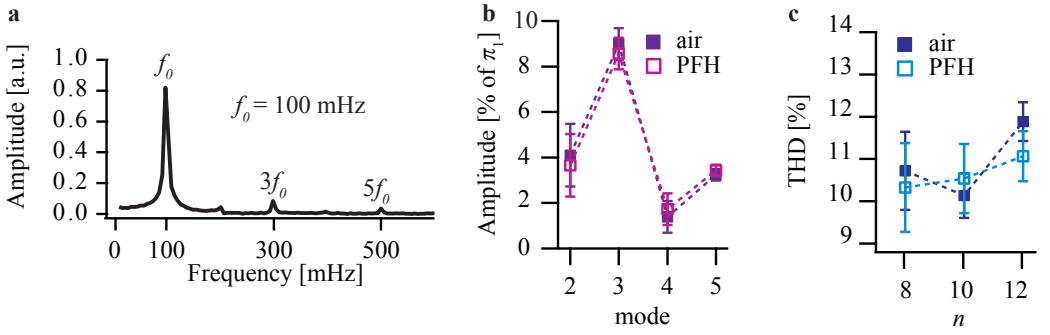

Figure 7.7.: **Nonlinear analysis of dilational rheology of *FnHm* monolayers in a PFH-enriched atmosphere.** a) Fourier spectrum of the response function of $F8H16$ recorded at $f = 100\,\text{mHz}$ in PFH-enriched atmosphere. b) Fractions of the k-th Fourier mode amplitude π_k with respect to the first mode π_1 averaged over the strain frequency f and plotted over the mode number for both situations in air and in the PFH-enriched atmosphere. c) THD values of the $FnH16$ diblocks as a function of the fluorocarbon segment length n in air and in the PFH-enriched atmosphere. The lines in b) and c) are given to guide the eye.

lateral compressibilites and PFH is known to adsorb at the air/water interface, the decrease in E_1' and g can be attributed to the increase in the lateral compressibility and to a decrease in inter-domain repulsions.

As presented extensively for the situation in air before, also in the PFH-enriched atmosphere a clear nonlinear surface pressure response was observed. Figure 7.7a shows the Fourier spectrum of $F8H16$ in the presence of PFH. As observed for the situation in air before, the first and third modes seem dominant. Since the amplitude of the k-th mode π_k normalized by the first Fourier mode π_1 is independent of the frequency, the normalized intensity averaged over the whole frequency regime was plotted as a function of the Fourier mode (Figure 7.7b). In air and in the PFH-enriched atmosphere, the normalized amplitudes are the same, the amplitude of the third mode is $\sim 9\,\%$ of the first mode. The second and fifth modes are $\sim 3\,\%$ of the first mode which is close to the noise level ($2\,\%$). Figure 7.7c shows the mean THD for every $FnH16$ diblock system averaged over the whole frequency regime for air and the PFH-enriched atmosphere. The values of the PFH-enriched atmosphere are almost identical to those in air and are independent of the fluorocarbon segment length. Obviously, the PFH-enriched atmosphere only affects the first mode of the Fourier spectrum but not the higher modes. PFH hence does not influence the nonlinear coupling between the surface micelles.

Interestingly, in the PFH-enriched atmosphere, an increase of the THD with the

hydrocarbon segment length was observed as well (Figure A.9). This effect could be attributed to the increase of the size of the surface micelles which may influence the ordering.

7.3. GISAXS

To obtain more information about the influence of PFH on the structure and correlation of the $FnHm$ domains, GISAXS measurements were performed in a PFH-enriched atmosphere and compared to the data measured in air which are presented in Section 6.2. Figure 7.8a shows the scattering signal of a $F8H16$ monolayer in the PFH-enriched atmosphere at a surface pressure of $\pi = 5\,\mathrm{mN\,m^{-1}}$, presented in a 2D reciprocal space coordinate system. Figure 7.8b shows the respective intensity profile along q_y including the fitted intensity, the form factor $|F(q)|^2$ and the structure factor $S(q)$. For the $FnHm$ surface micelles in the PFH-enriched atmosphere the same model was used as for the analysis of the GISAXS data in air (cf. Section 6.2.1). The fact that the best fit could well represent the experimental data implies that the PFH molecules do not cause a coalescence or deformation of the $FnHm$ domains.

Figure 7.8c shows the diameter D obtained from the fitting, as a function of the fluorocarbon segment length n in air and in the PFH-enriched atmosphere. An overview of all data obtained from GISAXS in air and in the PFH-enriched atmosphere is given in Table A.1. In the PFH-enriched atmosphere, the mean diameter of the $FnH16$ domains increases with fluorocarbon segment length from $D_{F8H16,\mathrm{PFH}} = (29.4 \pm 0.6)\,\mathrm{nm}$ to $D_{F12H16,\mathrm{PFH}} = (32.1 \pm 0.6)\,\mathrm{nm}$. The respective parameters in air are only slightly higher. The lattice parameter L obtained from the structure factor was comparable to the corresponding diameter of each system (e.g. $L_{F8H16,\mathrm{PFH}} = (28.6 \pm 5.2)\,\mathrm{nm}$), indicating that the $FnHm$ domains form tightly packed hexagonal lattices.

The data show further that the correlation length ξ increases monotonically from $\xi_{F8H16} = 300\,\mathrm{nm}$ to $\xi_{F12H16} = 750\,\mathrm{nm}$ with the fluorocarbon segment length. The inter-domain correlation between the $FnH16$ domains hence reaches a distance that is $12 - 18$ times longer than the distance of the nearest neighbors. In air, a similar long-range correlation length was reported and could be attributed to the strong dipole repulsions induced by the CF_3 termini and the $CF_2 - CH_2$ bond (Section 6.2).

It can be concluded that the PFH domains only barely influence the shape, size and correlation of the $FnH16$ domains in the static experimental setup of the GISAXS measurements. The intercalation of the PFH molecules into the $FnHm$ domains

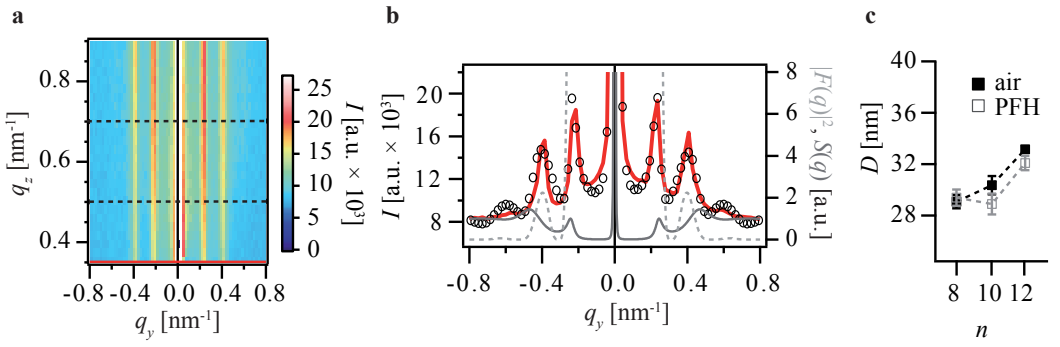

Figure 7.8.: **GISAXS of *FnHm* monolayers in a PFH-enriched atmosphere.** a) GISAXS signal from a $F8H16$ monolayer in a PFH-enriched atmosphere measured at $\pi = 5\,\mathrm{mN\,m^{-1}}$, plotted in 2D reciprocal coordinates. b) Intensity profile along q_y, integrated between $q_z = 1.0$ and $1.2\,\mathrm{nm^{-1}}$, indicated by the two dashed lines in panel a). The red line represents the fitted intensity, including the structure factor (solid gray line) and the form factor (dashed gray line). c) Calculated diameter D of $FnH16$ domains in air and in a PFH-enriched atmosphere plotted as a function of the fluorocarbon segment length n. The lines are given to guide the eye.

as it was hypothesized in the beginning (Figure 7.3a) is therefore not likely as this would result in a swelling of the domains. The second scenario (Figure 7.3b) is hence more plausible: PFH molecule adsorb to the air/water interface and form a thin layer between the domains. Actually, as presented in Figure 7.2a, the difference between the area per molecule of $F8H16$ at $\pi = 5\,\mathrm{mN\,m^{-1}}$ in the PFH-enriched atmosphere is very minor ($A_{F8H16,\mathrm{air}} = 30.9\,\mathrm{Å}^2$, $A_{F8H16,\mathrm{PFH}} = 30.3\,\mathrm{Å}^2$). This seems to agree well with the GISAXS data showing no major differences between air and the PFH-enriched atmosphere.

However a strong increase of the compressibility and a decrease of the elasticity of the monolayers were observed. This strongly suggests that the PFH molecules adsorb to the free space between the surface micelles and decrease the repulsions between the nanodomains which hence results in a decreased elastic response. On the other hand, the interfacial viscosity is not influenced by the PFH molecules. As PFH is extremely hydrophobic, it seems plausible that is has no effect on the friction between the monolayer and the water. The data show that in the presence of PFH, η is independent of the fluorocarbon segment length. This suggests that the PFH molecules between the domains slightly affect the inter-domain frictional forces.

8. Influence of Lipids on Monolayers of Semifluorinated Alkanes at the Air/Water Interface

So far, commercial microbubbles used for ultrasound diagnostics are mostly composed of a lipid or polymer shell.[55] The main disadvantage of these microbubbles is the limited life time which is often too short for the medical applications.[55] An interesting strategy to stabilize such microbubbles would be to incorporate semifluorinated alkanes into the shell. These are promising candidates due to their extreme hydrophobicity and the elastic behavior. Indeed, it was shown that semifluorinated alkanes stabilize phospholipid vesicles[22,95] as well as fluorocarbon-in-water emulsions.[7] A promising candidate would be a mixture of $F8H16$ and lipid DPPC[1] since it has its transition temperature at $T_m = 41°C$ and remains in the fluid phase in the human body. Both $F8H16$ and DPPC have hydrocarbon chains composed of 16 carbon atoms. So far, it is unclear, how the lipids and the semifluorinated alkanes mix on the microscopic scale and how they order in the microbubble's shell.

A first, straightforward attempt to study the physical interactions between semifluorinated alkanes and DPPC is the study of mixed monolayers. Maaloum et al. studied π/A-isotherms of mixed monolayers of the lipid DPPE[2] and $F8H16$ diblocks.[66] In contrast to DPPC, DPPE is in the gel phase throughout the compression. The effect of $F8H16$ on lipids in fluid phase is completely unclear. Interestingly, it was found that the short semifluorinated alkane $F8H2$ has a fluidizing effect on DPPC monolayers.[29] Gerber et al. found that a nitrogen atmosphere enriched with $F8H2$ prevents the formation of the LC phase of DPPC upon compression.[29]

In this chapter, monolayers of 1:1 mixtures of $F8H16$ and DPPC are investigated with respect to their physical properties. By performing π/A-isotherms, the phase behavior of the monolayer during compression was studied and compared to the pure

[1] cf. Section 3.1.2 and Figure 3.1a

[2] 1,2-Dipalmitoyl-sn-glycero-3-phosphoethanolamine, PE headgroup with 2 saturated hydrocarbon chains with 16 carbons

monolayers (Section 8.1). In a next step, the phase transition was further studied by doping the monolayer with lipids possessing a fluorescent die which allows to visualize the LE/LC phase transition by fluorescent microscopy (Section 8.2). Finally, in Section 8.3 the dilational viscoelastic properties of the monolayer at small surface pressures are presented.

8.1. π/A-Isotherms

Figure 8.1 displays π/A-isotherms of a $F8H16$/DPPC monolayer and a pure DPPC monolayer recorded at $T = 20°C$. The π/A-isotherms were recorded according to Section 3.2.1. The π/A-isotherm of the pure $F8H16$ monolayer is shown in Section 4.1 (Figure 4.1). The π/A-isotherm of pure DPPC is comparable to π/A-isotherms published, the principle behavior was already extensively described in Section 2.1:[1,63] Coming from large molecular areas, the surface pressure increases at $A_{\mathrm{DPPC}} \approx 90\,\text{Å}^2$. At the molecular area of $\sim 74\,\text{Å}^2$, π follows a plateau region which indicates the LE/LC phase transition. At a molecular area of $\sim 49\,\text{Å}^2$, the π/A-isotherm shows a steep increase of the surface pressure indicating that the whole monolayer has transitioned into the LC phase.

The π/A-isotherm of the mixed $F8H16$/DPPC monolayer shows a more complex behavior. The onset of the surface pressure increase occurs at $A_{F8H16/\mathrm{DPPC}} \approx 52\,\text{Å}^2$. At $\pi = 5 - 8\,\mathrm{mN\,m^{-1}}$ a plateau was observed which is followed by a steep increase of π. A further kink in the isotherm is observed at $\pi \approx 17\,\mathrm{mN\,m^{-1}}$ and $A \approx 26\,\text{Å}^2$.

Due to the lipophobic nature of the semifluorinated alkanes, one can assume that the lipids will not mix with the $F8H16$ on a molecular level and it can be suggested that the ordering of the $F8H16$ molecules into surface micelles stays intact. It is more likely that the mixed monolayer consists of $F8H16$ surface micelles which are incorporated into the smooth DPPC monolayer.

The theoretical, ideal average area per molecule of the mixed monolayer at a certain surface pressure is[42]

$$A_{\mathrm{ideal}} = x_1 A_1 + (1 - x_1) A_2, \tag{8.1}$$

assuming that there are no specific interactions between the two components. A_1 and A_2 are the areas per molecules of the pure monolayers and x_1 is the mole fraction of the component 1. In the case of the mixed $F8H16$/DPPC monolayer, one would hence expect the onset of the surface pressure increase to occur at $A_{\mathrm{ideal}} \approx 62\,\text{Å}^2$. Interestingly, the molecular area of the onset of the surface pressure $A_{F8H16/\mathrm{DPPC}} \approx$

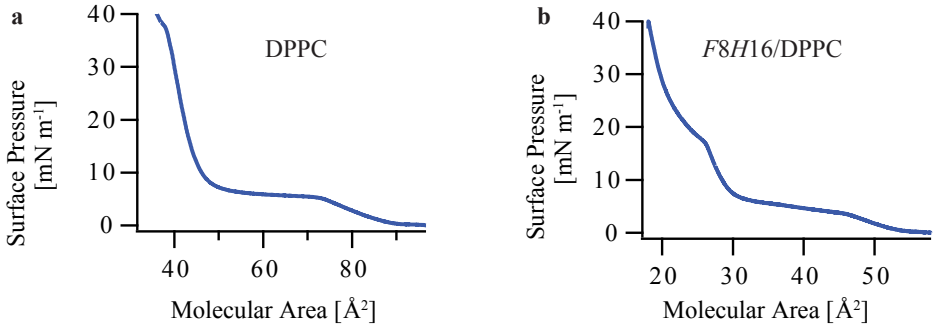

Figure 8.1.: **π/A-Isotherms of a DPPC monolayer (a) and a 1:1 mixed $F8H16$/DPPC monolayer (b).** The compression speed was $3.75\text{cm}^2\,\text{min}^{-1}$ and the π/A-isotherms were recorded at $T = 20°\text{C}$

$52\,\text{Å}^2$ is distinctly smaller than what is expected for an ideal mixing. The fact that $A_{\text{ideal}} > A_{\text{measured}}$ indicates that there are (small) attractive interactions between the two components.[42] This scenario underlines the picture presented previously that the $F8H16$ surface micelles are surrounded by the lipids which screen the repulsive dipole interactions between them. This means that the repulsive forces between the dipoles of the $F8H16$ are stronger than the repulsive forces between the $F8H16$ surface micelles and the DPPC molecules originating from the lipophobicity of the fluorocarbon chains.

The plateau region in the π/A-isotherm occurs at a similar surface pressure for both cases. In the pure DPPC isotherm it can be attributed to the LE/LC transition. Therefore, in the case of the mixed monolayer it probably also results from the phase transition of the lipids. However this assumption requires further assessments. In contrast to the pure DPPC monolayer, an additional transition was observed at $\pi \approx 17\,\text{mN}\,\text{m}^{-1}$ in the π/A-isotherms of the mixed $F8H16$/DPPC monolayer of which the origin is unclear. One possible hypothesis is that the $F8H16$ surface micelles start to form a second layer on top of the DPPC lipids in LC phase. Such a behavior was observed for pure $F8H16$ monolayers at $\pi_c \approx 12\,\text{mN}\,\text{m}^{-1}$.

Indeed, π/A-isotherms were performed on mixed monolayers composed of $F8H16$ and the lipid DPPE.[50,66] Analogous to DPPC, DPPE possesses two hydrocarbon chains of the length of 16 carbon atoms which are attached to a Phosphatidylethanolamine (PE) headgroup. Due to the stronger attractive forces of the PE headgroups compared to the PC headgroups, DPPE directly performs a transition from G to LC phase upon compression at 20°C. They observed a phase transition of the mixed $F8H16$/DPPE monolayer at $\pi \approx 12\,\text{mN}\,\text{m}^{-1}$ which was indicated by a drastic de-

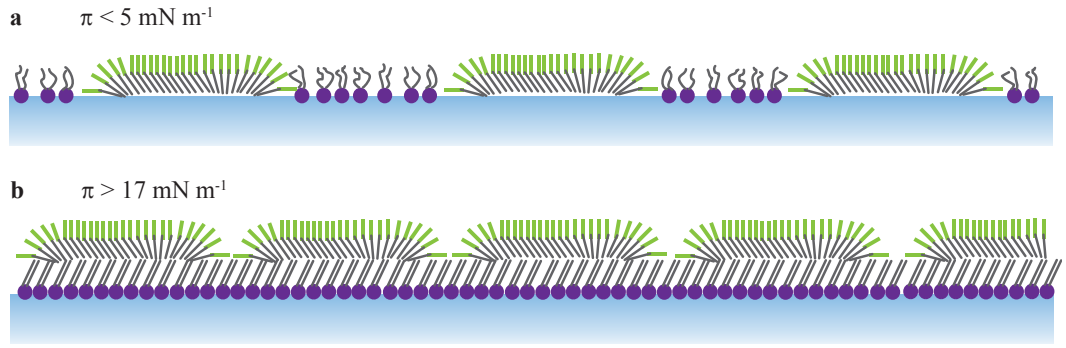

Figure 8.2.: **Schematic illustrations of mixed *F*8*H*16/DPPC monolayers** at $\pi < 5\,\mathrm{mN\,m^{-1}}$ (a) and $\pi > 17\,\mathrm{mN\,m^{-1}}$ (b). These two scenarios are assumptions based on the measurements presented here and measurements from Maaloum et al. The illustrations are not in scale but only show the schematic idea of the ordering of the surface micelles with the lipids.[66]

crease of the slope of the surface pressure.[66] They could attribute this to a 2D/3D phase transition where the hydrophobic $F8H16$ domains form a second layer on top of the DPPE monolayer. This was confirmed by imaging solid-supported films transferred via Langmuir Blodgett with AFM and by GIXD measurements.[50,66] However, in the case presented here the kink at $\pi \approx 17\,\mathrm{mN\,m^{-1}}$ is followed by a further steep increase in π. We would expect a plateau with constant π such as it was measured for the 2D/3D transition of the semifluorinated alkane surface micelles. Further measurements are hence necessary to find the origin of this phase transition.

Concluding from the π/A-isotherms a scenario such as it is shown in Figure 8.2 can be assumed. For low surface pressures $\pi < 5\,\mathrm{mN\,m^{-1}}$ the DPPC molecules are in the LE phase and homogeneously distributed with the $F8H16$ surface micelles (Figure 8.2a). At high surface pressures $\pi > 17\,\mathrm{mN\,m^{-1}}$ a possible setup as proposed by Maaloum et al. is the formation of a monolayer of $F8H16$ surface micelles on top of the DPPC layer in LC phase (Figure 8.2b) It is still unclear what happens in the region between $\pi = 5\,\mathrm{mN\,m^{-1}}$ and $17\,\mathrm{mN\,m^{-1}}$.

8.2. Fluorescence Microscopy

To shed more light on the ordering of the lipids and the $F8H16$ surface micelles in the region $5\,\mathrm{mN\,m^{-1}} < \pi < 17\,\mathrm{mN\,m^{-1}}$, fluorescent microscopy was used, a technique often applied to study lipid phase transitions of monolayers at the air/water interface.[36,46,71] 0.1 mol % of the lipid DHPE which had the fluorescent marker Texas Red attached to its head group was added to the DPPC solution. The ex-

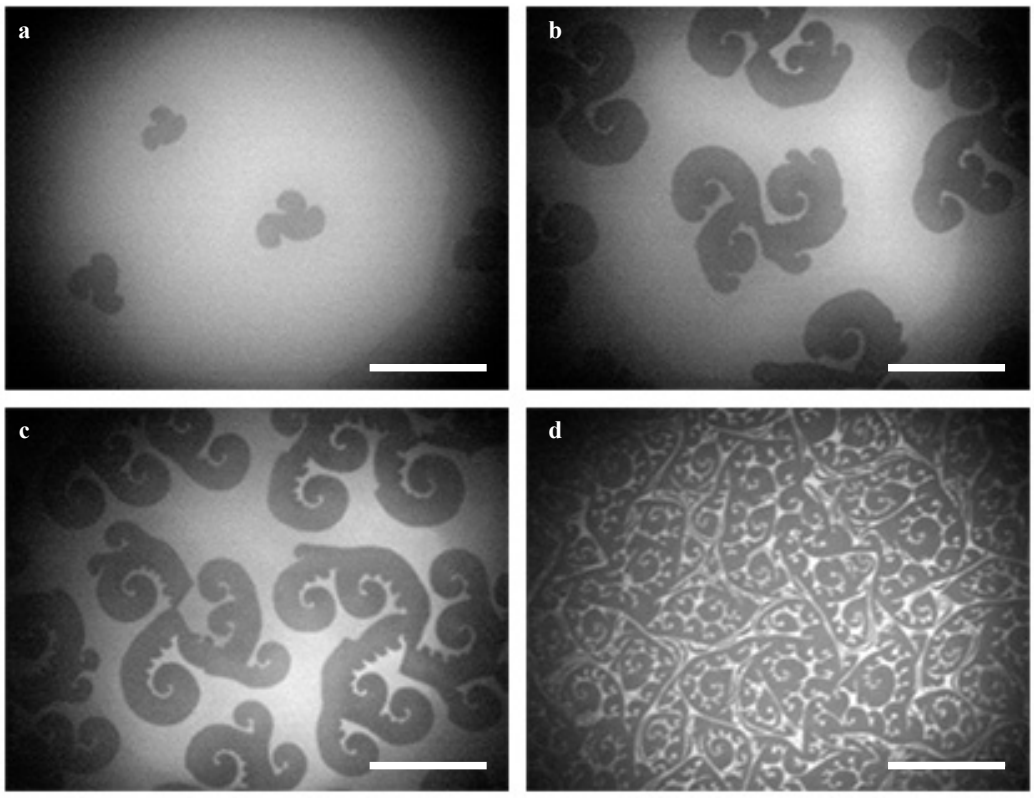

Figure 8.3.: **Fluorescence microscopy images of a DPPC monolayer.** 0.1 mol % of fluorescent DHPE-Texas Red was added to the DPPC solution. The images were recorded at a) 5.1mN m^{-1}, b) 6.0 mN m^{-1}, c) 6.8 mN m^{-1} and d) 7.7 mN m^{-1}. The compression speed was 3 cm^2 min^{-1}. The scale bar is 50 μm.

act experimental procedure is described in Section 3.2.5. During the compression of the monolayer, the fluorescent signal was constantly recorded using a fluorescent microscope that was positioned under the film balance which was equipped with a window. Doping the DPPC monolayer with DHPE-Texas Red allowed to visualize the LE/LC phase transition at $\pi \approx 5 - 8$mN m^{-1} which is shown in Figure 8.3. As the DHPE molecules are excluded from the LC phase of DPPC, the bright regions correspond to the LE phase whereas the dark regions correspond to the LC phase. Indeed, the fluorescent images confirm the published results:[71] At surface pressures below $\pi = 5$ mN m^{-1}, no dark spots could be observed. Once the dark domains, indicating the LC phase, form, the domains grow constantly under compression and form characteristic shapes. The first LC domains observed by the fluorescent microscopy have bean-like shapes which were found to be the most stable shapes for

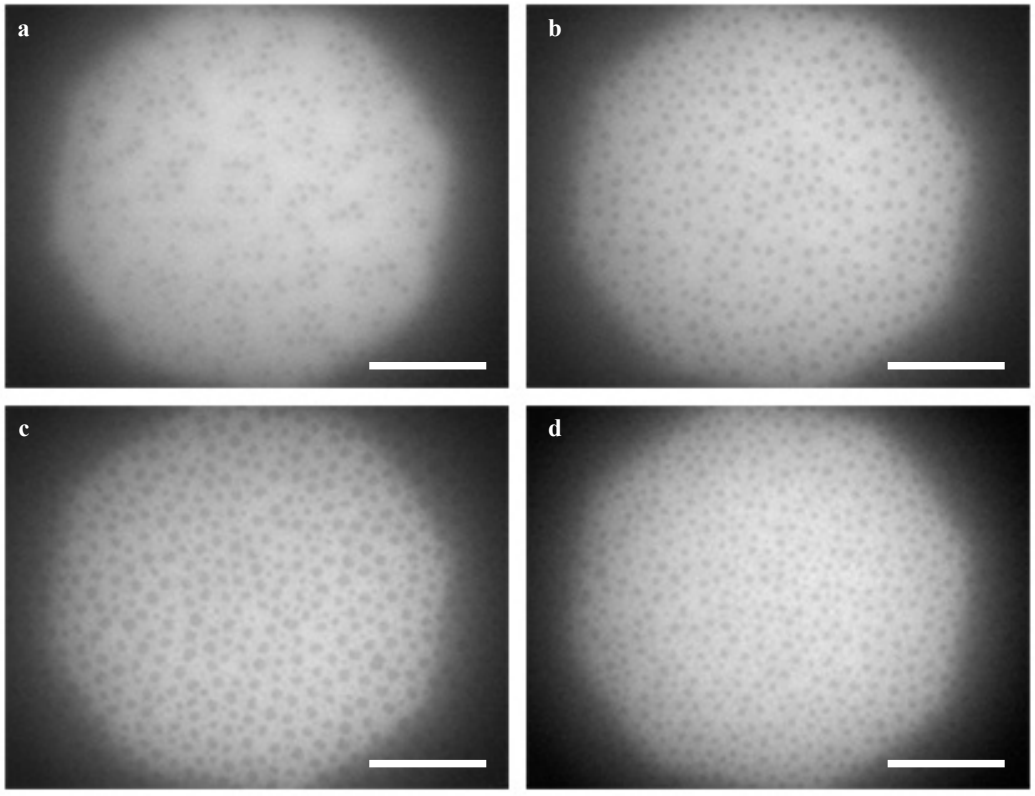

Figure 8.4.: **Fluorescence microscopy images of a *F*8*H*16/DPPC monolayer.** 0.1 mol % fluorescent DHPE-Texas Red was added to the $F8H16$/DPPC solution. The images were recorded at a) $5.4\,\mathrm{mN\,m^{-1}}$, b) $6.0\,\mathrm{mN\,m^{-1}}$, c) $6.8\,\mathrm{mN\,m^{-1}}$ and d) $7.7\,\mathrm{mN\,m^{-1}}$. The compression speed was $3\,\mathrm{cm^2\,min^{-1}}$. The scale bar is $50\,\mu\mathrm{m}$.

the DPPC lipids in LC phase.[71] After the further compression to smaller molecular areas the beans transform into multilobed domains which occur especially at compression rates $\geq 15\,\mathrm{\AA^2\,min^{-1}}$.[71] At molecular areas $A < 50\,\mathrm{\AA^2}$ ($\pi > 8\,\mathrm{mN\,m^{-1}}$), the LC domains finally merge and form a closed monolayer with all lipids being in the LC phase and no more fluorescent signal could be measured. The appearance of the multilobed domains was actually predicted theoretically using an energy model which is based on the line tension and the intermolecular dipole forces.[74]

Analogous experiments were performed for the mixed $F8H16$/DPPC monolayer. Interestingly, fluorescent signals were observed in the same surface pressure regime as for the pure DPPC monolayer. Figure 8.4 shows 4 fluorescent images at the same surface pressures between $\pi = 5.4\,\mathrm{mN\,m^{-1}}$ and $7.7\,\mathrm{mN\,m^{-1}}$. First dark spots

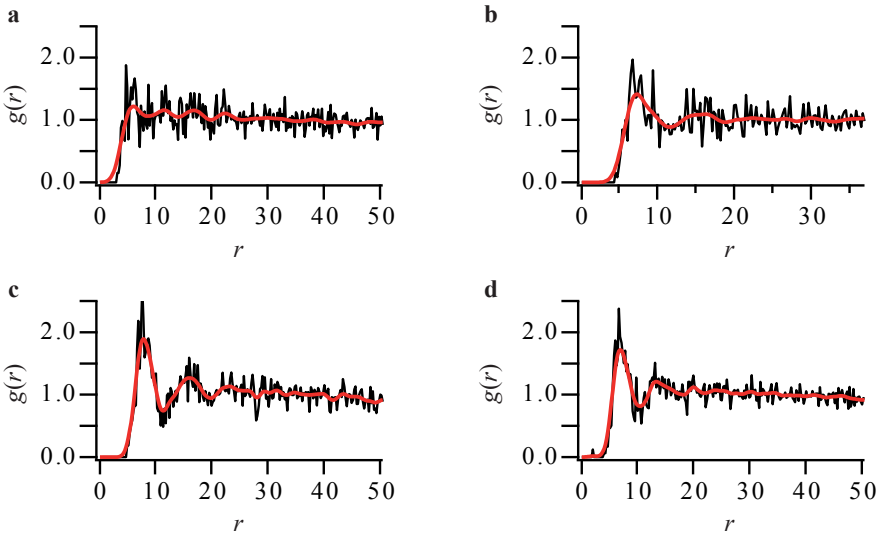

Figure 8.5.: **Radial distribution function $g(r)$ calculated from the images in Figure 8.4a-d respectively.** The red lines show the data smoothed by Gaussian filters over 10 points.

indicating the begin of the phase coexistence phase were observed at $\pi \approx 5\,\mathrm{mN\,m^{-1}}$ ($A \approx 47\,\mathrm{\AA}^2$). Upon compression, the number of the dark spots increased until they fully covered the available area and no more fluorescent signal was measured at $\pi > 8\,\mathrm{mN\,m^{-1}}$. The dark spots have a size of $3.5 - 6\,\mu\mathrm{m}$ which does not change during the compression.

Figure 8.5 shows the radial distribution functions $g(r)$ calculated from the images in Figure 8.4. The exact procedure is described in Section 3.2.5. In the first image, Figure 8.4a at $\pi = 5.4\,\mathrm{mN\,m^{-1}}$, the dark spots are rather disordered and hence $g(r)$ does not show a strong correlation between the spots. The correlation between the dark spots increases with the increase of the surface pressure as indicated by a strong first peak and the appearance of more peaks. Whereas at $\pi = 5.4\,\mathrm{mN\,m^{-1}}$, $g(r)$ shows the typical behavior of a liquid, at the higher surface pressures $g(r)$ rather shows a behavior of a solid material.

In case of the mixed $F8H16$/DPPC monolayer, it is not straightforward to predict in which phase the Texas Red marked DHPE lipids stay within the monolayer. It is highly unlikely that DHPE will merge into the $F8H16$ surface micelles due to the lipophobic nature of the fluorocarbon chains. It is more probable that DHPE will behave same as in the pure DPPC monolayer and mix with the DPPC lipids in the LE phase. We can therefore attribute the dark spots in Figure 8.4 to regions composed of $F8H16$ surface micelles and DPPC in the LC phase. The fact that the shape of the

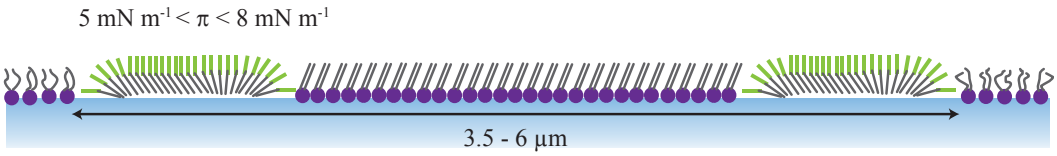

Figure 8.6.: **Schematic illustrations of mixed *F8H16*/DPPC monolayers in the phase transition region** $5\,\mathrm{mN\,m^{-1}} < \pi < 8\,\mathrm{mN\,m^{-1}}$**.** This hypothetical scenario is based on the fluorescence microscopy measurements. The domains of DPPC lipids in LC phase surrounded by the *FnHm* surface micelles is $3.5 - 6\,\mu$m, the graph is hence not in scale but shows the schematic idea of the situation.

radial distribution function $g(r)$ shows a more liquid like behavior at the beginning of the LC/LE transition and transforms into a higher correlated solid-like pattern for the higher surface pressures further confirms this suggestion (Figure 8.5). In contrast to the pure DPPC monolayer, the dark spots do not grow in size during compression. This strongly suggests that they correspond to DPPC lipids in the LC phase that are surrounded by *F8H16* surface micelles. This is schematically illustrated in Figure 8.6. It is likely that the *F8H16* surface micelles will assemble at the phase boundary regions between the DPPC LE and LC phase. Here they will reduce the line tension of the lipid LC domains in order to minimize the free energy of the system. This is a behavior similar to other multiphase systems that contain impurities. Actually, it was already predicted 1957 by McLean that impurities accumulate to phase boundary regions[75] which was later observed experimentally.[31,40] The accumulation of the *F8H16* surface micelles at the phase boundary would hinder a growth of the LC domains by reducing the line tension. Although these domains composed of DPPC in LC phase surrounded by *F8H16* surface micelles do not grow in size, they grow in number during the further compression of the monolayer. Actually, a similar effect was observed when compressing a DPPC monolayer in an atmosphere enriched with *F8H2*.[29] The *F8H2* molecules led to a decreased size of the LC domains which in that case even led to a complete fluidization of the DPPC monolayer which was in the LE phase during the complete isothermal compression.[29]

The phase transition of the mixed *F8H16*/DPPC monolayer observed with the fluorescent marked DHPE occurs at the same surface pressure as the LE/LC phase transition of the pure DPPC monolayer. This further suggests that the phase transition which was observed in the mixed monolayer can be attributed to DPPC which undergoes the LE/LC phase transition independent of the presence of *F8H16* at $\pi \approx 5 - 8\,\mathrm{mN\,m^{-1}}$. The plateau region in the pure DPPC monolayer how-

ever is broader and covers a molecular area of $\Delta A_{\mathrm{DPPC}} \approx 23\,\text{Å}^2$ compared to $\Delta A_{F8H16/\mathrm{DPPC}} \approx 8\,\text{Å}^2$.

8.3. Dilational Rheology

Dilational rheology experiments of mixed $F8H16$/DPPC monolayers were performed at $\pi_0 = 4\,\mathrm{mN\,m^{-1}}$. The experimental procedure is described in Section 3.2.3. Two different oscillation amplitudes $u_0 = 0.02$ and $u_0 = 0.05$ were investigated. Reducing the strain amplitude to $u_0 = 0.01$ which was used for the previous experiments, was not possible due to the low amplitude π_1 of the surface pressure response which was close to the resolution limit. Due to the comparable high oscillating amplitude, the measurable frequency regime was restricted to $1 - 75\,\mathrm{mHz}$. Figure 8.7 shows exemplarily the oscillation of the molecular area and the resulting surface pressure response for a DPPC monolayer (a) and a mixed $F8H16$/DPPC monolayer (b) at $f = 10\,\mathrm{mHz}$, $u_0 = 0.05$ and $\pi_0 = 4\,\mathrm{mN\,m^{-1}}$. The shape of the oscillation of the surface pressure again reveals a small nonlinearity in the response signal. The data were hence fitted by a Fourier series expansion and in the following the data obtained from the first mode are presented first, whereas the higher modes and the origin of the nonlinearity are discussed at the end of the section. Figure 8.7 also reveals that the phase separation between stress and strain is extremely small for both monolayers ($\varphi \approx 0.15$), indicating a predominantly elastic response (Figure A.11).

At higher surface pressures $\pi_0 > 7\,\mathrm{mN\,m^{-1}}$, the mixed $F8H16$/DPPC monolayer was unstable during the expansion/compression cycles which was indicated by a decreasing surface pressure throughout the measurement (Figure A.10). Such a decrease of π over time can have several reasons such as a loss of material to the subphase, a strong reordering of the monolayer or a formation of an additional layer on top of the monolayer (2D/3D transition). As the analysis of such unstable signals is extremely difficult and especially not meaningful, $\pi_0 = 4\,\mathrm{mN\,m^{-1}}$ was chosen since here DPPC should still be in the LE phase.

Figure 8.8a shows the dilational elastic modulus E_1' and the dilational viscous modulus E_1'' of a pure DPPC monolayer versus the frequency ($u_0 = 0.05$ and $\pi_0 = 4\,\mathrm{mN\,m^{-1}}$). As expected from the low phase shift, the monolayer shows a predominantly elastic response with $E_1' > E_1''$. Both, E_1' and E_1'' are independent of the frequency in the regime measured with $E_1' \approx 24\,\mathrm{mN\,m^{-1}}$ and $E_1'' \approx 0.6\,\mathrm{mN\,m^{-1}}$. These values are indeed comparable to the data published previously.[63,106] The low elastic moduli could be attributed to the low physical interactions between the lipids

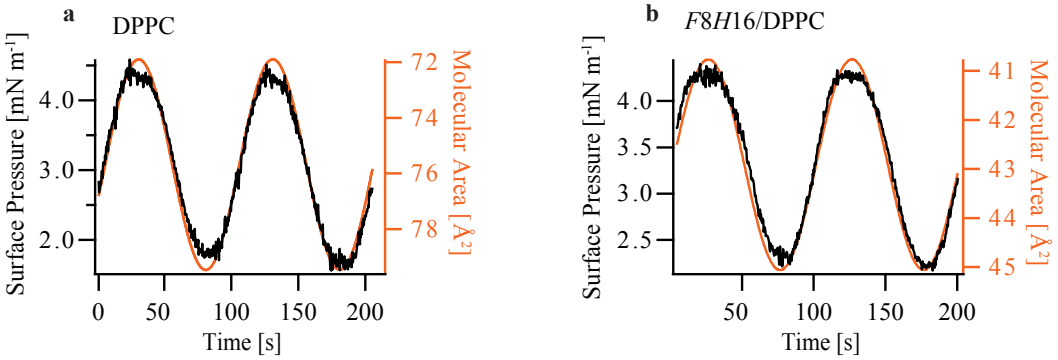

Figure 8.7.: **Surface pressure response $\pi(t)$ of a DPPC (a) and a $F8H16$/DPPC monolayer (b) versus time.** The strain frequency was $f = 10\,\mathrm{mHz}$, amplitude $u_0 = 0.05$ and $\pi_0 = 4\,\mathrm{mN\,m}$. The oscillation of the molecular area is marked in red, the response of the surface pressure is marked in black.

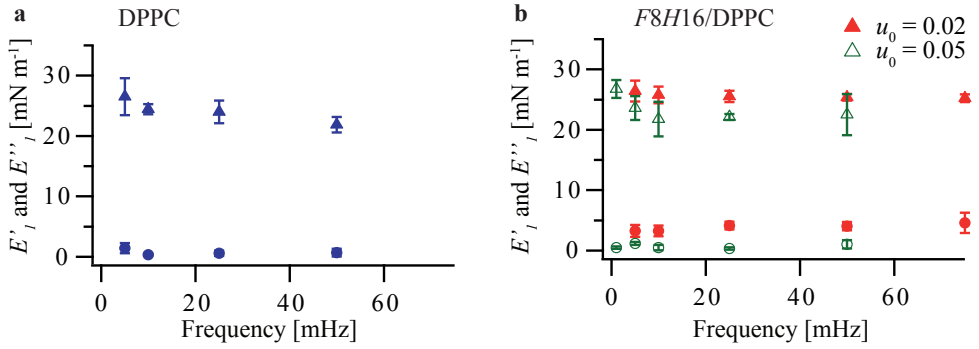

Figure 8.8.: **Dilational viscoelasticity of $F8H16$/DPPC and DPPC monolayers.** a) Elastic and viscous moduli E_1' (circle) and E_1'' (triangle) for a pure DPPC monolayer with $u_0 = 0.05$ with respect to the frequency. b) Elastic and viscous moduli E_1' (circle) and E_1'' (triangle) with respect to the frequency for $F8H16$/DPPC monolayers for the two strain amplitudes $u_0 = 0.02$ and $u_0 = 0.05$.

in the LE phase.[63] Actually the measurements were performed in close proximity to the region of LE/LC phase transition which is characterized by the presence of a plateau in the π/A-isotherm and would hence result in $\pi_1 \approx 0\,\mathrm{mN\,m^{-1}}$ and $E_1' = 0\,\mathrm{mN\,m^{-1}}$.

The dilational elastic and viscous moduli E_1' and E_1'' of the mixed $F8H16$/DPPC monolayer are shown in Figure 8.8b for both strain amplitudes, $u_0 = 0.02$ and $u_0 = 0.05$. In the frequency regime measured, the monolayer behaves predominantly elastic as well. E_1' and E_1'' are mostly independent of the frequency. Interestingly, both E_1' and E_1'' are $\sim 10\,\%$ lower for the higher oscillation amplitude which can be attributed to the higher compressibility of the monolayer at the higher surface pressures close to the LE/LC transition.

Compared to the pure $F8H16$ monolayer, the elastic modulus of the system is strongly reduced. This suggests that the DPPC molecules and the $F8H16$ surface micelles are homogeneously distributed and DPPC acts as a damper system to the elastic $F8H16$ monolayer. This is the scenario depicted in Figure 8.2a. As elaborated in Chapter 5, the strong elastic response of the semifluorinated alkane monolayers can be attributed to the highly repulsive interaction between the surface micelles. In the case of the mixed $F8H16$/DPPC monolayer, the DPPC molecules between the $F8H16$ surface micelles screen this repulsion, resulting in lower elastic moduli.

Surprisingly, the average elastic and viscous modulus of the mixed $F8H16$/DPPC monolayer over the whole frequency regime is the same as for the pure DPPC monolayer, $E_1' \approx 24\,\mathrm{mN\,m^{-1}}$ and $E_1'' \approx 0.7\,\mathrm{mN\,m^{-1}}$. The presence of $F8H16$ hence does not alter the elasticity and viscosity of the DPPC monolayer in the measured frequency and amplitude regime and the viscoelastic behavior of the mixed $F8H16$/DPPC monolayer is dominated by the mechanics of the pure DPPC monolayer.

In the next step, the nonlinearity of the response function was assessed. For the mixed $F8H16$/DPPC monolayer at the amplitude $u_0 = 0.02$, the Fourier spectra indicate a behavior similar to the one observed for the pure semifluorinated alkane monolayers: In addition to the first mode, a signal at the third mode is visible (Figure A.12). In order to get a better understanding of the contributions of the higher Fourier modes, the ratios of the higher modes compared to the first mode π_k/π_1 are plotted versus the frequency in Figure 8.9a. The higher mode amplitudes are independent of the frequency. The third mode shows the highest contribution ($\pi_3/\pi_1 \approx 0.05$). The contributions of the other modes are within the resolution limit of the system and can hence be neglected.

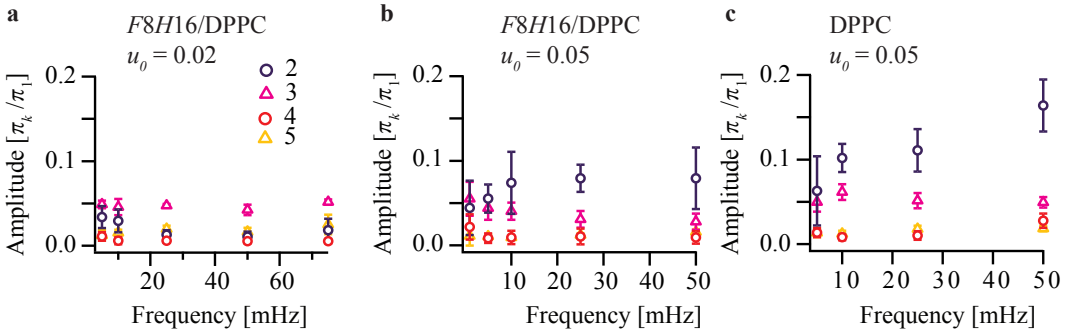

Figure 8.9.: **Fractions of the higher mode amplitudes π_k with respect to the first mode amplitude π_1 as a function of the frequency for the monolayers *F8H16*/DPPC.** The strain amplitude was $u_0 = 0.02$ (a) and $u_0 = 0.05$. (c) π_k/π_1 of a pure DPPC monolayer at $u_0 = 0.05$.

	F8H16/DPPC $u_0 = 0.02$	*F8H16*/DPPC $u_0 = 0.05$	DPPC $u_0 = 0.05$	*F8H16* $u_0 = 0.01$
THD	$(5.8 \pm 0.6)\,\%$	$(8.2 \pm 0.6)\,\%$	$(12.5 \pm 3.8)\,\%$	$(10.7 \pm 0.9)\,\%$

Table 8.1.: THD values averaged over the measured frequency regime of a *F8H16*/DPPC monolayer at $u_0 = 0.02$ and $u_0 = 0.05$, a pure DPPC monolayer at $u_0 = 0.05$ and a pure *F8H16* monolayer at $u_0 = 0.01$.

This behavior is different compared to the behavior at the amplitude $u_0 = 0.05$ (Figure 8.9b). Here, the second mode has the highest contribution with $\pi_2/\pi_1 \approx 0.07$ and slightly increases with the frequency. The second highest contribution of the Fourier modes has the third mode, with $\pi_3/\pi_1 \approx 0.05$, slightly decreasing with the frequency. The higher modes are within the noise level.

The pure DPPC monolayer shows a nonlinear behavior similar to the mixed *F8H16*/DPPC monolayer at the amplitude $u_0 = 0.05$ (Figure 8.9c): The second Fourier mode has the highest contribution which increases with frequency from $\pi_2/\pi_{1,5\,\mathrm{mHz}} = (0.06 \pm 0.04)$ to $\pi_2/\pi_{1,50\,\mathrm{mHz}} = (0.16 \pm 0.03)$. The third mode on the other hand remains almost constant over the measured frequency regime with $\pi_3/\pi_1 \approx 0.05$.

As expected, the nonlinear contribution hence increases with strain amplitude as reflected by the THD values which are lower for the smaller oscillation amplitude (Table 8.1). As the THD does not change with frequency it was averaged over the whole frequency regime. The THD of the pure DPPC monolayer is in the same range as the THD of the pure *F8H16* monolayer. However, we have to keep in mind that for the *F8H16* monolayer, a lower amplitude was used ($u_0 = 0.01$). At similar high

amplitudes, the nonlinearity of the pure $F8H16$ monolayer would hence probably be higher than the nonlinearity of the pure DPPC monolayer. Interestingly the mixed $F8H16$/DPPC has the lowest nonlinear contribution in the response signal, independent from the applied amplitude.

For all three systems containing DPPC and for all strain amplitudes measured, the nonlinear contribution of the third mode is the same ($\pi_3/\pi_1 \approx 0.05$) which is lower than the contribution of the third mode for the pure $F8H16$ monolayer ($\pi_3/\pi_1 \approx 0.09$, see Section 5.2). The nonlinearity of the pure $F8H16$ monolayer results mainly from the elastic part of the system and could be attributed to the phase transition of the surface micelles. As the elastic response of the mixed $F8H16$/DPPC monolayer and the pure DPPC monolayer is lower, it is not surprising that also the nonlinearity of the elastic part of the system (which is mainly described by the third mode) is reduced.

For the higher strain amplitude, an emergence of the second Fourier mode was observed which increases with frequency. This can be attributed to an increased nonlinear viscous contribution. As elaborated in Section 2.3.5, both, the existence of increased even modes as well as the frequency-dependency of the higher Fourier modes are indicators for nonlinear viscous stress responses. Interestingly, in contrast to the higher Fourier modes, the linear part of the viscous response (E_1'') seems independent of the strain amplitude.

Previous studies also showed a nonlinear response in the pure DPPC monolayers which was not further discussed and interpreted.[33,63] As the measurements were performed close to the LE/LC transition, the nonlinear response can be attributed to the phase transition of the lipids in the monolayer. In case of the mixed monolayer, this phase transition is strongly altered as observed by fluorescence microscopy (Section 8.2). Compared to the pure $F8H16$, the mixed monolayer is expected to have less defects since the free spaces between the $F8H16$ surface micelles are filled with the DPPC lipids.

These results are highly promising for the application of the mixed $F8H16$/DPPC monolayer as shell for the microbubbles since a predominantly elastic response with a low nonlinear contribution is favorable. However, further measurements are necessary in order to fully understand the interactions between the lipids and the $F8H16$ surface micelles. For example GISAXS measurements would reveal information about the lateral ordering and would especially help to unravel the origin of the additional phase transition observed in the π/A-isotherms.

9. Conclusion and Outlook

This thesis demonstrates that the self-assembly of semifluorinated alkanes into monolayers of well-ordered circular shaped surface micelles at the air/water interface regulates the interfacial viscoelastic properties. The viscoelastic properties were investigated using interfacial shear and dilational rheology and were correlated with the structure and form factors determined by grazing-incidence small-angle X-ray scattering. Towards potential biomedical applications of semifluorinated alkanes as the stabilizer for microbubbles used for sonographic imaging, the structure and mechanics of $FnHm$ diblock monolayers in a PFH-enriched atmosphere were studied and mixed monolayers of lipids and $F8H16$ surface micelles were investigated.

9.1. Conclusions

In Chapter 4, interfacial shear rheology measurements of semifluorinated alkane monolayers at the air/water interface are presented. The viscoelastic properties were investigated by systematically varying the amplitude and frequency of the applied shear stress while remaining in the linear response regime. The combination of the shear rheometer with a Langmuir film balance allowed to measure the elastic and viscous moduli with respect to the surface pressure of the monolayer as well. The obtained results indicate that the monolayers behave as predominantly elastic physical gels even at $0\,\mathrm{mN\,m^{-1}}$ surface pressure. The frequency-dependent elastic and viscous moduli could be well fitted using a Kelvin-Voigt model. This finding suggests that the surface micelles repel each other due to the repulsive interactions between dipoles arising from the CF_3 termini and the $CH_2 - CF_2$ junction of the molecules. The interfacial shear rheology measurements imply that subtle changes in the ratio between the fluorocarbon and hydrocarbon chains modulate the elastic and viscous moduli. This creates promising new perspectives for the fabrication of 2D gels with defined viscoelastic properties.

Complementary to the interfacial shear rheology, interfacial dilational rheology was applied on semifluorinated alkane monolayers. These results are presented in

Chapter 5. The stress response of both $FnHm$ and di($FnHm$) monolayers was recorded under oscillatory changes in the surface area and exhibited a clear nonlinearity. Therefore, the viscoelastic response functions were fitted by a Fourier series expansion. In a first step, the first mode was analyzed and used to calculate the elastic and viscous moduli which demonstrated that the monolayers behave predominantly elastic. The frequency-dependent data fit well to the simple linear Kelvin-Voigt model which reveals that the systems show a strong elastic response in combination with very low interfacial viscosities. Whereas the former is a result of the repulsive dipole interactions of the surface micelles, the latter can be attributed to the strong hydrophobicity of the molecules which lead to very low frictional forces between the monolayer and the water subphase.

The degree of nonlinearity was assessed by the total harmonic distortion which is in the range of $10-13\,\%$. Interestingly, the nonlinear signal arises mostly from uneven modes, especially the third mode, which one can hence attribute to the elastic part of the system due to mirror symmetry. Within the framework of Landau theory, the emergence of the uneven modes can be explained by a first order phase transition of the surface micelles under oscillatory strain. Using this approach, the viscoelastic response of semifluorinated alkane monolayers could be described by an extended Kelvin-Voigt model with a high spring constant ($g = 120 - 160\,\mathrm{mN\,m^{-1}}$), a small interfacial viscosity ($\eta = 20 - 60\,\mu\mathrm{N\,m\,s^{-1}}$) and a nonlinear term in the third order in the elasticity term with the proportionality factor $g' \approx 0.1g$.

To understand the origin of the unique viscoelastic properties of semifluorinated alkane monolayers, it is essential to unravel how they self-assemble at the air/water interface and how strongly they laterally correlate with each other. To this end, GISAXS was employed which allows to quantify the size, shape and correlation of the semifluorinated alkane surface micelles by fitting the intensity signal using a suitable form factor and structure factor. The results of this strategy are presented in Chapter 6. In case of the di($F10Hm$) tetrablock surface micelles, the combination of a form factor describing oblate hemiellipsoids with a structure factor that represents a 2D orthorhombic lattice was found to fit the scattering data best. Both axes D_x and D_y and therefore the size of the domains increase with the molecular length from $D_{x,\mathrm{di}(F10H16)} = (27 \pm 2)\,\mathrm{nm}$ and $D_{y,\mathrm{di}(F10H16)} = (31 \pm 1)\,\mathrm{nm}$ for di($F10H16$) to $D_{x,\mathrm{di}(F10H20)} = (42 \pm 2)\,\mathrm{nm}$ and $D_{y,\mathrm{di}(F10H20)} = (37 \pm 2)\,\mathrm{nm}$ for the di($F10H20$) surface micelles. Furthermore the width of the first peak of the structure factor allowed the calculation of the correlation length which was measured to be $8-$

14 times longer than the size of one surface micelle. The correlation length also increases with the size of the molecules which can by attributed to stronger repulsive interactions between the larger surface micelles. Interestingly, whereas at low surface pressures, the surface micelles have an almost circular shape, they deform to an elliptical shape with increasing surface pressure according to the direction of the compression of the monolayer.

In contrast, the GISAXS data recorded for the $FnHm$ diblock monolayers at the air/water interface revealed that they self-assemble into well-defined circular shaped surface micelles arranged in a hexagonal lattice which have similar sizes as the tetrablock molecules. The diameters of these domains as well as their correlation length where shown to increase both with hydrocarbon and fluorocarbon segment length.

Chapter 7 presents how a PFH-enriched atmosphere influences the structure and mechanics of $FnHm$ diblock monolayers on water. A significant change in the compressibility of $FnHm$ monolayers was observed ($\kappa_{FnHm,\mathrm{air}} = 7{-}8\,\mathrm{m\,N}$, $\kappa_{FnHm,\mathrm{PFH}} = 9{-}12\,\mathrm{m\,N}$). Also, the elastic modulus, measured by dilational rheology, is reduced by $\sim 25\,\%$. Interestingly, the shape, size and correlation of the surface micelles measured with GISAXS show no difference between air and the PFH-enriched atmosphere. It can therefore be concluded that a small number of PFH molecules adsorbs to the air/water interface between the surface micelles which has only minor effects on the static behavior of the monolayer whereas the elastic response is altered.

Studies on mixed monolayers of $F8H16$ and the lipid DPPC are presented in Chapter 8. The mixed monolayers behave very similarly to pure DPPC monolayers but very differently from pure $F8H16$ monolayers: Both the DPPC monolayer and the $F8H16$/DPPC monolayer undergo a phase transition upon isothermal compression at a surface pressure of $5\,\mathrm{mN\,m^{-1}}$ which can be attributed to the phase transition of DPPC from the LE to the LC phase. Fluorescence microscopy revealed that $F8H16$ hinders the growth of the LC-rich DPPC domains during compression by reducing the line tension.

The dilational viscoelasticity at small surface pressures ($4\,\mathrm{mN\,m^{-1}}$) is very similar to that of the pure DPPC monolayer. All monolayers measured exhibit a nonlinear response. Both the dilational elastic modulus E_1' and the viscous modulus E_1'' calculated from the first modes are independent of the frequency in the measured regime with $E_1' \approx 24\,\mathrm{mN\,m^{-1}}$ and $E_1'' \approx 0.7\,\mathrm{mN\,m^{-1}}$. These values are strongly

reduced compared to the pure $F8H16$ monolayer. This suggests that DPPC screens the repulsive interactions of the $F8H16$ surface micelles. Interestingly, the degree of nonlinearity of the mixed $F8H16$/DPPC monolayer is lower compared to the pure monolayers of DPPC and $F8H16$. The increase of the second Fourier mode at higher strain amplitudes suggests that the contribution of the nonlinear viscous response is increased compared to small amplitudes. The viscoelastic response of the mixed monolayer is hence dominated by the viscoelastic properties of the DPPC monolayer.

9.2. Outlook

The results of this thesis are highly promising for the application of semifluorinated alkanes as microbubbles used for sonographic imaging which are filled with PFH vapor in order to gain further stability. The data presented in Chapter 7 show that PFH only merely influences the behavior of semifluorinated alkane monolayers on water. This suggests that the PFH would stay inside the microbubble without destroying the shell composed of the self-assembled semifluorinated alkanes. Combining the semifluorinated alkanes with lipids is another very promising approach as lipid microbubbles form easily and the semifluorinated alkanes could extend their lifetime with their hydrophobic nature. Therefore, it is interesting to see that the semifluorinated alkanes do not influence the viscoelastic behavior of the lipid film in the LE phase. Indeed, it is very favorable for the application that they even decrease the nonlinearity of the response function. Of course all measurements were only performed on model systems of 2D films. After the successful formation of microbubbles, it is necessary to perform thorough investigations on these 3D systems to learn more about their mechanics and especially their behavior under ultrasonic stress.

Apart from this, investigations on the behavior of 2D films that self-assemble into ordered domains is very interesting from a physical point of view since the physical interactions regulating the viscoelastic properties are governed by two factors: the intermolecular interactions between single molecules and the macroscopic interactions between individual domains. This thesis shows that the mechanical properties of $FnHm$ and di($FnHm$) monolayers are governed by the surface micelles which interact in a repulsive manner. So far, there are only few studies about the viscoelastic behavior of nanodomains at the air/water interface and it is still mostly unclear to what extent the existence of nanodomains influences the viscoelastic properties of interfaces. Li Destri et al. for example studied the rheology of monolayers composed

of copolymer molecules that form circular or worm-like micelles at the air/water interface.[20] They found that the circular pattern results in a predominantly elastic response whereas an entanglement of the micelles leads to a rather viscous behavior. It can be assumed that the stronger elastic response of the circular domains originates from the weaker attractive interactions between the domains compared to elongated structures. This is in line with our system of semifluorinated alkanes which show a strong elastic response which can be attributed to the repulsive behavior of circular shaped surface micelles. The interaction between the surface micelles is strongly altered by mixing the semifluorinated alkanes with lipids. This thesis shows that the elastic and viscous moduli of a 1:1 mixture of DPPC and $F8H16$ is strongly decreased compared to the pure $F8H16$ monolayer. Most probably, the concentration of the lipid can hence act as a parameter to systematically tune the elastic and viscous moduli. Monolayers of $FnHm$ with and without lipids could hence act as an easily controllable model system of organized systems on a mesoscopic scale.

A. Supplementary Information

A.1. Supplementary Information for Chapter 4

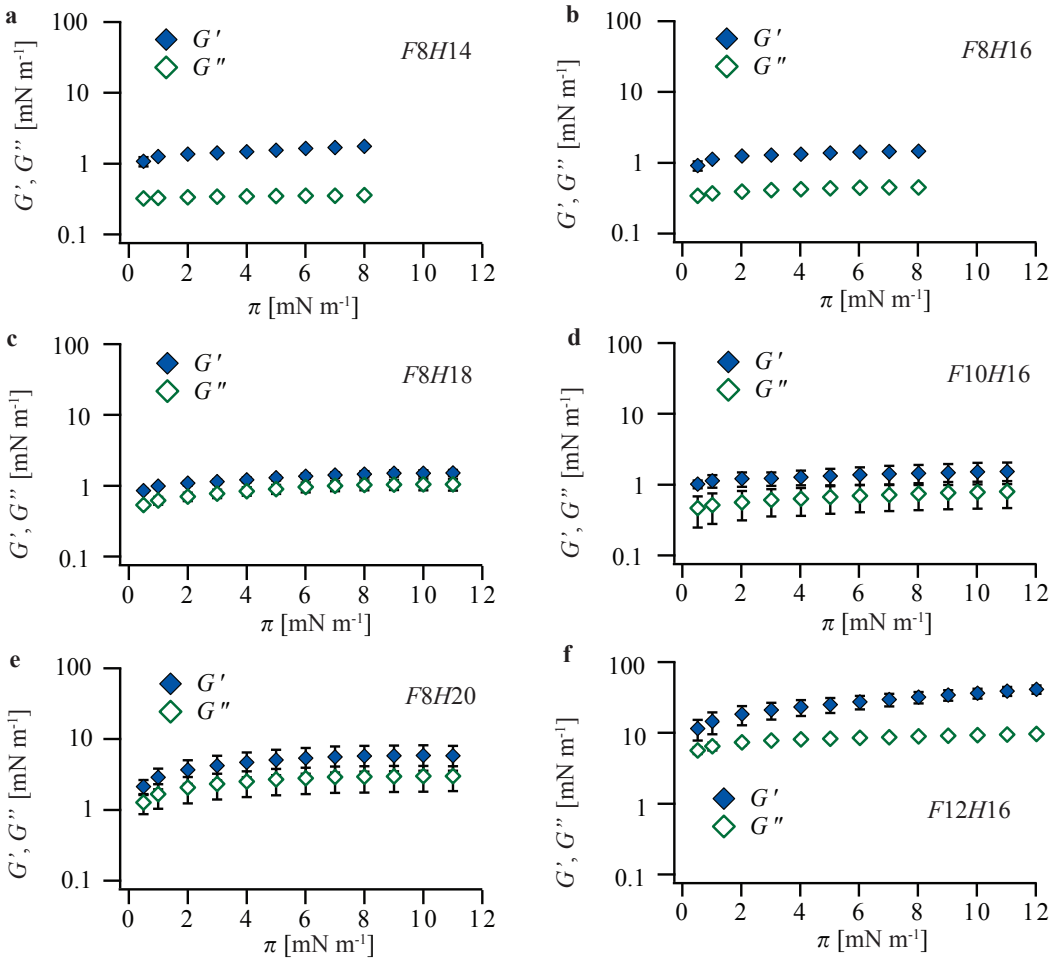

Figure A.1.: Shear elastic and viscous moduli G' and G'' with respect to the frequency for all $FnHm$ diblocks measured at the frequency $f = 3\,\mathrm{Hz}$ and amplitude $\gamma = 1.5\,\mathrm{mrad}$.

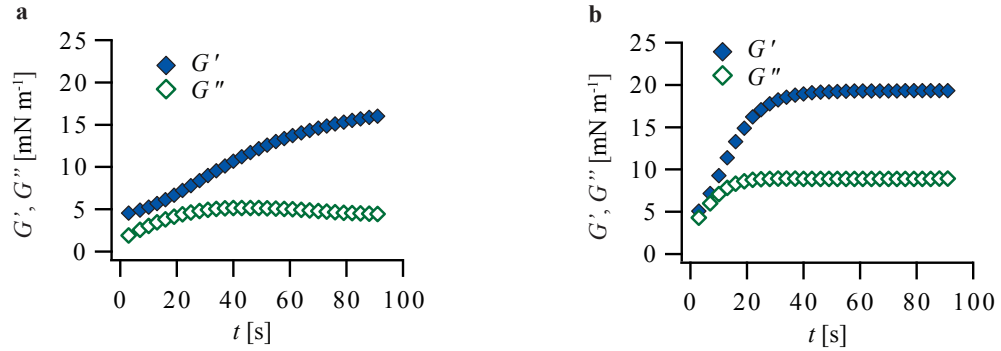

Figure A.2.: Interfacial shear rheology of a $F12H16$ monolayer at $f = 3\,\mathrm{Hz}$ and $\gamma = 1.5\,\mathrm{mrad}$ (a) and $f = 5\,\mathrm{Hz}$ and $\gamma = 3\,\mathrm{mrad}$ (b).

A.2. Supplementary Information for Chapter 5

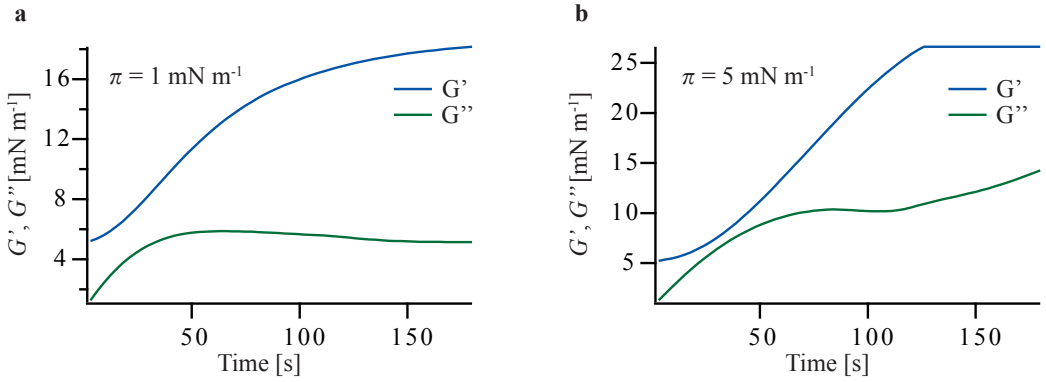

Figure A.3.: Shear elastic and viscous moduli G' and G'' of a di($F10H18$) monolayer at $\pi = 1\,\mathrm{mN\,m^{-1}}$ (a) and $\pi = 5\,\mathrm{mN\,m^{-1}}$ (b). The measurements were performed at $f = 3\,\mathrm{Hz}$ and $\gamma = 1.5\,\mathrm{mrad}$. It was not possible to reach equilibrium even after 180 s, also at other frequency / amplitude conditions. Also, at surface pressures $\pi > 1\,\mathrm{mN\,m^{-1}}$, the film was too stiff and the values of G' exceeded the sensitivity of the rheometer ($\sim 26\,\mathrm{mN\,m^{-1}}$).

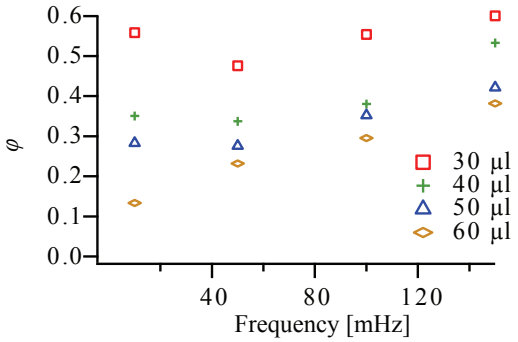

Figure A.4.: Influence of the amount of di($F10H16$) molecules (1 mM) spread on the air/water interface on the phase separation φ between stress and strain.

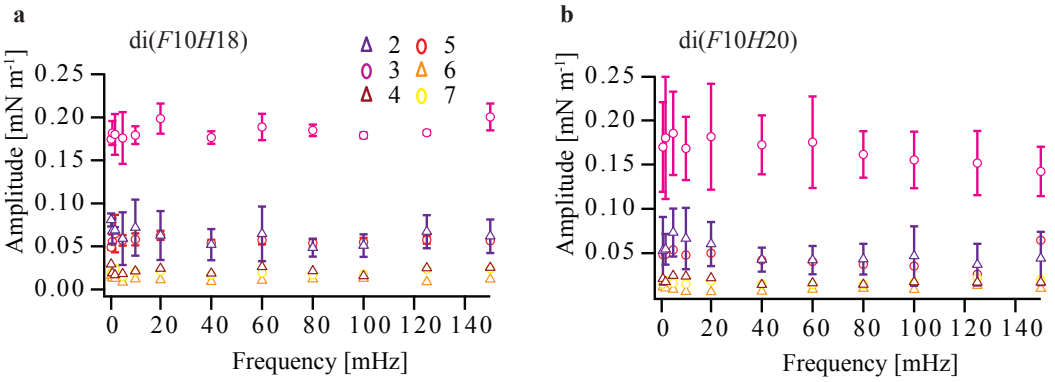

Figure A.5.: Amplitudes of the higher Fourier modes of di($F10H18$) (a) and di($F10H20$) (b) with respect to the frequency.

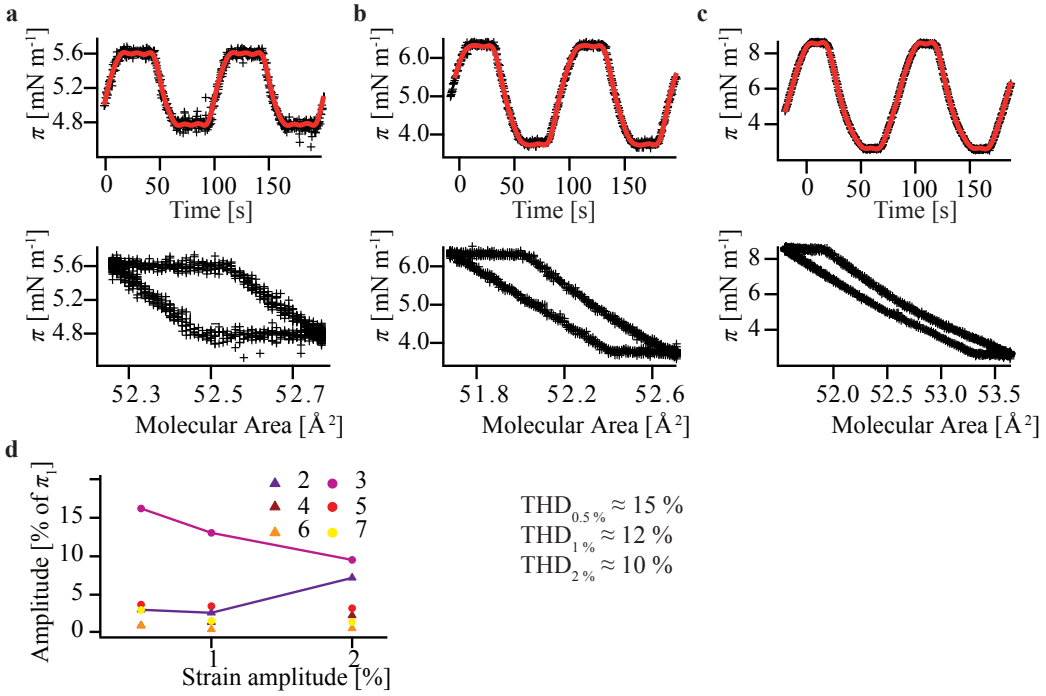

Figure A.6.: Influence of the strain amplitude on the dilational rheology of a di($F10H16$) monolayer at $\pi = 5\,\mathrm{mN\,m^{-1}}$ and $f = 10\,\mathrm{mHz}$. a) $u_0 = 0.005$, b) $u_0 = 0.01$, c) $u_0 = 0.02$. d) Fractions of the higher mode amplitudes plotted as a function of the strain amplitude showing the emergence of the second mode at $u_0 = 0.02$.

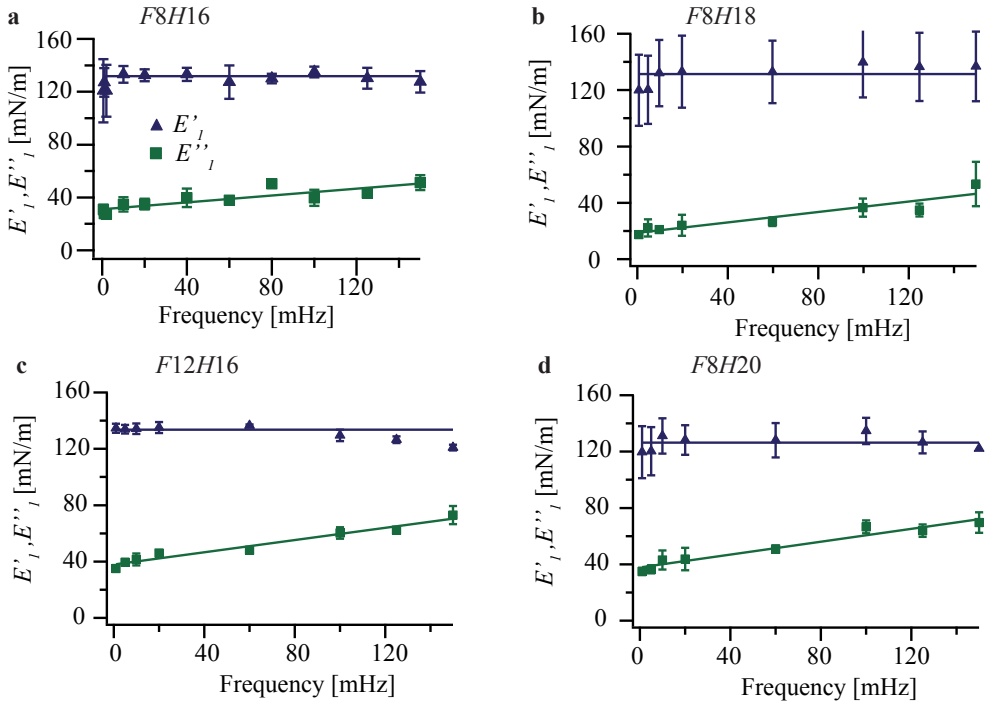

Figure A.7.: Dilational elastic and viscous moduli for $F8H16$ (a), $F8H18$ (b), $F12H16$ (c) and $F8H20$ (d) monolayers.

A.3. Supplementary Information for Chapter 6

Molecule	Diameter D [nm]		Correlation Length ξ [nm]	
	air	PFH	air	PFH
$F8H16$	29.08 ± 0.51	29.44 ± 0.64	350	330
$F10H16$	30.36 ± 0.32	29.06 ± 0.64	505	605
$F12H16$	33.16 ± 0.88	32.09 ± 0.62	870	750
$F8H18$	31.99 ± 0.72	31.63 ± 0.81	585	680
$F8H20$	35.46 ± 0.26	34.19 ± 0.55	1000	880

Table A.1.: GISAXS data in air and in PFH-enriched atmosphere for all measured $FnHm$ monolayers.

A.4. Supplementary Information for Chapter 7

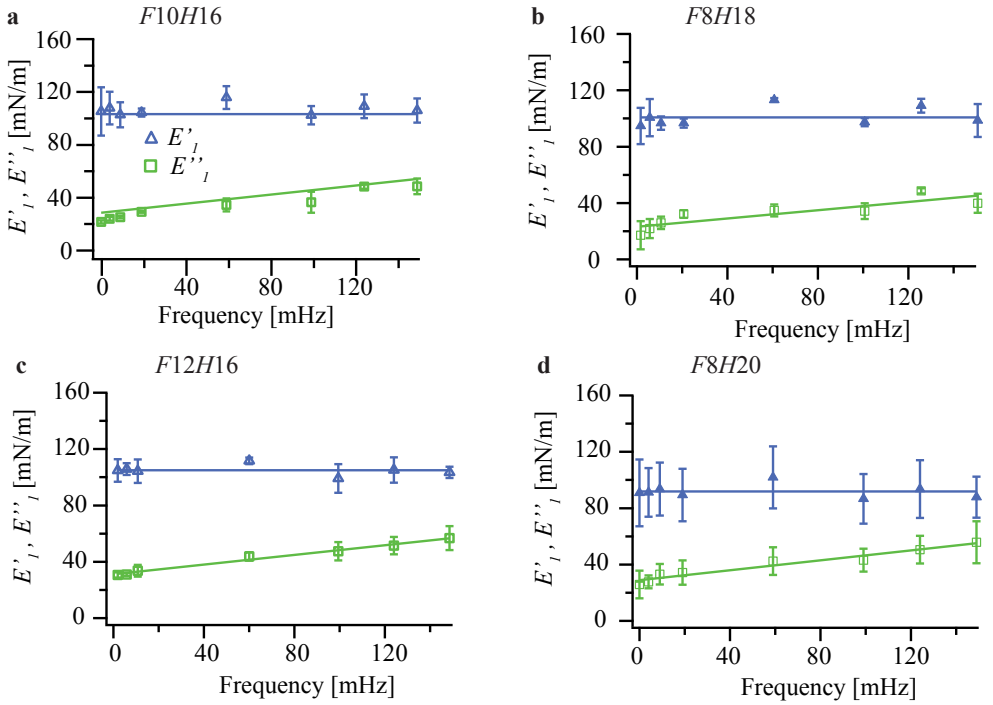

Figure A.8.: E_1' and E_1'' vs. frequency for the $F10H16$, $F12H16$, $F8H18$ and $F8H20$ monolayers in a PFH-enriched atmosphere.

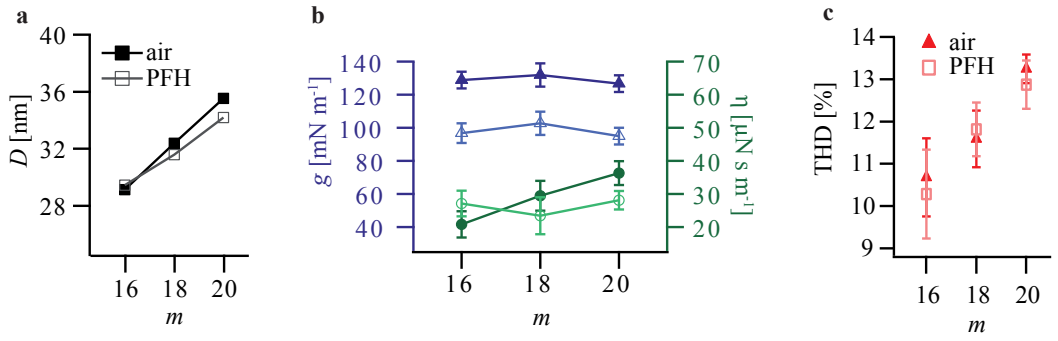

Figure A.9.: Dilational rheology of $F8Hm$ monolayers in air and in PFH-enriched atmosphere. a) Diameter obtained from GISAXS with respect to the hydrocarbon segment length m. b) Spring constant g and interfacial viscosity η with respect to m. c) THD with respect to m. Air data are presented as filled data points in darker color, the datapoints for the measurements in the PFH-enriched atmosphere are of a brighter color and open symbols.

A.5. Supplementary Information for Chapter 8

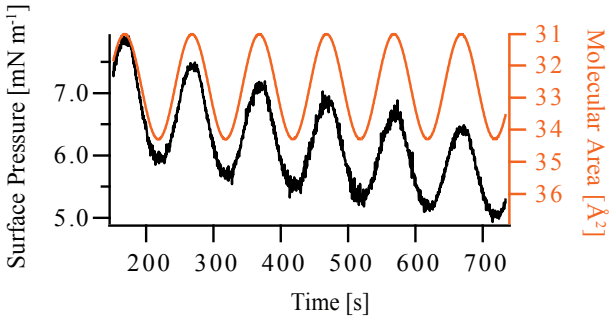

Figure A.10.: Surface pressure response of interfacial dilational rheology of the mixed $F8H16$/DPPC monolayer at $\pi_0 = 7\,\mathrm{mN\,m^{-1}}$

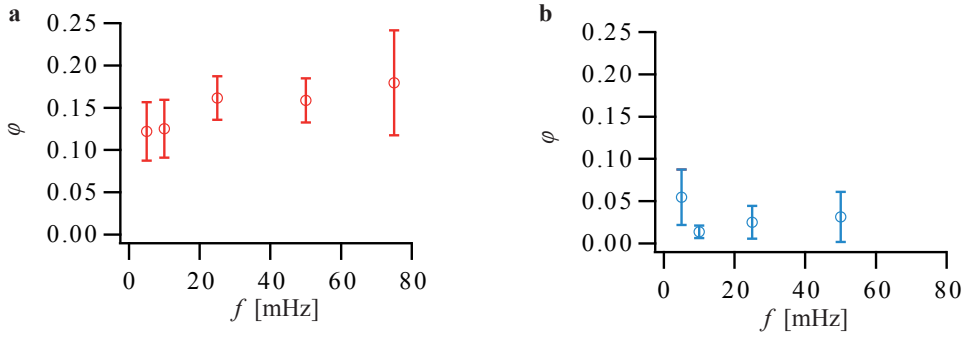

Figure A.11.: Phase separation vs. Frequency for a $F8H16$/DPPC monolayer with $u_0 = 0.02$ (a) and a DPPC monolayer with $u_0 = 0.05$ (b).

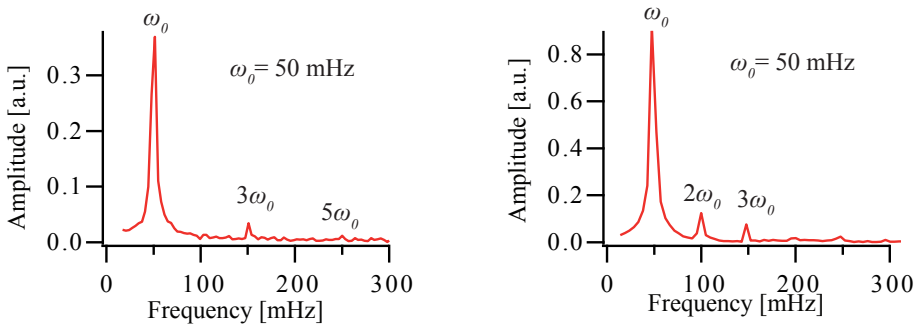

Figure A.12.: Fourier Spectra of a $F8H16$/DPPC monolayer ($u_0 = 0.02$) (a) and a DPPC monolayer ($u_0 = 0.05$) (b) recorded at $f = 0.05$.

List of Publications

Included in this thesis

Abuillan, W., Veschgini, M., **Mielke, S.**, Yamamoto, A., Liu, X., Konovalov, O., Krafft, M. P., & Tanaka, M. (2019) Long-Range Lateral Correlation between Self-Assembled Domains of Fluorocarbon-Hydrocarbon Tetrablocks by Quantitative GISAXS. *ChemPhysChem, 20*(6), 898-904.

Mielke, S., Habe, T., Veschgini, M., Liu, X., Yoshikawa, K., Krafft, M. P., & Tanaka, M. (2018). Emergence of Strong Nonlinear Viscoelastic Response of Semifluorinated Alkane Monolayers. *Langmuir, 34*(7), 2489-2496.

Veschgini, M., Abuillan, W., Inoue, S., Yamamoto, A., **Mielke, S.**, Liu, X., Konovalov, O., Krafft, M. P., & Tanaka, M. (2017). Size, Shape, and Lateral Correlation of Highly Uniform, Mesoscopic, Self-Assembled Domains of Fluorocarbon-Hydrocarbon Diblocks at the Air/Water Interface: A GISAXS Study. *ChemPhysChem, 18*(19), 2791-2798.

Veschgini, M., Habe, T., **Mielke, S**., Inoue, S., Liu, X., Krafft, M. P., & Tanaka, M. (2017). Existence of Two-Dimensional Physical Gels even at Zero Surface Pressure at the Air/Water Interface: Rheology of Self-Assembled Domains of Small Molecules. *Angewandte Chemie, 129*(41), 12777-12781.

Not included in this thesis

Masuda, S., **Mielke, S**., Amadei, F., Yamamoto, A., Wang, P., Taniguchi, T., Yoshikawa, K., Tamada, K., & Tanaka, M. (2018). Nonlinear Viscoelasticity of Highly Ordered, Two-Dimensional Assemblies of Metal Nanoparticles Confined at the Air/Water Interface. *Langmuir, 34*(43), 13025-13034.

Liu, X., **Mielke, S.**, Contal, C., Favier, D., Yamamoto, A., Tanaka, M., & Krafft, M. P. (2018). 2D Spherulites of a Semi-Fluorinated Alkane: Controlled Access to Either Radial Or Ring-Banded Morphologies. *ChemPhysChem, 19*(1), 29-33.

References

[1] Albrecht, O., Gruler, H., and Sackmann, E. (1978). Polymorphism of phospholipid monolayers. *J. Phys.*, 39(3):301–313.

[2] Altamura, D., Sibillano, T., Siliqi, D., Caro, L. D., and Giannini, C. (2012). Assembled Nanostructured Architectures Studied By Grazing Incidence X-Ray Scattering. *Nanomater. Nanotechnol.*, 2:2–16.

[3] Andelman, D. and Rosensweig, R. E. (2009). Modulated Phases: Review and Recent Results. *J. Phys. Chem. B*, 113(12):3785–3798.

[4] Arriaga, L. R., López-Montero, I., Rodríguez-García, R., and Monroy, F. (2008). Nonlinear dilational mechanics of Langmuir lipid monolayers: a lateral diffusion mechanism. *Phys. Rev. E. Stat. Nonlin. Soft Matter Phys.*, 77(6):061918.

[5] Babonneau, D. (2010). FitGISAXS: software package for modelling and analysis of GISAXS data using IGOR Pro. *J. Appl. Crystallogr.*, 43(4):929–936.

[6] Bardin, L., Faur, M.-c., Limagne, D., Chevallard, C., Konovalov, O., Filipe, E. J. M., Waton, G., Goldmann, M., and Fontaine, P. (2011). Long-Range Nanometer-Scale Organization of Semifluorinated Alkane Monolayers at the Air/Water Interface. *Langmuir*, 27(22):13497–13505.

[7] Bertilla, S. M., Thomas, J.-L., Marie, P., and Krafft, M. P. (2004). Cosurfactant Effect of a Semifluorinated Alkane at a Fluorocarbon/Water Interface: Impact on the Stabilization of Fluorocarbon-in-Water Emulsions. *Langmuir*, 20(10):3920–3924.

[8] Bleyl, J. U., Ragaller, M., Tscho, U., Regner, M., Kanzow, M., Hubler, M., Rasche, S., and Albrecht, M. (1999). Vaporized perfluorocarbon improves oxygenation and pulmonary function in an ovine model of acute respiratory distress syndrome. *Anesthesiol. J. Am. Soc. Anesthesiol.*, 91(2):461–469.

[9] Bondi, A. (1964). van der Waals volumes and radii. *J. Phys. Chem.*, 68(3):441–451.

[10] Brace, N. O. (1999). Syntheses with perfluoroalkyl radicals from perfluoroalkyl iodides. A rapid survey of synthetic possibilities with emphasis on practical applications. Part one: alkenes, alkynes and allylic compounds. *J. Fluor. Chem.*, 93(1):1–25.

[11] Brinson, H. F. and Brinson, L. C. (2015). *Polymer Engineering Science and Viscoelasticity: An Introduction*. Springer US, 2 edition.

[12] Broniatowski, M., Sandez Macho, I., Miñones, J., and Dynarowicz-Łatka, P. (2004). Langmuir Monolayers Characteristic of (Perfluorodecyl)-Alkanes. *J. Phys. Chem. B*, 108(35):13403–13411.

[13] Brzoska, J. B., Shahidzadeh, N., and Rondelez, F. (1992). Evidence of a transition temperature for the optimum deposition of grafted monolayer coatings. *Nature*, 360(6406):719.

[14] Cape, J. A., Hall, W. F., and Lehman, G. W. (1974). Theory of magnetic domain dynamics in uniaxial materials. *J. Appl. Phys.*, 45(8):3572–3581.

[15] Chernyshev, V. S. and Skliar, M. (2013). Surface Tension of Water in the Presence of Perfluorocarbon Vapors. *Soft Matter*, 10(12):1937–1943.

[16] Cohen, I., Mason, T. G., and Weitz, D. A. (2004). Shear-Induced Configurations of Confined Colloidal Suspensions. *Phys. Rev. Lett.*, 93(4):046001.

[17] de Gracia Lux, C., Gallani, J. L., Waton, G., and ierre Krafft, M. P. (2010). Compression of self-assembled nano-objects: 2D/3D transitions in films of (perfluoroalkyl)alkanes-persistence of an organized array of surface micelles. *Chem. - A Eur. J.*, 16(24):7186–7198.

[18] de Gracia Lux, C., Gallani, J.-L., Waton, G., and Krafft, M. P. (2012). Stacking of Self-Assembled Surface Micelles in Ultrathin Films. *ChemPhysChem*, 2(6):1454–1462.

[19] de Gracia Lux, C. and Krafft, M. P. (2010). Nonpolar Gemini Amphiphiles Self-Assemble into Stacked Layers of Nano-Objects. *Chem. - A Eur. J.*, 16(38):11539–11542.

[20] Destri, G. L., Miano, F., and Marletta, G. (2014). Structure - Rheology Relationship in Weakly Amphiphilic Block Copolymer Langmuir Monolayers. *Langmuir*, 30:3345–3353.

[21] Dillmann, P., Maret, G., and Keim, P. (2012). Comparison of 2D melting criteria in a colloidal system. *J. Phys. Condens. Matter*, 24(46):464118.

[22] Ferro, Y. and Krafft, M. P. (2002). Incorporation of semi-fluorinated alkanes in the bilayer of small unilamellar vesicles of phosphatidylserine: impact on fusion kinetics. *Biochim. Biophys. Acta*, 1581(1-2):11–20.

[23] Fontaine, P., Fauré, M.-C., Bardin, L., Filipe, E. J. M., and Goldmann, M. (2014). Evidence for Interaction with the Water Subphase As the Origin and Stabilization of Nano-Domain in Semi-Fluorinated Alkanes Monolayer at the Air/Water Interface. *Langmuir*, 30(50):15193–15199.

[24] Fontaine, P., Goldmann, M., Muller, P., Faure, M.-c., Konovalov, O., and Krafft, M. P. (2005). Direct Evidence for Highly Organized Networks of Circular Surface Micelles of Surfactant at the Air-Water Interface. *J. Am. Chem. Soc.*, 127(2):512–513.

[25] Fung, Y.-c., Tong, P., and Chen, X. (2001). *Classical and Computational Solid Mechanics*. Advanced series in engineering science. World Scientific Publishing Company.

[26] Gaines Jr, G. L. (1991). Surface activity of semifluorinated alkanes: F(CF2)m(CH2)nH. *Langmuir*, 7(12):3054–3056.

[27] Gerber, F., Krafft, M. P., and Vandamme, T. F. (2007). The detrimental effect of serum albumin on the re-spreading of a dipalmitoyl phosphatidylcholine Langmuir monolayer is counteracted by a fluorocarbon gas. *Biochim. Biophys. Acta - Biomembr.*, 1768(3):490–494.

[28] Gerber, F., Krafft, M. P., Vandamme, T. F., Goldmann, M., and Fontaine, P. (2006). Fluidization of a Dipalmitoyl Phosphatidylcholine Monolayer by Fluorocarbon Gases: Potential Use in Lung Surfactant Therapy. *Biophys. J.*, 90(9):3184–3192.

[29] Gerber, F., Vandamme, T. F., and Krafft, M. P. (2009). Impact of perfluorooctylethane on the formation of a semi-crystalline liquid-condensed phase in a phospholipid monolayer and of perfluorooctyl bromide on the adsorption of albumin on such a monolayer. *Comptes Rendus Chim.*, 12(1-2):180–187.

[30] González-Pérez, A., Contal, C., and Krafft, M. P. (2007). Experimental evidence for a surface concentration-dependent mechanism of formation of hemimicelles in Langmuir monolayers of semi-fluorinated alkanes. *Soft Matter*, 3(2):191–193.

[31] Guo, Z. and Kindt, J. T. (2018). Partitioning of Size-Mismatched Impurities to Grain Boundaries in 2d Solid Hard-Sphere Monolayers. *Langmuir*, 34(43):12947–12956.

[32] Guzmán, E., Liggieri, L., Santini, E., Ferrari, M., and Ravera, F. (2011). Effect of Hydrophilic and Hydrophobic Nanoparticles on the Surface Pressure Response of DPPC Monolayers. *J. Phys. Chem. C*, 115(44):21715–21722.

[33] Guzmán, E., Liggieri, L., Santini, E., Ferrari, M., and Ravera, F. (2012). DPPC-DOPC Langmuir monolayers modified by hydrophilic silica nanoparticles: Phase behaviour, structure and rheology. *Colloids Surfaces A Physicochem. Eng. Asp.*, 413:174–183.

[34] Haken, H. (2012). *Synergetics: An Introduction Nonequilibrium Phase Transitions and Self-Organization in Physics, Chemistry and Biology*. Springer Series in Synergetics. Springer Berlin Heidelberg.

[35] Haynes, W. M. (2014). *CRC handbook of chemistry and physics*. CRC press.

[36] Heckl, W. M., Cadenhead, D. A., and Moehwald, H. (1988). Cholesterol concentration dependence of quasi-crystalline domains in mixed monolayers of the cholesterol-dimyristoylphosphatidic acid system. *Langmuir*, 4(6):1352–1358.

[37] Herrmann, M., Schneck, E., Gutsmann, T., Brandenburg, K., and Tanaka, M. (2015). Bacterial lipopolysaccharides form physically cross-linked, two-dimensional gels in the presence of divalent cations. *Soft Matter*, 11(30):6037–6044.

[38] Hillebrandt, H. and Tanaka, M. (2001). Electrochemical characterization of self-assembled alkylsiloxane monolayers on indium- tin oxide (ITO) semiconductor electrodes. *J. Phys. Chem. B*, 105(19):4270–4276.

[39] Hilles, H., Monroy, F., Bonales, L. J., Ortega, F., and Rubio, R. G. R. G. (2006). Fourier-transform rheology of polymer Langmuir monolayers: Analysis of the non-linear and plastic behaviors. *Adv. Colloid Interface Sci.*, 122(1-3):67–77.

[40] Hu, S., Nozawa, J., Koizumi, H., Fujiwara, K., and Uda, S. (2015). Grain Boundary Segregation of Impurities During Polycrystalline Colloidal Crystallization. *Cryst. Growth Des.*, 15(12):5685–5692.

[41] Hyun, K., Wilhelm, M., Klein, C. O., Cho, K. S., Nam, J. G., Ahn, K. H., Lee, S. J., Ewoldt, R. H., and McKinley, G. H. (2011). A review of nonlinear oscillatory shear tests: Analysis and application of large amplitude oscillatory shear (LAOS). *Prog. Polym. Sci.*, 36(12):1697–1753.

[42] Jones, M. N. and Chapman, D. (1994). *Micelles, Monolayers, and Biomembranes*. Wiley.

[43] Jones, R. A. L. (2002). *Soft Condensed Matter*. Oxford Master Series in Physics. OUP Oxford.

[44] Kabalnov, A., Klein, D., Pelura, T., Schutt, E., and Weers, J. (1998). Dissolution of multicomponent microbubbles in the bloodstream: 1. theory. *Ultrasound Med. Biol.*, 24(5):739–749.

[45] Klein, C. O., Viguerie, L. D., Christopoulou, C., Jonas, U., Clark, C. G., and Klaus, M. (2011). Viscoelasticity of semifluorinated alkanes at the air/water interface. *Soft Matter*, 7(17):7737–7746.

[46] Knobler, C. M. (1990). Seeing phenomena in flatland: studies of monolayers by fluorescence microscopy. *Science*, 249(4971):870–874.

[47] Kovalenko, A., Polavarapu, P., Gallani, J.-L., Pourroy, G., Waton, G., and Krafft, M. P. (2014). Super-Elastic Air/Water Interfacial Films Self-Assembled from Soluble Surfactants. *ChemPhysChem*, 15(12):2440–2444.

[48] Krafft, M. P. (2012). Large organized surface domains self-assembled from nonpolar amphiphiles. *Acc. Chem. Res.*, 45(4):514–24.

[49] Krafft, M. P. (2015). Fluorine in medical microbubbles - Methodologies implemented for engineering and investigating fluorocarbon-based microbubbles. *J. Fluor. Chem.*, 177:19–28.

[50] Krafft, M. P., Giulieri, F., Fontaine, P., and Goldmann, M. (2001). Reversible Stepwise Formation of Mono- and Bilayers of a Fluorocarbon/Hydrocarbon Diblock on Top of a Phospholipid Langmuir Monolayer. A Case of Vertical Phase Separation. *Langmuir*, 17(21):6577–6584.

[51] Krafft, M. P. and Riess, J. G. (2007). Perfluorocarbons: Life sciences and biomedical uses Dedicated to the memory of Professor Guy Ourisson, a true RENAISSANCE man. *J. Polym. Sci. Part A Polym. Chem.*, 45(7):1185–1198.

[52] Krafft, M. P. and Riess, J. G. (2009). Chemistry, Physical Chemistry, and Uses of Molecular Fluorocarbon - Hydrocarbon Diblocks, Triblocks, and Related Compounds. *Chem. Rev.*, 109(5):1714–1792.

[53] KSV NIMA / Biolin Scientific Oy (2013). *Software Manual Langmuir and Langmuir-Blodgett devices.*

[54] Larson, R. G. (1999). *The Structure and Rheology of Complex Fluids.* Topics in Chemical Engineering. OUP USA.

[55] Lee, H., Kim, H., Han, H., Lee, M., Lee, S., Yoo, H., Ho, J., and Kim, H. (2017). Microbubbles used for contrast enhanced ultrasound and theragnosis : a review of principles to applications. *Biomed. Eng. Lett.*, 7(2):59–69.

[56] Lemal, D. M. (2004). Perspective on Fluorocarbon Chemistry. *J. Org. Chem.*, 69(1):1–11.

[57] Lifschitz, E. M., Landau, L. D., and Pitaevskij, L. P. (1983). *Lehrbuch der theoretischen Physik : in 10 Bänden. 10. Physikalische Kinetik.* Lehrbuch der theoretischen Physik. Akademie-Verlag, Berlin.

[58] Liggieri, L. and Miller, R. (2009). *Interfacial rheology.* CRC Press.

[59] Liggieri, L. and Miller, R. (2010). Relaxation of surfactants adsorption layers at liquid interfaces. *Curr. Opin. Colloid Interface Sci.*, 15(4):256–263.

[60] Loglio, G., Pandolfini, P., Miller, R., Makievski, A. V., Krägel, J., Ravera, F., and Noskov, B. A. (2005). Perturbation–response relationship in liquid interfacial systems: non-linearity assessment by frequency–domain analysis. *Colloids Surfaces A Physicochem. Eng. Asp.*, 261(1):57–63.

[61] López-Montero, I., Catapano, E. R., Espinosa, G., Arriaga, L. R., Langevin, D., and Monroy, F. (2013). Shear and compression rheology of langmuir monolayers of natural ceramides: Solid character and plasticity. *Langmuir*, 29(22):6634–6644.

[62] Lucassen, J. and Van Den Tempel, M. (1972). Dynamic measurements of dilational properties of a liquid interface. *Chem. Eng. Sci.*, 27(6):1283–1291.

[63] Lucero Caro, A., Rodríguez Niño, M. R., and Rodríguez Patino, J. M. (2008). The effect of pH on surface dilatational and shear properties of phospholipid monolayers. *Colloids Surfaces A Physicochem. Eng. Asp.*, 327(1-3):79–89.

[64] Lyadinskaya, V., Bykov, A., Campbell, R., Varga, I., Lin, S., Loglio, G., Miller, R., and Noskov, B. (2014). Dynamic surface elasticity of mixed poly(diallyldimethylammonium chloride)/sodium dodecyl sulfate/NaCl solutions. *Colloids Surfaces A Physicochem. Eng. Asp.*, 460:3–10.

[65] Maaloum, M., Muller, P., and Krafft, M. P. (2002). Monodisperse Surface Micelles of Nonpolar Amphiphiles in Langmuir Monolayers. *Angew. Chemie Int. Ed.*, 41(22):4331–4334.

[66] Maaloum, M., Muller, P., and Krafft, M. P. (2004). Lateral and Vertical Nanophase Separation in Langmuir-Blodgett Films of Phospholipids and Semifluorinated Alkanes. *Langmuir*, 20(6):2261–2264.

[67] Mahler, W., Guillon, D., and Skoulios, A. (1985). Smectic liquid crystal from (perfluorodecyl)decane. *Mol. Cryst. Liq. Crystals, Lett.*, 2(3-4):111 – 119.

[68] Makino, M. and Yoshikawa, K. (1997). Dynamic Properties of a Phospholipid Thin Film at an Air/Water Interface with a Periodic Change in Surface Area. *Langmuir*, 13(26):7125–7134.

[69] Maruyama, N., Koito, T., Nishida, J., Sawadaishi, T., Cieren, X., Ijiro, K., Karthaus, O., and Shimomura, M. (1998). Mesoscopic patterns of molecular aggregates on solid substrates. *Thin Solid Films*, 327-329:854–856.

[70] Masuda, S., Mielke, S., Amadei, F., Yamamoto, A., Wang, P., Taniguchi, T., Yoshikawa, K., Tamada, K., and Tanaka, M. (2018). Nonlinear Viscoelasticity of Highly Ordered, Two-Dimensional Assemblies of Metal Nanoparticles Confined at the Air/Water Interface. *Langmuir*, 34(43):13025–13034.

[71] McConlogue, C. W. and Vanderlick, T. K. (1997). A Close Look at Domain Formation in DPPC Monolayers. *Langmuir*, 13(26):7158–7164.

[72] McConnell, H. M. (1989). Theory of hexagonal and stripe phases in monolayers. *Proc. Natl. Acad. Sci. U. S. A.*, 86(10):3452–5.

[73] McConnell, H. M. and De Koker, R. (1992). Note on the theory of the sizes and shapes of lipid domains in monolayers. *J. Phys. Chem.*, 96(17):7101–7103.

[74] McConnell, H. M. and Moy, V. T. (1988). Shapes of finite two-dimensional lipid domains. *J. Phys. Chem.*, 92(15):4520–4525.

[75] McLean, D. (1957). *Grain boundaries in metals, Monographs on the physics and chemistry of materials*. Oxford University Press., London.

[76] Miller, R., Ferri, J. K., Javadi, A., Krägel, J., Mucic, N., and Wüstneck, R. (2010). Rheology of interfacial layers. *Colloid Polym. Sci.*, 288(9):937–950.

[77] Mouritsen, O. G. (2006). *Life - As a Matter of Fat: The Emerging Science of Lipidomics*. The Frontiers Collection. Springer Berlin Heidelberg.

[78] Mourran, A., Tartsch, B., Gallyamov, M., Magonov, S., Lambreva, D., Ostrovskii, B. I., Dolbnya, I. P., De Jeu, W. H., and Moeller, M. (2005). Self-assembly of the perfluoroalkyl-alkane F14H20 in ultrathin films. *Langmuir*, 21(6):2308–2316.

[79] Müller-Buschbaum, P. (2009). A Basic Introduction to Grazing Incidence Small-Angle X-Ray Scattering. In Ezquerra, T., Garcia-Gutierrez, M. C., Nogales, A., and Gomez, M., editors, *Appl. Synchrotron Light to Scatt. Diffr. Mater. Life Sci.* Springer, Heidelberg.

[80] Naumann, C. A., Brooks, C. F., Fuller, G. G., Knoll, W., and Frank, C. W. (1999). Viscoelastic Properties of Lipopolymers at the Air-Water Interface: A Combined Interfacial Stress Rheometer and Film Balance Study. *Langmuir*, 15(22):7752–7761.

[81] Naumann, C. A., Brooks, C. F., Fuller, G. G., Lehmann, T., Rühe, J., Knoll, W., Kuhn, P., Nuyken, O., and Frank, C. W. (2001). Two-Dimensional Physical Networks of Lipopolymers at the Air/Water Interface: Correlation of Molecular Structure and Surface Rheological Behavior. *Langmuir*, 17(9):2801–2806.

[82] Nguyen, P. N., Veschgini, M., Tanaka, M., Waton, G., Vandamme, T., and Krafft, M. P. (2014). Counteracting the inhibitory effect of proteins towards lung surfactant substitutes: a fluorocarbon gas helps displace albumin at the air/water interface. *Chem. Commun.*, 50(78):11576–11579.

[83] Noskov, B., Loglio, G., and Miller, R. (2011). Dilational surface visco-elasticity of polyelectrolyte/surfactant solutions: Formation of heterogeneous adsorption layers. *Adv. Colloid Interface Sci.*, 168(1):179–197.

[84] Oelke, J., Pasc, A., Wixforth, A., Konovalov, O., and Tanaka, M. (2008). Highly uniform, strongly correlated fluorinated lipid nanodomains embedded in biological membrane models. *Appl. Phys. Lett.*, 93(21):1–3.

[85] Ophir, J. and Parker, K. J. (1989). Contrast agents in diagnostic ultrasound. *Ultrasound Med. Biol.*, 15(4):319–333.

[86] Paefgen, V., Doleschel, D., and Kiessling, F. (2015). Evolution of contrast agents for ultrasound imaging and ultrasound-mediated drug delivery. *Front. Pharmacol.*, 6:197.

[87] Phan-Thien, N. (2013). *Understanding Viscoelasticity: Basics of Rheology*. Advanced Texts in Physics. Springer Berlin Heidelberg.

[88] Rabolt, J. F., Russell, T. P., and Twieg, R. J. (1984). Structural studies of semifluorinated n-alkanes. 1. Synthesis and characterization of F(CF2)n(CH2)mH in the solid state. *Macromolecules*, 17(12):2786–2794.

[89] Renaud, G., Lazzari, R., and Leroy, F. (2009). Probing surface and interface morphology with Grazing Incidence Small Angle X-Ray Scattering. *Surf. Sci. Rep.*, 64(8):255–380.

[90] Riess, J. G. (2003). Fluorocarbon-based injectable gaseous microbubbles for diagnosis and therapy. *Curr. Opin. Colloid Interface Sci.*, 8(3):259–266.

[91] Safran, S. (2018). *Statistical Thermodynamics Of Surfaces, Interfaces, And Membranes*. CRC Press.

[92] Sagis, L. M. and Fischer, P. (2014). Nonlinear rheology of complex fluid-fluid interfaces. *Curr. Opin. Colloid Interface Sci.*, 19(6):520–529.

[93] Sagis, L. M. C. (2011). Dynamic properties of interfaces in soft matter: Experiments and theory. *Rev. Mod. Phys.*, 83(4):1367–1403.

[94] Schmidbauer, M. (2004). Dynamical Scattering Effects at Grazing Incidence Conditions. In *X-Ray Diffus. Scatt. from Self-Organized Mesoscopic Semicond. Struct. Springer Tracts Mod. Physics, vol 199*. Springer, Berlin, Heidelberg.

[95] Schmutz, M., Michels, B., Marie, P., and Krafft, M. P. (2003). Fluorinated Vesicles Made from Combinations of Phospholipids and Semifluorinated Alkanes. Direct Experimental Evidence of the Location of the Semifluorinated Alkane within the Bilayer. *Langmuir*, 19(12):4889–4894.

[96] Schneider, M. F., Andelman, D., and Tanaka, M. (2005). Stripes of partially fluorinated alkyl chains: Dipolar Langmuir monolayers. *J. Chem. Phys.*, 122(9):1–5.

[97] Schneider, M. F., Lim, K., Fuller, G. G., and Tanaka, M. (2002). Rheology of glycocalix model at air/water interface. *Phys. Chem. Chem. Phys.*, 4(10):1949–1952.

[98] Schutt, E. G., Klein, D. H., Mattrey, R. M., and Riess, J. G. (2003). Injectable Microbubbles as Contrast Agents for Diagnostic Ultrasound Imaging: The Key Role of Perfluorochemicals. *Angew. Chemie Int. Ed.*, 42(28):3218–3235.

[99] Schwieger, C., Liu, X., and Krafft, M. P. (2017). Self-assembled mesoscopic surface domains of fluorocarbon-hydrocarbon diblocks can form at zero surface pressure: tilting of solid-like hydrocarbon moieties compensates for cross-section mismatch with fluorocarbon moieties. *Phys. Chem. Chem. Phys.*, 19(35):23809–23816.

[100] Slaughter, W. S. (2012). *The Linearized Theory of Elasticity*. Birkhäuser Boston.

[101] Sollich, P., Lequeux, F., Hébraud, P., and Cates, M. E. (1997). Rheology of Soft Glassy Materials. *Phys. Rev. Lett.*, 78(10):2020–2023.

[102] Steven, P., Scherer, D., Krösser, S., Beckert, M., Cursiefen, C., and Kaercher, T. (2015). Semifluorinated alkane eye drops for treatment of dry eye disease - a prospective, multicenter noninterventional study. *J. Ocul. Pharmacol. Ther.*, 31(8):498–503.

[103] Stubenrauch, C. and Miller, R. (2004). Stability of foam films and surface rheology: an oscillating bubble study at low frequencies. *J. Phys. Chem. B*, 108(20):6412–6421.

[104] Szíjjártó, C., Rossi, S., Waton, G., and Krafft, M. P. (2012). Effects of perfluorocarbon gases on the size and stability characteristics of phospholipid-coated microbubbles: Osmotic effect versus interfacial film stabilization. *Langmuir*, 28(2):1182–1189.

[105] van Kempen, S. E. H. J., Schols, H. A., van der Linden, E., and Sagis, L. M. C. (2013). Non-linear surface dilatational rheology as a tool for understanding

microstructures of air/water interfaces stabilized by oligofructose fatty acid esters. *Soft Matter*, 9(40):9579.

[106] Vrânceanu, M., Winkler, K., Nirschl, H., and Leneweit, G. (2007). Surface rheology of monolayers of phospholipids and cholesterol measured with axisymmetric drop shape analysis. *Colloids Surfaces A Physicochem. Eng. Asp.*, 311(1-3):140–153.

[107] Wang, J., Nguyen, A. V., and Farrokhpay, S. (2016). Effects of surface rheology and surface potential on foam stability. *Colloids Surfaces A Physicochem. Eng. Asp.*, 488:70–81.

[108] Wilhelm, M. (2002). Fourier-transform rheology. *Macromol. Mater. Eng.*, 287(2):83–105.

[109] Witten, T. A. (1990). Structured fluids. *Phys. Today*, 43:21–28.

[110] Zang, D. Y., Rio, E., Langevin, D., Wei, B., and Binks, B. P. (2010). Viscoelastic properties of silica nanoparticle monolayers at the air-water interface. *Eur. Phys. J. E. Soft Matter*, 31(2):125–34.